University of Alberta

Measurement of radiofrequency emissions from a medical linac

by

Benjamin L. Burke

A thesis submitted to the Faculty of Graduate Studies and Research
in partial fulfillment of the requirements for the degree of

Master of Science
in
Medical Physics

Department of Physics

Edmonton, Alberta
Fall 2008

Your file Votre référence
ISBN: 978-0-494-47188-3
Our file Notre référence
ISBN: 978-0-494-47188-3

Abstract

The integration of a medical linear accelerator (linac) with a magnetic resonance imaging (MRI) system requires the measurement and shielding of radiofrequency (RF) noise produced by linac pulsing. Near field RF measurement techniques and their suitability for measurement of RF emissions of a medical linac are investigated in this thesis. A measurement technique using commercial field probes is proposed and investigated by measurement of the radiation pattern of a dipole emission source. The results indicate the field probes appropriately measure the electric and magnetic field components of the dipole source. The measurement technique is then applied to measure the RF emissions of a medical linac. The results of these preliminary measurements show that the RF emissions of a medical linear accelerator contain substantial field strengths in the range of DC – 50 MHz. Finally, future directions for the isolation and shielding of the sources of RF emission are suggested.

Acknowledgement

My supervisor, Dr. Gino Fallone thank you for all of the direction you have provided during the completion of this degree. You provided me with support, both financial and scientific, and also provided motivation and guidance to help me successfully complete my project. Without your supervision and support this thesis would not have become a reality.

Dr. Marco Carlone, I cannot thank you enough for the countless hours you spent with me on this project. You gave up weekends to help with data collection and many, many afternoons helping me to make sense of it all. Your constant support and guidance has helped me to become a better student and researcher. Your unwavering patience through the ups and downs of my research provided me with the determination necessary to complete this project.

To the members of my committee: Dr. Sataypal Rathee, your input has been invaluable to me. Your willingness to dedicate a large amount of your time helping me, particularly towards the end of my project, was immensely appreciated. The numerous discussions we had about the analysis of my data were instrumental in the successful completion of my thesis. I look forward to working with you during my PhD. Dr. Ron Sloboda, thank you so much for agreeing to become a member of my supervisory committee only weeks before the completion of my degree. Your willingness to help me out was very kind and was greatly appreciated. Your comments and suggestions were extremely helpful in

making my thesis clear and concise. Dr. Sharon Morsink, thank you for being the chair of my examination committee.

To my research partner Michael Lamey, I cannot begin to thank you for all the help you have given me over the last few years. You gave up weekends and week nights to help acquire data; you spent countless hours discussing linac and antenna theory. You helped me get back on track if I got frustrated and always provided a laugh when I needed one. I have thoroughly enjoyed working alongside you and have greatly appreciated your friendship over these years. I look forward to continuing our work together in the future.

To my family: my parents Joan and Lester, my sister Erin and my brother Mitch. Without your unwavering support over the last years I don't know if I would have finished. You have always encouraged me and I am eternally grateful for that. I am extremely lucky to have such a caring family.

Finally, to my love Vanessa, your constant love and encouragement have given me the strength and resolve to finish this degree. You have never wavered in your support of me and without that support I would be lost. I thank you with all my heart.

Table of Contents

1 Introduction 1

1.1 Advances in radiotherapy 1

1.2 Intensity-modulated radiotherapy and imaging 1

1.3 Organ movement and treatment errors 3

1.4 Image-guided radiotherapy 4

1.5 MRI and real-time IGRT 5

1.5.1 MRI accelerator 6

1.5.2 Viewray Renaissance™ System 1000 6

1.5.3 MRI-Linac integration at Cross Cancer Institute 7

2 Theory 12

2.1 Antenna Theory and Definitions 15

2.1.1 Dipole Antenna 15

2.1.2 Loop Antenna 20

2.1.3 Antenna Parameters: Terms and Descriptions 21

2.1.4 Field Regions 23

2.1.5 Derivation of field region boundaries 26

2.1.6 Power and the Poynting Vector 31

2.1.7 Input Impedance 32

2.2 Linear Accelerator Theory 34

2.2.1 Pulsed Power modulator (PPM) 34

2.2.2 Magnetron and Klystron RF sources 35

2.2.3 Circulator 38

2.2.4 Automatic Frequency Control (AFC) 39
2.2.5 Water cooling system 39
2.2.6 Vacuum system 40
2.2.7 Pressure system 40
2.2.8 Accelerator structure 40
2.3 Pulsed power modulator: a detailed description [10] 42
3 Materials and Methods 50
3.1 Dipole antenna measurements 50
3.1.1 Introduction 50
3.1.2 Equipment 51
3.1.3 Materials testing for antenna stand 59
3.1.4 Note about transition to linear accelerators 64
3.2 Linear Accelerator Measurements 67
3.2.1 Introduction 67
3.2.2 Equipment 67
3.2.3 Measurement setup 72
4 Results 76
4.1 Dipole Antenna Radiation Pattern Measurements 76
4.1.1 Simplification of theory 76
4.1.2 Radial Measurements 78
4.1.3 Angular measurements 84
4.2 Linear Accelerator Measurements (time domain) 88
4.2.1 Electric field measurements 88

4.2.2 Magnetic field measurements 91
4.3 Linear Accelerator Measurements (Frequency domain) 94
4.3.1 Electric field measurements 96
4.3.2 Magnetic field measurements 99
4.4 Electric and Magnetic field values 103
5 Discussion 107
5.1 Antenna pattern measurements 107
5.2 Linear Accelerator Measurements 107
6 Conclusions and Future Work 111
6.1 Conclusions 111
6.2 Future Work 112
7 Bibliography 114

List of Tables

Table 4-1 Comparison of HVPS current frequencies to Electric Field probe frequencies 97

Table 4-2 Comparison of Magnetron Current frequencies to Electric Field probe frequencies 98

Table 4-3 Frequency comparison of HVPS current and Magnetic Field probe signal 100

Table 4-4 Frequency comparison of magnetron current and Magnetic Field probe signal 101

Table 4-5 Comparison of PFN Voltage frequencies to Magnetic Field probe frequencies 102

List of Figures

Figure 1-1 MR-Linac design: Courtesy Dr. G. Fallone 9

Figure 2-1 Graphical depiction of a dipole antenna (A) and constructed dipole antenna (B) 16

Figure 2-2 Theoretical dipole radiation pattern in 3D (left) and 2D (right), the 2D plane represents the same plane as the purple slice in the 3D pattern. The dipole is oriented along the z axis of the 3D pattern, thus along the horizontal axis of the 2D pattern 18

Figure 2-3 Geometry for near-field analysis of a dipole radiator 19

Figure 2-4 Graphical representation of a loop antenna (A) and constructed loop antenna (B) 20

Figure 2-5 Geometry of radiation pattern measurement 27

Figure 2-6 Block Diagram of a Medical Linear Accelerator 34

Figure 2-7 Block Diagram of Pulsed Power Modulator 35

Figure 2-8 Transverse plane of magnetron oscillator tube 37

Figure 2-9 Functional diagram of a klystron RF amplifier with a single cavity 38

Figure 2-10 Simplified Charging Circuit 43

Figure 2-11 Simplified modulator circuitry highlighting the DeQing circuit 44

Figure 2-12 Modulator circuit with discharge section 46

Figure 2-13 Test signal measurement locations in modulator 47

Figure 3-1 Dipole antenna 12cm in length constructed in-house with half-wavelength resonance frequency of 1.25GHz 51

Figure 3-2 HZ-11 probe set: arrows indicate probes used in 52

Figure 3-3 Ball (a) and Loop (b) probe [© Rohde and Schwarz, 2008 with permission] 53

Figure 3-4 Circuit approximation of electric field probe 54

Figure 3-5 Performance factors for the ball probe and 6cm loop probe (Picture reproduced with permission of Rohde and Schwarz) 56

Figure 3-6 Impedance matching circuit for 4396B analyzer 57

Figure 3-7 Autocad depiction of antenna stand 59

Figure 3-8 Obstruction measurement setup 60

Figure 3-9 Loop antenna receiver 61

Figure 3-10 Obstruction measurements with wood as obstruction 61

Figure 3-11 Obstruction measurements with Delrin as obstruction 62

Figure 3-12 Constructed Antenna stand – showing entire stand (left) 63

Figure 3-13 Comparison of Voltages measured by the spectrum analyzer and the oscilloscope 66

Figure 3-14 Magnetron Current (pink), PFN voltage (red) and HVPS current (cyan) on ms timescale 69

Figure 3-15 Magnetron current (pink), PFN voltage (Red) and HVPS current (cyan) on a μs timescale 70

Figure 3-16 Electric field probe (blue) and magnetic field probe (green) signals on a ms timescale 71

Figure 3-17 Electric field probe (blue) and magnetic field probe (green) signals on a μs timescale 71

Figure 3-18 Measurement setup for MRIL field measurements 74

Figure 4-1 Angular dipole radiation pattern for dipole lengths of half-(blue),..... 77

Figure 4-2 Comparison of near-field electric field to a 1/r type decay..... 78

Figure 4-3 Electric field measurements and theory 81

Figure 4-4 Magnetic field measurements and theory 82

Figure 4-5 Comparison of radial electric field measurements made at 83

Figure 4-6 Comparison of radial magnetic field measurements made at 400 and 500 MHz; with (red, blue) and without (pink, cyan) room effects 84

Figure 4-7 Rotation of dipole transmit antenna (shown at ~ 45°) 85

Figure 4-8 Angular field measurements for Electric and Magnetic fields at 400MHz .. 86

Figure 4-9 Angular field measurements for Electric and Magnetic fields at 500MHz .. 87

Figure 4-10 Angular electric field pattern of dipole antenna measured at 1GHz..... 87

Figure 4-11 Time domain comparison of HVPS current and electric field probe signal . 89

Figure 4-12 Time domain comparison of magnetron current and electric field probe signal 90

Figure 4-13 Time domain comparison of PFN voltage and electric field probe signal.... 91

Figure 4-14 Time domain comparison of HVPS current and magnetic field probe signal 92

Figure 4-15 Time domain comparison of magnetron current and magnetic field probe signal 93

Figure 4-16 Time domain comparison of PFN voltage and magnetic field probe signal. 94

Figure 4-17 Frequency comparison of HVPS current and electric field probe signal..... 97

Figure 4-18 Frequency comparison of magnetron current and electric field probe signal98

Figure 4-19 Frequency comparison of PFN voltage and electric field probe signal 99

Figure 4-20 Frequency comparison of HVPS current and magnetic field probe signal. 100

Figure 4-21 Frequency comparison of magnetron current and magnetic field probe signal 101

Figure 4-22 Frequency comparison of PFN voltage and magnetic field probe signal ... 103

Figure 4-23 Electric field values as a function of frequency 104

Figure 4-24 Magnetic field values as a function of frequency 105

Figure 4-25 Magnetic field values as a function of frequency (scaled y -axis) 105

Figure 5-1 Approximation of power as a function of frequency 109

List of Abbreviations

AFC	Automatic Frequency Control
APS	Advanced Photon Source
CBCT	Cone Beam Computed Tomography
CT	Computed Tomography
EM	Electromagnetic
EMC	Electromagnetic Compatibility
EPID	Electronic Portal Imaging Device
HVPS	High Voltage Power Supply
IGRT	Image-Guided Radiotherapy
IMRT	Intensity Modulated Radiotherapy
kV	Kilovoltage
linac	Linear Accelerator
MLC	Multileaf Collimator
MRI	Magnetic Resonance Imaging
MV	Megavoltage
PF	Performance Factor
PFN	Pulse Forming Network
PPM	Pulsed Power Modulator
RMS	Root Mean Squared
RF	Radiofrequency

1 Introduction

1.1 Advances in radiotherapy

Since the discovery of the X-ray by Röntgen in 1895, there have been great advances in the field of radiotherapy and the treatment of cancer by x-rays. Initially the progress was largely driven by physics and physicists alone [1]; with much of the progress revolving around the understanding of the interaction of radiation with body tissues and increasing both the quality and quantity of radiation that was given to the tumor [1]. The field of radiobiology was then born out of a need to understand the effects of radiation at a cellular level, and to explore the difference in response to radiation of normal tissues compared with tumor tissues [1]. Finally, radiation oncology emerged as a scientific discipline, whose umbrella encompassed physicists, biologists, chemists, radiation oncologists and other scientific and medical personnel [1]. This union of scientific disciplines led to much collaboration and allowed for research to drive clinical trials and, in turn, allowed for the outcome of these clinical trials to provide direction for new research. A comprehensive review of the progression of radiation oncology is given in [1] and is beyond the scope of this work.

1.2 Intensity-modulated radiotherapy and imaging

Advances in radiotherapy have allowed cancer treatment to improve by having higher energy photon and electron beams and the delivery of more conformal doses, which allow for an increase in dose to the tumor while also minimizing the dose to the

surrounding normal tissues [2]. The advent and improvement of three dimensional (3D) treatment planning allowed for the advancement of conformal radiation doses leading to greater tumor control and eradication [2, 3]. Intensity modulated radiation therapy (IMRT) using high energy photon beams delivers highly shaped dose distributions to the patient treating tumors that occur in close proximity of the critical structures. The addition of multileaf collimators (MLCs) to the treatment machines also added to computer controlled delivery IMRT [1], allowing for a more homogeneous irradiation of the cancerous tissue and the sparing of normal tissues. With the increased efficacy of radiation therapy treatments came a necessity for improved patient imaging methods in terms of localizing the diseased volume and critical structures, as well as ensuring the reproducible setup of the patient with respect to the treatment beams during the course of fractionated radiation therapy. The advances in treatment and treatment planning are only useful if the tumor can be accurately imaged and contoured, and the patient accurately set up for the treatment, such that the treatment margins around the tumor, used to account for setup uncertainty, can be reduced and normal tissue surrounding the tumor can be spared [1-3]. Thus, alongside the aforementioned advances there has been significant progress in imaging methods as well [1]. The introduction of computed tomography (CT) imaging of tumors in the 1970s allowed for researchers and clinicians to gain knowledge of the differences in electron densities of tumors when compared to normal tissues, and as such design conformal treatments using multiple treatment beams [1]. The introduction of magnetic resonance imaging (MRI) into the field of oncology also allowed for vast improvement in tumor delineation [1]. The exquisite soft tissue contrast available in MRI makes it ideal for separating the tumor from the surrounding normal tissues, while with

CT the tumor often has electron densities which are quite similar to the surrounding normal, soft tissue structures making delineation more difficult. Thus MRI has become very useful in helping to determine treatment volumes, though CT data is typically still used for treatment planning because of the electron density data it provides for radiation dose calculation [2, 3]. This density information is very useful for dose calculation in the presence of tissue homogeneity.

1.3 Organ movement and treatment errors

The goal of all radiotherapy is to deliver the planned conformal radiation precisely to the tumor volume, while minimizing the dose to other tissues. Traditional radiotherapy and IMRT can suffer from several sources of uncertainty or error [4]. Several different sources of error are listed but the most important are said to be setup error and organ motion, which can both lead to daily errors and variations in treatment. Setup error refers to geometric error in positioning the patient with respect to the treatment beams during the course of radiation therapy. Organ motion refers to the movement of tumor or critical structures of the patient during a treatment session due to respiration and other physiological functions. Much work has been done to quantify and understand organ motion [4-7]. Many different schemes have been attempted to deal with organ motion such as respiratory gating, mathematical modeling of breathing and motion, fiducial markers for tracking and many more [7]. The majority of the schemes proposed in [6] and [7] either rely on pre/post treatment session imaging to estimate what movement occurred during the treatment or modeling the movement mathematically to calculate errors. Ideally a system would be able to image the tumor during the treatment fraction and account for tumor movement by adjusting the treatment scheme. This field of study is

called image-guided radiotherapy (IGRT) and is the field that is driving the research contained in this work.

1.4 Image-guided radiotherapy

There are several different IGRT modalities that have been introduced or proposed, and are reviewed in [2] and [3]; however, for this work, only some of these will be discussed. One of the first, and currently most widespread [2], IGRT technologies is the electronic portal imaging device (EPID). EPIDs use the treatment megavoltage (MV) photon beam and an image receptor to form MV radiographic images of the patient in treatment position. These images are generally used for positioning the patient to assure beam accuracy, but they can also be used to monitor the dose received by the patient [2, 8]. EPIDs are a planar imaging modality which uses the MV treatment beam, and thus images suffer with reduced contrast due both to small differences in the attenuation of the beam by various tissue types and overlaying of 3D structures onto 2D planes [2]. Recently, the 2D MV radiographs provided by the EPIDs at various angles around the patient have been used to obtain MV cone beam CT images. The contrast problem with MV photons has been circumvented by the addition of an on-board X-ray imaging device, which is generally mounted perpendicular to the treatment beam [2, 3]. This peripheral imaging device acquires kilovoltage (kV) cone-beam CT (CBCT) data, which has better contrast than the MV images and provides volumetric data to generate 3D images [2,3].

Another approach to IGRT is helical Tomotherapy, which has taken the concept of helical CT imaging and combined it with a 6 MV linear accelerator (linac) [2, 3]. The kV

X-ray tube in the CT scanner has been replaced with a 3.5 MV photon beam (imaging beam) from the treatment linac operating at 6 MV (treatment beam) [2]. The patient is given IMRT as the couch is translated through the bore of the scanner. MVCT images can also be acquired before treatment, but images can not be acquired during treatment due to the use of the same linac for imaging and treatment. This unit can alleviate errors associated with moving the patient since they remain on the same couch for the imaging and subsequent treatment. This is in contrast to the treatment systems that do not have a method of 3-D imaging of the patient in treatment position and where the patient set up is largely based on 2-D EPID images.

In-room CT scanners have also been introduced as IGRT devices, where the patient is imaged with the CT sharing the same couch as the treatment unit, then the couch is translated to the treatment unit and treatment begins. This type of unit has the advantage of acquiring diagnostic (kV) CT images, which according to [9] provide superior images when compared with the Tomotherapy and on-board kV and MV imaging technologies described above. Again with this unit it is not possible to image during treatment.

1.5 MRI and real-time IGRT

The next logical step in the evolution of IGRT would be to provide a system capable of providing 3D images in real-time during the patient treatment, rather than pre/post fraction. One logical way to do this is to introduce MRI into the IGRT process, because of its better-quality soft tissue contrast when compared to X-ray methods. The MRI scanner will also be a separate entity from the treatment unit and so will allow for simultaneous treatment and imaging. Indeed, MRI does not require mechanical motion of

the imaging subsystems as in the case of CT for imaging the patient. This notion of integrating MRI with radiotherapy is the driving force behind this thesis work. There are a few other centers working along this vein and their research will be briefly described below.

1.5.1 MRI accelerator

Researchers at the University of Utrecht are designing a prototype called an MRI accelerator which involves the integration of a closed-bore 1.5 Tesla MRI scanner with a 6 MV linac, mounted on a ring gantry [10]. The linac will rotate around the stationary MRI scanner and its beam will pass through the scanner before reaching the patient. This approach must overcome significant obstacles such as: (1) the transmission of the treatment beam through the magnet and gradient coil structure; (2) radiofrequency (RF) interference from linac to the MRI system; (3) effect of the magnetic field on the accelerating waveguide and (4) relatively strong magnetic field effects on the patient dosimetry with 1.5 Tesla magnet [2].

1.5.2 Viewray Renaissance™ System 1000

Another research group at the University of Florida has proposed a unit which combines a split solenoid 0.3 Tesla MRI scanner with a three-headed Cobalt 60 IMRT unit [2, 3, 11 and 12]. The three Cobalt sources are placed on a rotational gantry to allow for 3-beam treatment from all angles, and the presence of a MLC will allow for the application of IMRT [12]. The low field strength avoids deleterious dose effects, but the system could have difficulty due to the ferromagnetic nature of Cobalt: it is possible that the magnetic field homogeneity could be perturbed by the presence of the Cobalt sources.

1.5.3 MRI-Linac integration at Cross Cancer Institute

The work presented in this thesis is focused on aiding in the successful integration of an MRI scanner with a linac, a project under development here at the Cross Cancer Institute (CCI). In the proposed design of the MRI-linac at the CCI, a bi-planar magnet and the linear accelerator have been mechanically couple such that the vertically mounted waveguide, and the beam generation and collimation system are physically displaced from the magnet. The open space between the poles of the magnet allows unobstructed irradiation of the magnet at any gantry angle. The entire integrated assembly is able to rotate around the patient. A prototype 0.2 Tesla permanent, bi-planar magnet with a 27 cm gap between the poles is currently attached to a refurbished 6 MV linac and the preliminary measurements are underway. There are possible difficulties that could be encountered with this integration, such as: 1) magnetic interference between the MRI magnetic fields and the linac rotation; (2) mechanical interference between the two devices, (3) effect of the magnetic field on the accelerating waveguide; (4) effect of the magnetic field on patient dosimetry; (5) RF interference with MR imaging caused by the pulsing of the linac. The first two obstacles have largely been overcome simply through efficient design; the MRI scanner will rotate along with the linac, thus making them stationary with respect to each other. The 3rd obstacle is currently being investigated by others in our research group. Radiation dose distribution in the patient for MV photon beams in the presence of main uniform magnetic field have been studied [15] and it has been shown that 0.2 T magnet has a smaller impact on the dose distributions compared to 1.5 T magnet. Our group is developing techniques to account for this small dose perturbation during the treatment planning step [16]. The topic of RF interference is the

focus of this research. A preliminary design is shown in figure 1-1, and the rotational nature can be seen with the rings. Also, the open bore low field magnet avoids the treatment beam passing through any structures before irradiating the patient and avoids deleterious dosimetry effects that can be seen at higher fields.

The purpose of this thesis is to develop and test a measurement technique which will allow the measurement of the electric and magnetic field components of the RF emissions of a medical linac due to the pulsed nature of the radiation production. The theory and terminology necessary for understanding these RF measurements are contained in chapter 2, along with a description of linac functional block diagram and a detailed description of the linac pulsing mechanism. Very little work has been done measuring RF emissions of medical linacs and the only related research that was found by the author were emission measurements taken on the Advanced Photon Source (APS) kicker magnet power supplies [13]. These power supplies deliver currents which exceed 2400 amps peak [12], which far exceed the typical 90-110 amps [14] that a medical linac utilizes, through the magnetron/klystron, though the measurement techniques bear some similarity to the techniques used in this thesis.

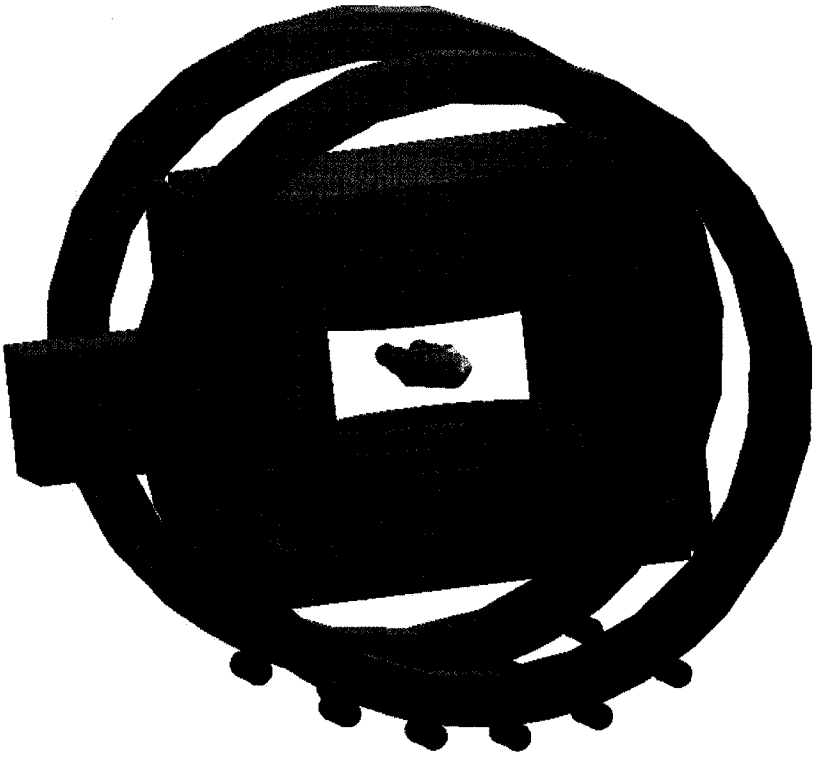

Figure 1-1 MR-Linac design: Courtesy Dr. G. Fallone

References:

1. Bernier, J., Hall, E.J., Giaccia, A. Radiation oncology: a century of achievements. *Nature Reviews Cancer* **4**, 737-747 (2004).
2. Verellen, D., De Ridder, M., Linthout, N., et al. Innovations in image-guided radiotherapy. *Nature Reviews Cancer* **7**, 949-960 (2007).
3. Dawson, L.A., Jaffray, D.A. Advances in Image-Guided Radiation Therapy. *Journal of Clinical Oncology* **25(8)** 938-946 (2007)
4. Marcel van Herk. Errors and Margins in Radiotherapy. *Seminars in Radiation Oncology* **14(1)** 52-54 (2004)
5. Rietzel, E., Rosenthal, S.J., Gierga, D.P., et al. Moving targets: detection and tracking of internal organ motion for treatment planning and patient set-up. *Radiother. Oncol.* **73** S68-S72 (2004)
6. Langen, K.M., Jones, T.L. Organ motion and its management *Int. J. Radiation Oncology Biol. Phys.* **50(1)** 265-278 (2001)
7. S Webb. Motion effects in (intensity modulate) radiation therapy: a review. *Physics in Medicine and Biology* **51** R403-R42 (2006).
8. Jake Van Dyke. *The Modern Technology of Radiation Oncology: A Compendium for Medical Physicists and Radiation Oncologists*. Medical Physics Publishing, Madison, Wisconsin, 1999.
9. Stützel, J., Oelfke, O., Nill, S. A quantitative image quality comparison of four different image guided radiotherapy devices. *Radiotherapy and Oncology* **86** 20-24 (2008)

10. Lagendijk, J.J.W., Raaymakers, B.W., Raaijmakers, A.J.E., et al. MRI/linac integration. *Radiotherapy and Oncology* **86** 25-29 (2008)

11. J.F. Dempsey. An Image-Guided Device Providing 4D CINE MRI Simultaneous to Radiotherapy Delivery. *Journal of Radiotherapy in Practice* **5** 179 (2006)

12. www.viewray.com

13. Carwardine, J.A., Wang, J. Analysis of the Electrical Noise from the APS Kicker Magnet Power Supplies. Proceedings of the 1995 IEEE *Particle Accelerator Conference.* **2** 1242-1244 (1995)

14. Karzmark, C.J., Nunan, C.S., Tanabe, E., *Medical Electron Accelerators*, McGraw-Hill Inc., New York, 1993

15. Kirkby, C., Stanescu, T., et al. Patient dosimetry for hybrid MRI-radiotherapy systems. *Medical Physics* **35** 1019 (2008)

16. Stanescu, T., Kirkby, C., et al. Sci-Fri PM: Planning-02: MRI-based radiation treatment planning for an MRI-linac system. *Medical Physics* **35** 3412 (2008)

2 Theory

The major topic of this thesis involves the electromagnetic (EM) radiation of antennas, and of linear accelerators. As such, before the specific task of presenting antenna theory is undertaken, a brief introduction to the governing principles of EM radiation will be presented.

It is well known in EM theory that stationary electric charges will produce electric fields that remain constant with time, while steady currents will analogously produce magnetic fields which are constant with time [1]. The two areas of EM theory that discuss these phenomena are called electrostatics and magnetostatics, respectively. Coulomb's law states that the electric field produced by stationary charges is [1]:

$$E(r) = \frac{1}{4\pi\varepsilon_0} \int_V \frac{\rho(r')}{(r-r')^2} \overrightarrow{d\tau'} \tag{2-1}$$

Where ρ is the charge density, *r'* is the location of the charge density, *r* is the location of the measurement point, and ε_0 is the permittivity of free space. Analogously, the Biot-Savart law states that the magnetic field created by a steady line current is [1]:

$$B(r) = \frac{\mu_0 I}{4\pi} \int_{line} \frac{\overrightarrow{dl'} \times \vec{r'}}{r'^2} \tag{2-2}$$

Where *I* is the current, μ_0 is permeability of free space, *dl'* represents a line segment along the current, *r'* is the distance between *dl'* and the measurement point. The arrows above *dl'* and *r'* represent vector quantities.

The above relations hold true for time independent charge and current configurations; now the case of time dependent charge and current will be examined. In the above equations it is assumed that electric and magnetic phenomena are essentially independent [1, 2]. This assumption of independence fell apart in 1831 when Faraday performed his induction experiments [1]. The discovery that a changing magnetic field induces an electric field caused a shift in thinking about electric and magnetic fields; they were then thought of as *electromagnetic* fields. Driven by Faraday's work, in 1865, J.C. Maxwell corrected the equations derived from the static situation and introduced a set of equations describing electromagnetic behavior, which would later be termed *Maxwell's equations* [1, 2]. These equations are as follows [1, 2]:

Gauss's law $$\vec{\nabla} \cdot \vec{E} = \frac{\rho}{\varepsilon_0} \tag{2-3}$$

Absence of free magnetic monopoles $$\vec{\nabla} \cdot \vec{B} = 0 \tag{2-4}$$

Faraday's law $$\vec{\nabla} \times \vec{E} = -\frac{\partial \vec{B}}{\partial t} \tag{2-5}$$

Ampère's law $$\vec{\nabla} \times \vec{B} = \mu_0 \vec{J} + \mu_0 \varepsilon_0 \frac{\partial \vec{E}}{\partial t} \tag{2-6}$$

These equations form the basis of all the different phenomena seen in classical electrodynamics. When combined with the Lorentz force equation,

$$\vec{F} = q(\vec{E} + \vec{v} \times \vec{B}) \tag{2-7}$$

Where q is the charge, and $\vec{v}$ is the velocity of the charge, they can be used to describe all classical electrodynamics [1, 2]. As will be seen later, Faraday's law plays an essential role in magnetic loop probes (see section 3.1.2).

Now that the behavior of electromagnetic fields has been briefly touched upon, it is necessary to this work to also briefly describe the energy contained and radiated by EM fields. Derivation of the time rate of change of energy in a specified volume can be seen in detail in refs [1] and [2], and only the result will be shown here from [1].

$$\frac{dW}{dt} = -\frac{d}{dt}\int_V \frac{1}{2}\left(\varepsilon_0 E^2 + \frac{B^2}{\mu_0}\right)d\tau - \frac{1}{\mu_0}\oint_S \left(\vec{E}\times\vec{B}\right)\cdot da \tag{2-9}$$

Where V is the volume of integration and S is the surface of V. This is the work-energy theorem, also known as *Poynting's Theorem*. The first integral on the right indicates the energy which is stored in the electric and magnetic fields. The second integral represents the power being radiated out of the volume V. This radiated power density is called the Poynting vector and is represented as [1]:

$$\vec{S} \equiv \frac{1}{\mu_0}\left(\vec{E}\times\vec{B}\right) \tag{2-10}$$

This represents the power per unit area that is being radiated, and the integral seen above represents the power being radiated through a given surface by a given source.

Finally, it should be noted that not all charge and current arrangements will allow for the radiation of EM energy. For radiation to occur the charges (or currents) must be accelerating, and thus have a time dependence [1, 3]. The detailed physics description of the radiation process is beyond the scope of this thesis but an important point to note is that radiation of a specific frequency can be obtained by using a continuously oscillating current at the frequency of interest. This fundamental principle is vital to antenna theory and measurements.

2.1 Antenna Theory and Definitions

A radio frequency antenna is any device, usually metal, that can be used to either radiate or receive electromagnetic waves in the radio frequency (RF) range [3]. An ideal transmit antenna will accept maximum power from a RF source and radiate all of the accepted power into space; however, practically, an antenna is not completely efficient and it will dissipate some power resistively in the form of heat [4]. There are several different types of antennas that are used for various applications; a few of these, relevant to the work in this thesis, will be briefly described in the following sections.

2.1.1 Dipole Antenna

A very basic type of antenna is the dipole antenna, which consists of two wires attached to a two-conductor coaxial transmission line. One wire is attached to the center conductor of the transmission line and the other is attached to the outer conductor (Figure 2-1a and b). When used as a transmitter a time-varying voltage can be applied to the transmission line creating a time-varying electric field between the center and outer conductors in the transmission line, which in turn creates time-varying magnetic fields. These varying electric and magnetic fields form electromagnetic waves which propagate along the transmission line [3]. If we assume a sinusoidal voltage source, then the EM waves will also exhibit a sinusoidal variation along the transmission line. This will create sinusoidal current distributions in the two dipole wires and, since they are connected to opposite conductors, the current directions will always be opposed. The result is a spatial current distribution which looks like a sine wave across the dipole [3], with the actual shape depending on the length of the dipole compared to the wavelength (λ) of interest.

This oscillating current distribution causes the emission of EM waves which can then propagate into space; the frequency of these emitted waves will be the same as the frequency of the current oscillation. One of the most common forms of the dipole antenna is the λ/2 dipole because its current distribution is very simple: minimum at the ends and maximum at the midpoint of the dipole. This gives the λ/2 dipole a simple radiation pattern. λ/2 refers to the total length of the dipole being half the resonant wavelength.

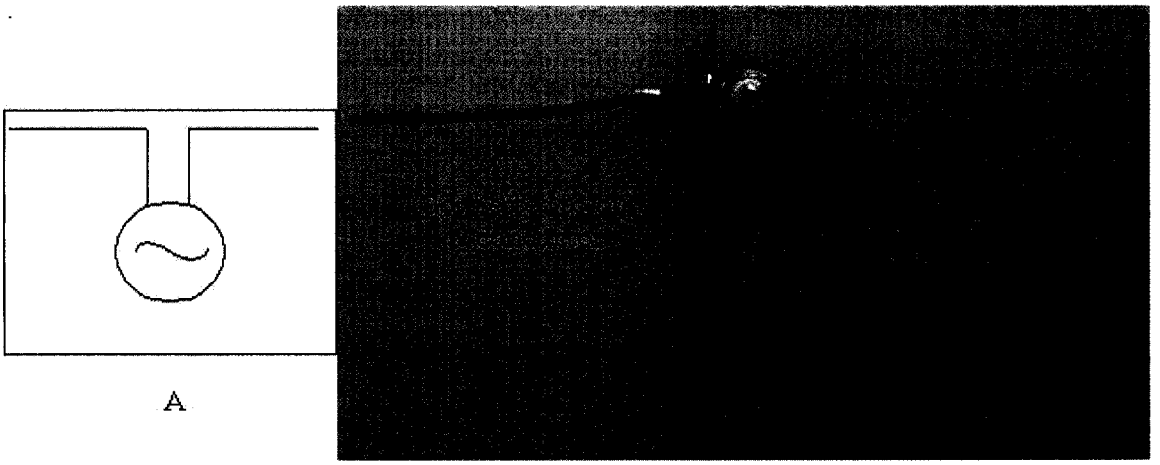

Figure 2-1 Graphical depiction of a dipole antenna (A) and constructed dipole antenna (B)

A dipole antenna was chosen to be the standard radiation source for this work because of its well known radiation pattern. In particular, the radiation pattern of a half wavelength (λ/2) dipole is very simple, and symmetrical. The theoretical pattern for a half-wavelength dipole is shown in Figure 2-2, which is a graphical representation of the time-averaged power density [3]:

$$W_{av} = \eta \frac{|I_0|^2}{8\pi^2 r^2} \left[\frac{\cos\left(\frac{\pi}{2}\cos\theta\right)}{\sin\theta} \right]^2 \cong \eta \frac{|I_0|^2}{8\pi^2 r^2} \sin^3(\theta) \qquad (2\text{-}11)$$

Where η is the free space wave impedance (377ohms), I_0 is the peak current [3] in the dipole, r is the distance from the dipole antenna center to the point of measurement and θ is the angle that this measurement point makes with the z axis (see Figure 2-3).

The time-averaged power density follows from the Poynting vector of the time-averaged electric and magnetic fields of a dipole antenna [3]. The time averaged Poynting vector is,

$$W_{av} = \frac{1}{2}\mathrm{Re}\left[\vec{E} \times \vec{H}\right] \tag{2-12}$$

$$E = E_\theta = j\eta \frac{I_0 e^{-jkr}}{2\pi r}\left[\frac{\cos\left(\frac{\pi}{2}\cos\theta\right)}{\sin\theta}\right] \tag{2-13a}$$

$$H = H_\phi = j\frac{I_0 e^{-jkr}}{2\pi r}\left[\frac{\cos\left(\frac{\pi}{2}\cos\theta\right)}{\sin\theta}\right] \tag{2-13b}$$

Where j represents $\sqrt{-1}$. Equations 2-12, 2-13a, and 2-13b are all functions of both r and θ. The factor of ½ appears because the electric and magnetic fields are peak values, and this term would be omitted if RMS values were used [3]. Also, H is used here instead of B as it represents the field intensity in A/m, given by $\vec{B} = \mu_0 \vec{H}$, but (2-12) is equivalent to (2-10). It can also be noted that the electric and magnetic field patterns have identical forms, except for a scaling factor of η.

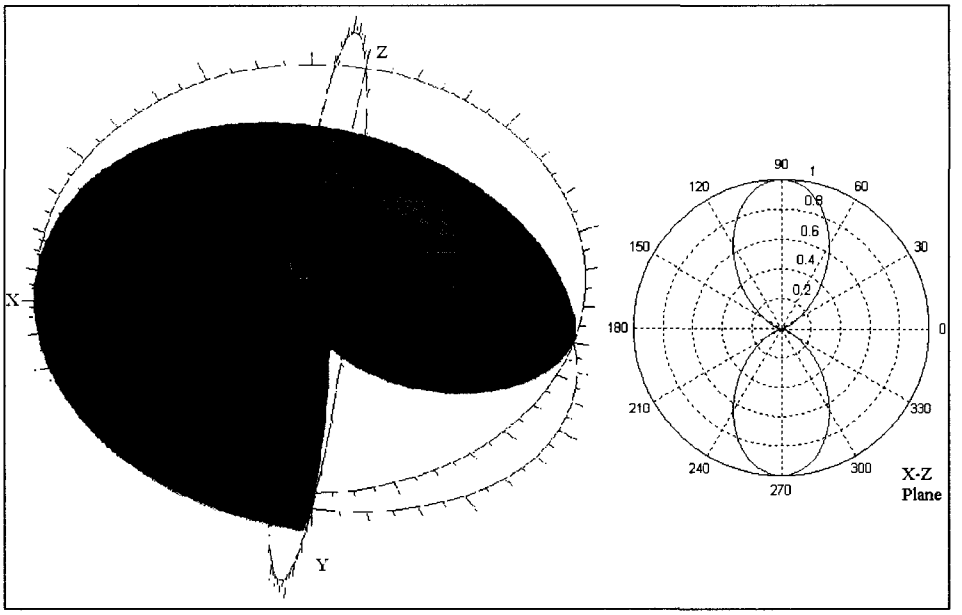

Figure 2-2 Theoretical dipole radiation pattern in 3D (left) and 2D (right), the 2D plane represents the same plane as the purple slice in the 3D pattern. The dipole is oriented along the z axis of the 3D pattern, thus along the horizontal axis of the 2D pattern

Because both the near field and far field (see section 2.1.4 for limits) of the dipole will be examined with subsequent measurements, the near fields of a dipole antenna will now be stated. In the near field the electric field of a dipole consists of two components, while the magnetic field consists of one component [3]:

$$E = E_\rho + E_z \tag{2-14}$$

$$E_\rho = j\frac{\eta I_0}{4\pi y}\left[\left(z-\frac{l}{2}\right)\frac{e^{-jkR_1}}{R_1}+\left(z+\frac{l}{2}\right)\frac{e^{-kR_2}}{R_2}-2z\cos\left(\frac{kl}{2}\right)\frac{e^{-jkr}}{r}\right] \tag{2-14a}$$

$$E_z = -j\frac{\eta I_0}{4\pi}\left[\frac{e^{-jkR_1}}{R_1}+\frac{e^{-jkR_2}}{R_2}-2\cos\left(\frac{kl}{2}\right)\frac{e^{-jkr}}{r}\right] \tag{2-14b}$$

$$H_\phi = \frac{I_0}{4\pi j}\frac{1}{y}\left[e^{-jkR_1}+e^{-jkR_2}+2\cos\left(\frac{kl}{2}\right)e^{-jkr}\right] \tag{2-14c}$$

Where the values x, y, and z represent the distance from the dipole center to the point of measurement, represented by the vector r. R_1 and R_2 represent the distance from the dipole extremities to the point of measurement. r is the total distance to the point of measurement represented by $r = \sqrt{x^2 + y^2 + z^2}$. Finally, ρ refers to the x-y plane and E_ρ represents the radial component of the electric field. (Figure 2-3)

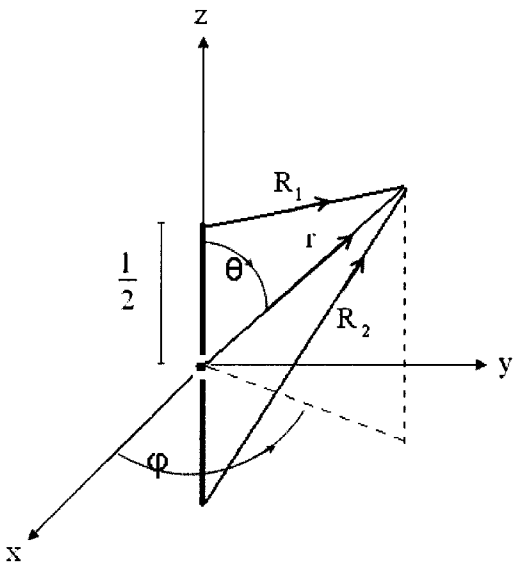

Figure 2-3 Geometry for near-field analysis of a dipole radiator

Although these near field equations are much more complex than the far field patterns given above (eqns. 2-13a, b), by an appropriate choice of measurement geometry they can be significantly simplified. This will be shown later in this text (Section 4.1.1).

2.1.2 Loop Antenna

A loop antenna will be used as a receiver in chapter 3, and as such is described here. A loop antenna is a simple antenna consisting of single wire connected at one end to the centre conductor of a transmission line and connected at the other end to the outer conductor of the transmission line (Figure 2-4). Loop antennas are generally divided into two broad categories: electrically small ($N*C < \lambda/10$; N = number of turns, C = circumference of loop) and electrically large ($C \sim \lambda$) [3]. Electrically small loop antennas have very small radiation resistances and as such are very poor radiators; they are thus commonly used as field probes in the receiving mode, where the signal to noise ratio is more important than the antenna efficiency. Loop antennas are often used as magnetic field probes because when an EM wave is incident upon the loop an open circuit voltage is induced in the loop, which is related to the component of magnetic flux density, B, perpendicular to the plane of the loop [3].

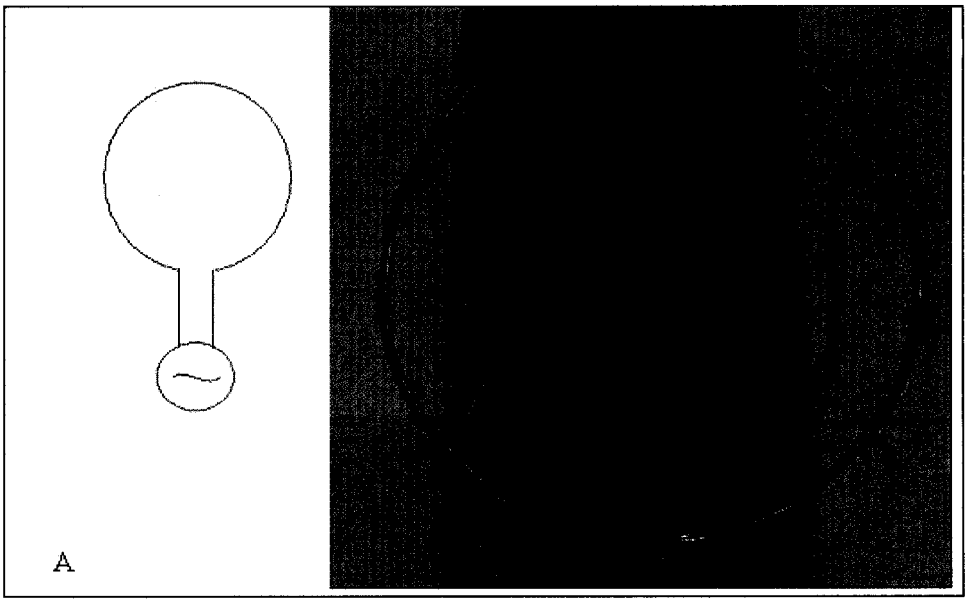

Figure 2-4 Graphical representation of a loop antenna (A) and constructed loop antenna (B)

2.1.3 Antenna Parameters: Terms and Descriptions

There are several parameters needed to properly describe the functioning and performance of an antenna. Many of these parameters have been referred to by different terms over the years and this can cause some ambiguity. To avoid confusion the relevant terms will be stated and described below; definitions are taken from [3] and [5].

Radiation Pattern: The radiation pattern of an antenna, also called the antenna pattern, is described in [5] as "The spatial distribution of a quantity which characterizes the electromagnetic field generated by an antenna." This pattern can be expressed in a number of different ways and is generally proportional to one of the following: power flux density, directivity, radiation intensity, field strength, phase and polarization. However, the most common radiation pattern is the radiation power density pattern or power pattern. This is a graphical representation of the power density radiated by the antenna at a constant radius as a function of angle. The radiation pattern demonstrates where the radiation maxima and minima are located for a particular antenna, and by reciprocity displays the orientations of maximum and minimum acceptance of electromagnetic energy.

Radiation Power Density: This quantity reflects the power that is carried by an electromagnetic wave as a function of area; it is described by the Poynting vector [5]

$$\vec{S} = \vec{E} \times \vec{H}$$

$$Where,\ \vec{S} = Poynting\ Vector\left(\frac{W}{m^2}\right)$$

$$\vec{E} = Electric\ Field\ Strength\left(\frac{V}{m}\right)$$

$$\vec{H} = Magnetic\ Field\ Strength\left(\frac{A}{m}\right)$$

Radiation Intensity: As defined by [5], radiation intensity is "In a given direction, the power radiated from an antenna per unit solid angle." If integrated over all angles it will give the total power.

Directivity: The directivity of an antenna is defined as "the ratio of the radiation intensity in a given direction from the antenna to the radiation intensity averaged over all directions" [5]. If a direction is not explicitly given, then the directivity is assumed to be given along the direction of maximum radiation. In other words, the directivity is the ratio of radiation intensity of an antenna along a specified direction to the radiation intensity of an isotropic radiation source, where the total radiated power of each antenna is equal.

Radiation Efficiency: The radiation efficiency of an antenna is "the ratio of the total power radiated by an antenna to the net power accepted by the antenna from the connected transmitter."[5] It is merely a measure of how much of the power being accepted by the antenna is being radiated; it does not take into account power being reflected back to the source due to impedance mismatch (See section 2.1.7). The radiation

efficiency is difficult to measure [4] and is not often explicitly used because it is contained implicitly in the gain of an antenna.

Gain: Antenna gain is defined as "the ratio of the radiation intensity, in a given direction, to the radiation intensity that would be obtained if the power accepted by the antenna were radiated isotropically."[5] Another way of stating this is that the antenna gain is the product of the directivity and the radiation efficiency. Again here, as with the radiation efficiency, the gain does not account for mismatch losses. [5]

2.1.4 Field Regions

The volume surrounding a radiating antenna is typically divided into three separate regions: (a) the reactive near field, (b) the radiating near field and (c) the far field. The different regions exhibit different electromagnetic field properties. It is important to note that the boundaries suggested below are not rigid and do not represent physical boundaries where drastic changes in field properties occur, but there are fundamental differences between the three regions [3, 6].

The *reactive near-field* is "That portion of the near-field region immediately surrounding the antenna, wherein the reactive field dominates" [5]. It is called 'reactive' because for a non-resonant antenna, reactive power is circulated between the reactive near field and the source, and for a resonant antenna, reactive power is circulated within the reactive near field [6]. In both of these cases the circulated power is associated with the quasi-

static, non-propagating field components. For antennas that are large in comparison to the wavelength in question, the boundary of this field region is typically given as

$$R < 0.62\sqrt{\frac{D^3}{\lambda}}$$

Where R is the radial distance from the antenna, D is the largest dimension of the antenna and λ is the wavelength [3]. However, if the antenna is not large compared to the wavelength, as in the case of an electrically small dipole, the boundary of this region is usually given as [3, 5, and 6]

$$R \approx \frac{\lambda}{2\pi}$$

The *radiating near-field* is "that portion of the near field region of an antenna between the far field and the reactive portion of the near field region, wherein the angular field distribution is dependent upon the distance from the antenna" [5]. In this region the radiating components of the EM fields dominate. In the case of an antenna whose dimensions are large compared to the wavelength the inner boundary for this region is

$$R \geq 0.62\sqrt{\frac{D^3}{\lambda}}$$

and the outer boundary is

$$R < \frac{2D^2}{\lambda}$$

For electrically small antennas this region may not exist and the radiation pattern will shift directly from the reactive near-field to the far-field. [3, 6] The criterion for the radiating near-field to exist relies upon interference from different points on the antenna

being significantly large [6], thus causing the angular field distribution to be dependent on the distance from the antenna. This field region is also termed the 'Fresnel' region in reference to the analogous optical Fresnel diffraction zone; indicating the angular pattern dependence on distance.

The *far-field* region is "that region of the field of an antenna where the angular distribution is essentially independent of the distance of a specified point in the antenna region" [5]. In this region it is only the radiating part of the field that is significant. In the far field the electric and magnetic field components are orthogonal and are related by the impedance of free space,

$$\eta_0 = \frac{E}{H} = 377\Omega$$

For antennas whose largest dimension, D, is large compared to the wavelength the far field region is taken to begin at

$$R > \frac{2D^2}{\lambda}$$

For antennas whose largest dimension does not satisfy the above condition, such as a dipole whose length is smaller than λ but still a significant fraction of λ, this field boundary is insufficient and the boundary must be extended to meet the following condition:

$$R >> \lambda$$

In the far field region the angular distribution of the radiation is independent of the distance from the antenna. If the antenna is focused at infinity the far-field region is sometimes referred to as the Fraunhofer region, analogous to the optical equivalent. This

analogy means that the radiation waves are plane waves in this region. In this region the power density decreases with the inverse square of the distance [6]. The simple relationship between the electric and magnetic field components, mentioned above, in this region makes it simpler to use far-field approximations for some near field applications; however, these approximations are not always valid and for accurate results they should not be used [6].

2.1.5 Derivation of field region boundaries

In section 2.1.4 the field regions of a radiating antenna are described. The boundaries of the field regions are given as $R \leq 0.62\sqrt{\frac{D^3}{\lambda}}$ for the boundary between the *reactive near-field* and *radiating near-field*, and as $R \leq \frac{2D^2}{\lambda}$ for the boundary between the *radiating near field* and the *far-field.* These limits will be derived below based on the geometry of the measurement of the field pattern. Figure 2-5 shows the geometry of a measurement point, P, along the radiation pattern of a simple line source antenna [7]. The length of the antenna is $2z'$. Consider the antenna as a simple filament of current along the z axis.

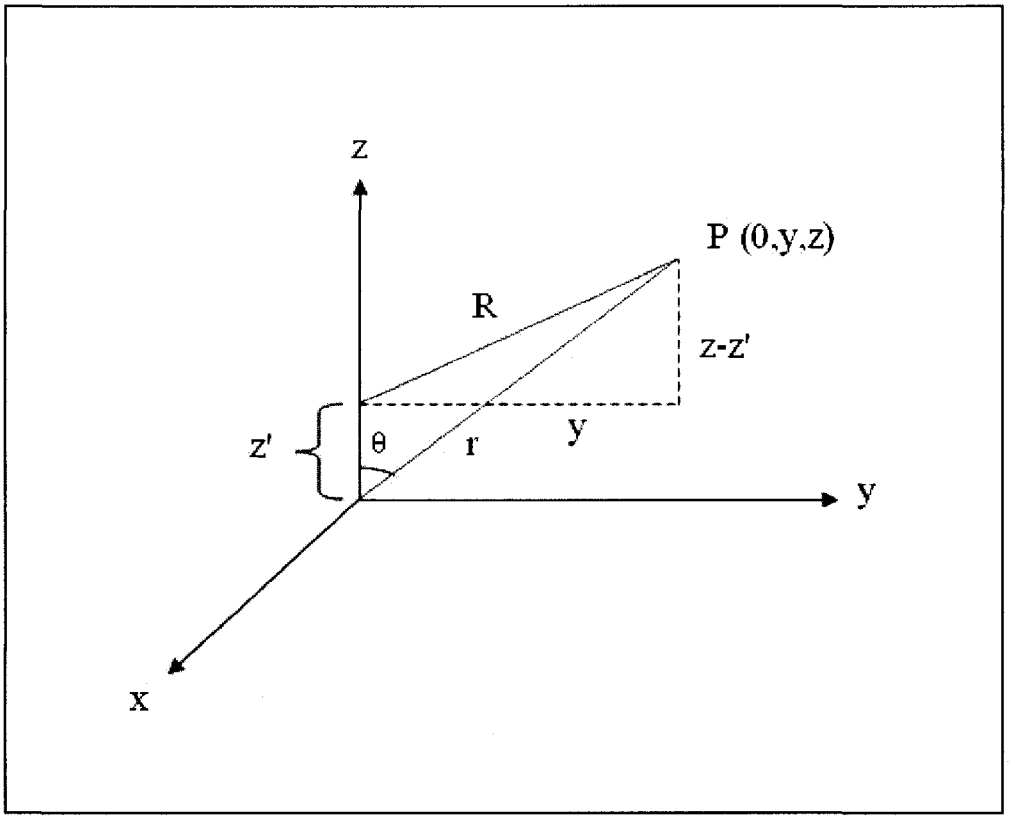

Figure 2-5 - Geometry of radiation pattern measurement

In Figure 2-5 *P* is the measurement point; *r* is the distance from the center of the line source to the measurement point; *R* is the distance from the end of the line source to the measurement point; θ is the angle between the z axis and the measurement point and, though it isn't shown, φ would represent rotation around the z axis (i.e. constant *r* and *z*).

Because of the symmetrical arrangement of the source, the radiation fields should not vary with φ [7]. As the measurement point is rotated around at constant *r* and *z*, the source will appear the same at all points on this circle; this allows the use of the geometry in Figure 2-5 to derive the field pattern limits.

First it is necessary to define the vector potential, A, for the line source; since our line source is along z there is only a z component to A. Hence, the vector potential becomes:

$$A = A_z = \int I(z') \frac{e^{-j\beta R}}{4\pi R} dz' \tag{2-15}$$

Where $I(z')$ is the current distribution of the line source, j is $\sqrt{-1}$ and β is the phase constant of a plane wave [3], $\beta = \omega\sqrt{\mu\varepsilon}$, where ω is the frequency in radians, μ is the permeability of the medium and ε is the permittivity of the medium.

Using the geometry seen in Figure 2-5 it is possible to develop an expression for R.

$$r^2 = y^2 + z^2 \tag{2-16}$$

$$z = r\cos\theta \tag{2-17}$$

$$R = \sqrt{y^2 + (z - z')^2} = \sqrt{y^2 + z^2 - 2zz' + (z')^2} \tag{2-18}$$

Substituting (2-16) and (2-17) into (2-18) yields:

$$R = \left\{r^2 + [-2rz'\cos\theta] + (z')^2\right\}^{\frac{1}{2}} \tag{2-19}$$

Now that an expression for R has been stated, a special case of the Taylor series, called the Maclaurin series, will be applied to (2-19) to develop approximate expression for R. The Taylor series is defined as follows [8]:

$$f(x) = \sum_{n=0}^{\infty} \frac{f^n(a)}{n!}(x - a)^n \tag{2-20}$$

And the special case of a = 0 is the Maclaurin series, defined as [8]:

$$f(x) = \sum_{n=0}^{\infty} \frac{f^n(0)}{n!} x^n \tag{2-21}$$

When (2-21) is applied to (2-19), first the differentials are calculated:

$$R = f(z') = \sqrt{r^2 - 2rz'\cos\theta + z'^2} \; : \qquad f(0) = r \tag{2-22}$$

$$f'(z') = \frac{-2r\cos\theta + 2z'}{2\sqrt{r^2 - 2rz'\cos\theta + z'^2}} \; : \qquad f'(0) = -\cos\theta \tag{2-23}$$

$$f''(z') = \frac{(\sin\theta)^2 r^2}{\left(r^2 - 2rz'\cos\theta + z'^2\right)^{\frac{3}{2}}} \; : \qquad f''(0) = \frac{(\sin\theta)^2}{r} \tag{2-24}$$

$$f'''(z') = \frac{3(\sin\theta)^2 r^2 (r\cos\theta - z')}{\left(r^2 - 2rz'\cos\theta + z'^2\right)^{\frac{5}{2}}} \qquad f'''(0) = \frac{3(\sin\theta)^2\cos\theta}{r^2} \tag{2-25}$$

These differentials are then placed into (2-21):

$$R = r - z'\cos\theta + \frac{z'^2(\sin\theta)^2}{2r} + \frac{z'^3(\sin\theta)^2\cos\theta}{2r^2} \tag{2-26}$$

This expression for R is then substituted into the phase term of equation (2-15) and the vector potential can be evaluated. In the denominator of (2-15) the approximation $R \approx r$ is commonly used as the contributions from the other terms in (2-26) are negligible [7]. In the phase term, $-\beta R$, small contributions from the terms in (2-26) can introduce substantial errors if the terms are ignored, so they must be included. However, as the measurement point is moved farther away from the source, the contributions from the trailing terms of (2-26) become less. The integral in (2-15) is a summation of the contribution to the vector potential of all the points along the line source. The amplitude of the wave contributed by different points will be practically equal, but there may be a significant difference in phase if the path length difference between the two contributing waves is a considerable portion of a wavelength [7]. The field region boundaries are

derived by assuring a path length difference of $\frac{\lambda}{16}$ or less; this represents a phase difference of $\frac{\pi}{8}$ [3, 7]. This phase difference is chosen because it is deemed an acceptable error in phase.

Thus the field zone boundary between the reactive near field and the radiating near field is derived by equating the maximum value of the fourth term of (2-26) with $\frac{\lambda}{16}$. Terms after the fourth do not contribute significantly to the total so are excluded. The maximum value occurs when $z' = D/2$ [7], where D is the length of the line source, and $\theta = 54.7°$.

$$\frac{z'^3 (\sin\theta)^2 \cos\theta}{2r^2} = \frac{\lambda}{16}$$

$$\frac{\left(\frac{D}{2}\right)^3 (\sin 54.7)^2 \cos 54.7}{2r^2} = \frac{\lambda}{16}$$

$$r = 0.62\sqrt{\frac{D^3}{\lambda}}$$

The field zone boundary between the near field and far field is derived by equating the maximum value of the third term of (2-26) with $\frac{\lambda}{16}$. Again, the maximum value for z' is D/2 but this time the maximum value for θ is 90°.

$$\frac{z'^2 (\sin\theta)^2}{2r} = \frac{\lambda}{16}$$

$$\frac{D^2}{8r} = \frac{\lambda}{16}$$

$$r = \frac{2D^2}{\lambda}$$

2.1.6 Power and the Poynting Vector

The power of any electromagnetic field is usually described in terms of the instantaneous Poynting Vector, which was described above (equation 2-10)

$$\vec{W} = \vec{E} \times \vec{H}$$

W is typically used in antenna theory instead of S (as above), so to keep with antenna theory W will now be used. The Poynting vector represents a power density at a specific point in time and as such if a signal is time dependent the Poynting vector at a specific point in space can change. In most electromagnetic compatibility (EMC) measurements the time-averaged Poynting vector is used to describe the power,

$$W_{av} = \frac{1}{2}\mathrm{Re}\left[\vec{E} \times \vec{H}^{*}\right]$$

Where 'Re' refers to the real part of the cross product. The ½ arises from the fact that the E and H fields in the equations are peak values, however, if root mean squared (RMS) values are used instead then the ½ should be omitted [3]. In the far field the equation simplifies to

$$W = \frac{1}{2\eta_0}|E|^2$$

Here η_0 is the impedance of free space mentioned above. However, in the near field both components must be measured independently and combined to obtain the power density for a specific point.

2.1.7 Input Impedance

The capability of an antenna to accept, and subsequently radiate, power from a source is largely determined by the *input impedance* of the antenna [4]. The input impedance is defined as "the impedance presented by an antenna at its terminals" [5] and is also described as "the ratio of the voltage to current at a pair of terminals or the ratio of the appropriate components of the electric to magnetic fields at a point" [3]. In general, the impedance, of any device, is a complex quantity, because devices will typically have a resistance and a reactance, and is usually expressed in the following form:

$$Z = R + jX$$

Where Z is the impedance, R is the resistance and X is the reactance. An antenna usually has complex impedance and proper matching of the antenna to the transmission line is not simple. The impedance of an antenna will be dependent on frequency and so the match between the antenna and the transmission line will only be appropriate for a certain bandwidth [3]. Ideal matching occurs when a 'conjugate match' is made between two devices, meaning the impedance of one device is the complex conjugate of the other [3, 4]. Conjugate matching allows for maximum power transfer to occur between two devices; in the case of an antenna it would be between the antenna and the RF power source. Most RF sources and generators have a purely real impedance, typically 50 ohms [4], this is a convenient value as several types of typical coaxial cable have an impedance of 50 ohms; this means the antenna impedance must also be 50 ohms for conjugate matching. Though a dipole antenna can nominally have an impedance of 73 ohms, using a 50 ohm feed line is still acceptable. The impedance mismatch is reflected in a slight loss of accepted power.

It should be noted that of the power that can be produced by a generator, half of this power is dissipated by the generator's internal resistance and the other half is available to be delivered to the antenna [3]. The amount of power delivered to the antenna that is radiated is dependent on the antenna radiation efficiency. With a radiation efficiency of 1 all of this power will be radiated, else some power will be dissipated resistively as heat. This can be related to the antenna's behavior in receiving mode, where half the power will be transferred to the load, assuming conjugate matching, and the other half will be scattered (reradiated) or dissipated resistively. Thus, the maximum power accepted by the antenna that can be delivered to the receiving system (load) is half, and that is only with conjugate matching and a lossless transmission line [3].

2.2 Linear Accelerator Functional Description

A medical linac consists of several major parts which are shown in a block diagram in Figure 2-6. A brief description of these components and their functionality will follow.

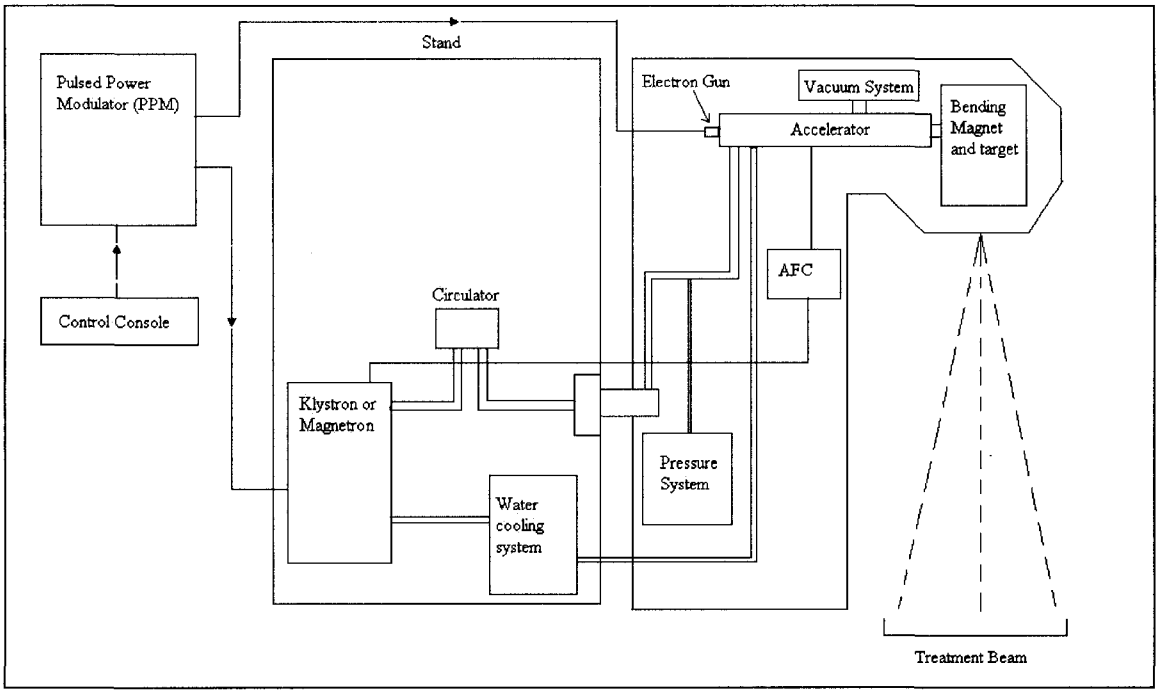

Figure 2-6 Block Diagram of a Medical Linear Accelerator

2.2.1 Pulsed Power modulator (PPM)

All Medical linacs employ a PPM, which consists of a high voltage power source and a pulse modulator. The main task of the PPM is to provide a shaped voltage (or current) pulse to the RF power source of the linac, either a magnetron or a klystron. This is accomplished through several sub-circuits which will be described briefly here and in more detail in section 2.3. The PPM can be represented in a block diagram as shown in

Figure 2-7 [9]. It consists of a power supply, a charging circuit, an isolation circuit, a pulse forming network (PFN) circuit, a switch, and a pulse transformer. The high voltage power supply circuit provides electrical energy to the charging circuit which proceeds to charge the PFN. The isolation circuit assures that no power flows from the PFN back to the power supply and charging circuits. The PFN serves a twofold purpose, first to store the energy needed for the discharge pulse and second, to shape the discharge pulse. Once the PFN is fully charged the switch will be closed to allow the stored energy to discharge in the form of a shaped pulse sent to the transformer, which will step up the voltage and provide a shaped pulse to the magnetron or klystron [9].

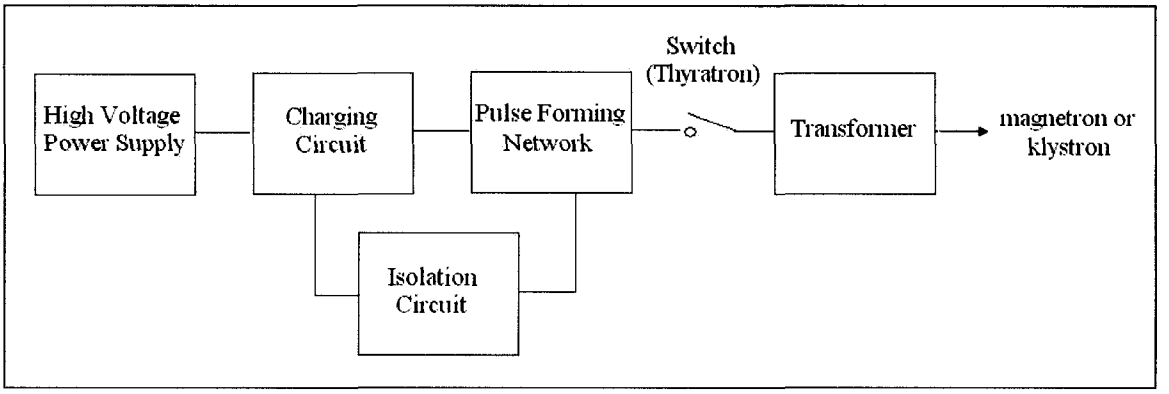

Figure 2-7 Block Diagram of Pulsed Power Modulator

2.2.2 Magnetron and Klystron RF sources

There are two main sources of RF power used in medical accelerators: magnetrons, for low to medium energy linacs and klystrons, for high energy linacs [10].

A magnetron is a type of oscillator used to provide the microwave power necessary for electron acceleration in many low energy linacs. The magnetron typically is a cylindrically shaped device, which consists of a two-element tube containing a cathode and an anode. A cross-sectional slice of the magnetron shows the symmetry of the tube (Figure 2-8). The cathode and the anode can be seen in this Figure with the resonant cavities in the anode. For simplicity, Figure 2-8 only displays 6 cavities, though more typically a magnetron would have 12 [10]. The cylindrical cathode is located in the center, enclosed first by the drift space and then by the anode. There is an applied, static magnetic field which is perpendicular to the plane shown in Figure 2-8 and also a pulsed electric field, E_{DC}, which is applied in the drift space and is directed towards the cathode from the anode [9, 10]. The cathode is continually heated which causes it to emit electrons which are then accelerated towards the anode. Once the electrons begin moving they are subjected to the magnetic field present, and thus to the Lorentz force [9] $F = e(\vec{v} \times \vec{B})$ where e is the electron charge, $\vec{v}$ is the electron velocity and $\vec{B}$ is the magnetic field. This will cause the electrons to begin moving along a curved path. These accelerated electrons then induce small charge distributions on the anode and induce an oscillating electric field, E_{RF}, between subsequent anode cavities (Figure 2-8). This electric field oscillates with microwave frequency and the most common mode of operation is the π mode where there is a phase difference of π radians between subsequent anode cavities [9]. There is a strong interaction between the electrons at the entrance to the cavity and the RF electric field inside the cavity. Energy is transferred from the electrons to the electric field, thus providing the desired microwave power [10]. The electrons, now with considerably less energy, spiral back in towards the cathode [9].

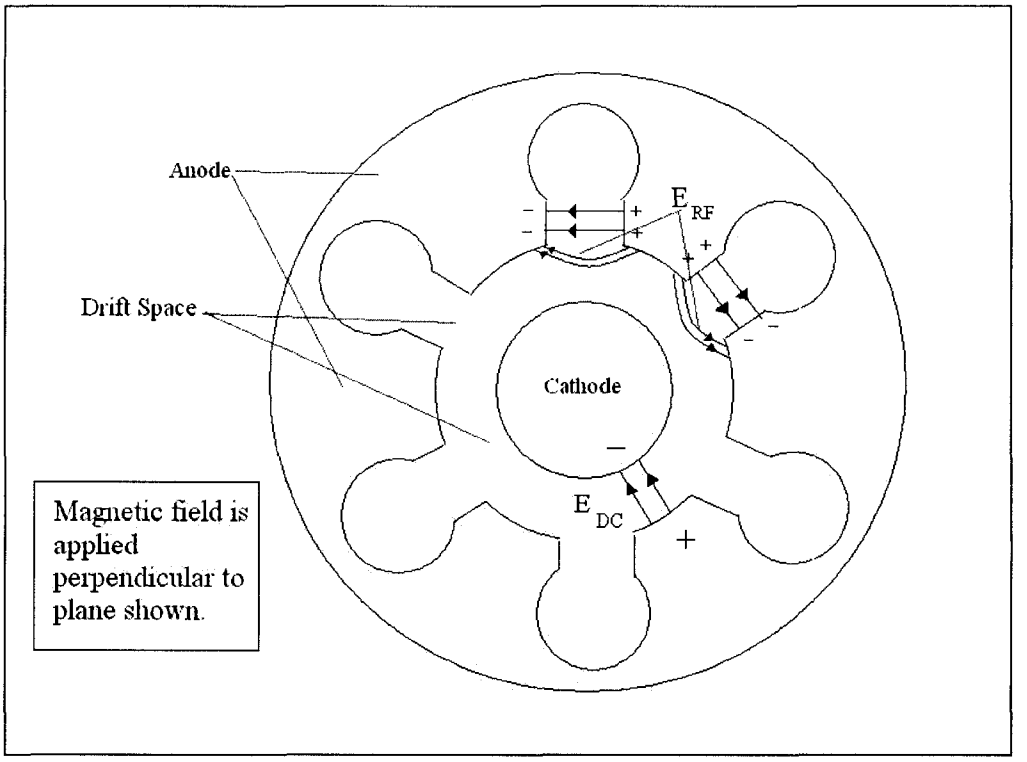

Figure 2-8 Transverse plane of magnetron oscillator tube

A klystron is an RF amplifier, as opposed to the magnetron which is an oscillator. A generic functional diagram of a klystron can be seen in Figure 2-9. A hot wire filament heats up the cathode causing it to eject electrons into the klystron structure; this is also known as the electron gun. These electrons then travel into the 'buncher' cavity, where they are met by a low level RF field. The electric field component of this RF oscillates sinusoidally with time and serves to 'bunch' the electrons together. The early arriving electrons will meet with a positive electric field which acts as a retarding potential, while late arriving electrons will meet a negative electric field and will thus be accelerated [9]. This velocity modulation will cause electrons emitted within the period of the RF to gather into discrete bunches as they travel along the drift tube. Figure 2-9 only shows 1 buncher cavity for simplicity, but klystrons will often have more in order to increase the effectiveness of bunching and to increase the subsequent power amplification [9, 10].

The electron bunches now enter the 'catcher' cavity, which has a resonance at the frequency of the electron bunches, where they induce charges on the cavity ends, thereby setting up a retarding E field which transfers a large amount of the electron's kinetic energy to electromagnetic energy. This electromagnetic energy is then output to provide the microwave power needed for the accelerator. The electrons, now having much lower energy, are collected at the end of the klystron and dissipated as heat [9].

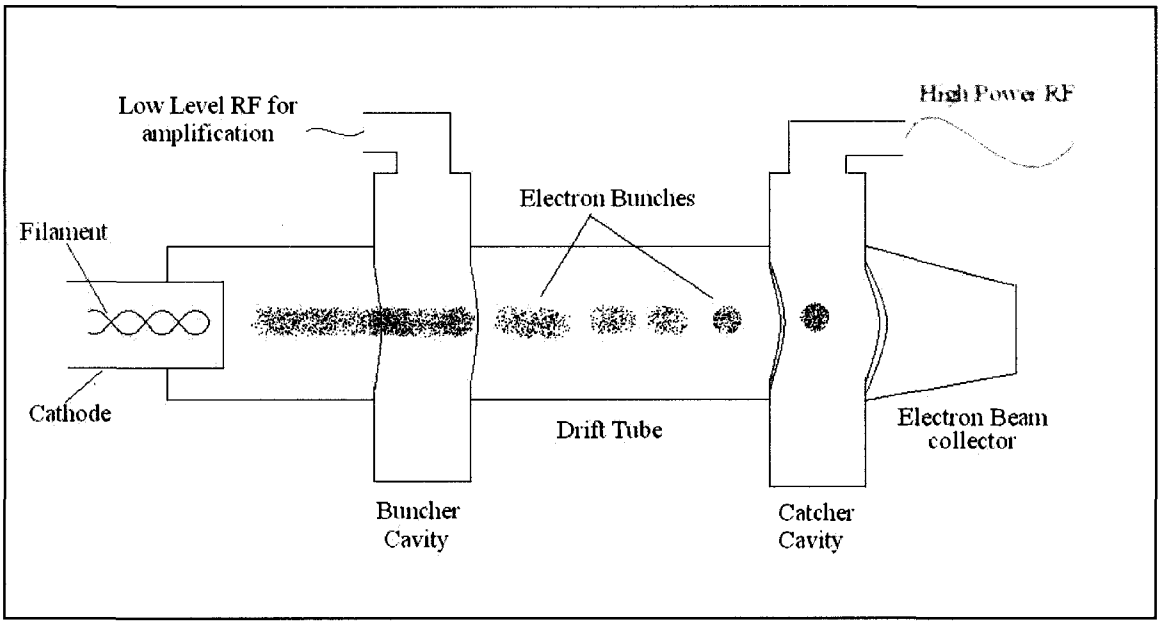

Figure 2-9 Functional diagram of a klystron RF amplifier with a single bunching cavity

2.2.3 Circulator

The circulator is placed between the RF producing mechanism, magnetron or klystron, and the actual accelerating structure. The purpose of the circulator is to isolate the aforementioned sections from each other so that no power gets reflected back to the RF source from the accelerating structure [10]. It can also measure the forward and reflected

power being sent along the waveguide and sends this information to the automatic frequency control (AFC).

2.2.4 Automatic Frequency Control (AFC)

The AFC is a circuit which is designed to monitor the resonant frequency of the accelerator and to then tune the frequency of the RF power source (klystron/magnetron) to the resonant frequency. The amount of forward and reflected power is measured by the circulator and is compared at the resonant frequency [9]. It is important to note here that the amount of reflected power is very small. A delay line is used for the forward power to ensure that the two signals have the same transmission path length. The sum of the two signals should be zero because they should be of equal magnitude but of opposite phase. If the sum of the two signals is not zero, a signal is sent to the RF power source to tune it to the proper frequency. A magnetron is tuned using a motor-driven mechanical tuner. A klystron is tuned by altering the output frequency of the low level RF source.

2.2.5 Water cooling system

The cooling system uses water to cool various components of the linac (RF power source, electromagnet, accelerator structures), trying to keep these components at a constant temperature [9]. The operating temperature is kept above room temperature so as to prevent condensation [10].

2.2.6 Vacuum system

The vacuum system keeps the accelerator at a very high vacuum state, with an approximate pressure of 10^{-7} mmHg [9]. This system is used to prevent the electrical breakdown of the accelerator for the very high EM fields that are present. The vacuum system also keeps the klystron evacuated.

2.2.7 Pressure system

The waveguides are kept pressurized with an inert gas, in most cases sulfur hexafluoride [9, 10]. This pressurized gas increases the power transmission capability of the waveguides and also prevents electrical breakdown and arcing inside the structure. This gas is found in the waveguide between the RF power supply and the accelerator structure and is separated from these components via ceramic windows [9, 10].

2.2.8 Accelerator structure

The accelerator structure consists of an electron gun, which injects electrons into the accelerating waveguide, and the actual accelerating cavities. Once injected into the accelerating cavities the electrons are met with the high energy RF fields provided by the RF power source. The waveguide cavities have a similar function to the bunching cavities discussed earlier; they form clusters of electrons which are continuously accelerated as they travel along the waveguide. Once accelerated to the desired energy, the electrons are focused using a bending magnet and impinge upon a high Z target, Z referring to the atomic number of the target material, to create the x-ray output used for treatment. The

bending magnet provides a magnetic field which changes the trajectory of the electron beam, focusing it into a tight beam. Here, in contrast to the RF power source, energy is transferred from the electric fields to the electrons to accelerate them. There are two general types of accelerator structures that are used, traveling wave and standing wave accelerators; these will be described below [10].

Traveling wave accelerators are typically cylindrical structures with disks inserted to divide the structure into several resonant cavities. These cavities are finely tuned to resonate at a precise frequency [10]. The electrons are injected into the accelerator structure in the buncher section, which has several cavities of decreasing aperture size. The RF power from the power source is also injected at this end of the structure. As the name suggests, the buncher section uses the RF electric fields to group the electrons into discrete bunches. Once through this section, the bunched electrons enter a uniform section which is used to further accelerate them. In a traveling wave accelerator, RF power is injected at one end, used to accelerate the electrons down the length of the structure, and the residual power is then absorbed at the end of the accelerator [9, 10]. The electric field along the accelerator axis varies sinusoidally and as such travels smoothly from the site of power injection to the end. Electrons are accelerated by the negative portion of the electric field wave [10] and gain energy in each subsequent cavity.

Standing wave accelerators function in a manner very similar to traveling wave accelerators, except that the electric field does not travel along the length of the structure.

It changes with time only in magnitude; the pattern remains stationary, analogous to standing waves on a string [10]. The microwave power can be injected into the structure at almost any point along the structure because it will be reflected back and forth from the proximal (electron gun) and distal (target) ends of the accelerator [10]. These forward and reflected waves create standing wave patterns through constructive and destructive interference patterns. Maxima equal to twice the wave amplitude will occur when the two waves add constructively, while zeroes will occur when they add destructively. Every other cavity will have an electric field of zero at all times, making it a node, because it will either have zero electric field or the forward and backward electric fields will be equal and opposite [10]. These cavities were eventually placed on the side (side coupled) to allow for a more compact design in which half the resonant cavities, instead of only a quarter, are accelerating simultaneously [10]. Again here, the electrons are accelerated by the negative portion of the electric field; however they are accelerated by the oscillating standing wave pattern and not carried along by a traveling wave.

2.3 Pulsed power modulator: a detailed description [10]

The measurements in chapter 4 involve comparing EM field measurements to modulator test point signals. To understand these test signals a detailed description of the modulator is provided. The description will gradually build the complex circuitry of the modulator.

First, the charging circuitry of the modulator will be considered. Figure 2-10 shows an extremely simple circuit representing the functionality of the charging portion of the modulator.

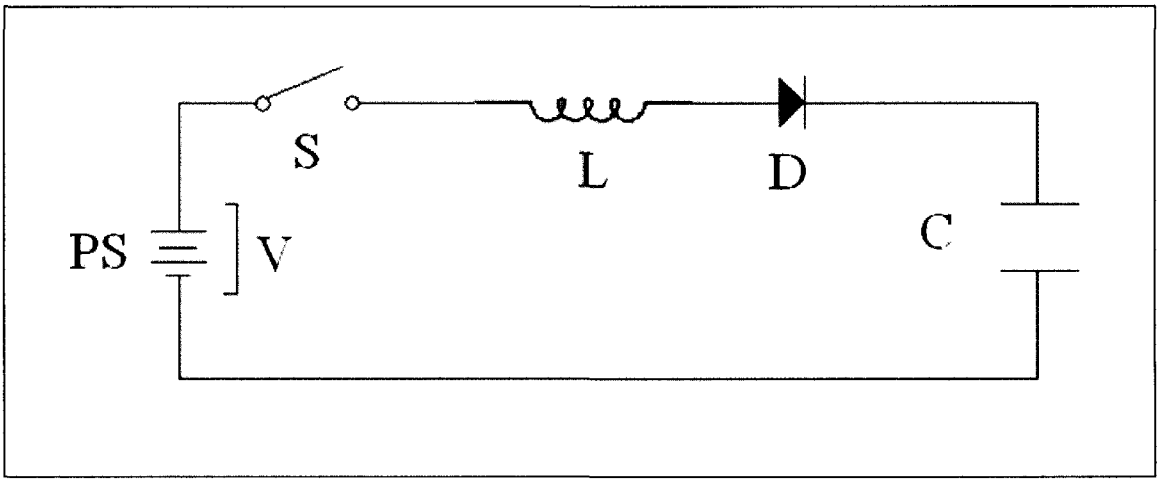

Figure 2-10 Simplified Charging Circuit

Assuming that the capacitor is initially discharged, the switch S is closed to begin the charging process. The voltage of the power supply, V, is developed across the inductor, L. The diode is forward biased, current will begin to flow from the power supply, PS, through L and charge the capacitor C. Also called the choke inductor, L serves to control the current flow to C. As the current begins to flow through L, there is an increase in the magnetic field in the core of L, which results in the storage of energy in the inductor, while C is still being charged. As the charge on C approaches V the current through the inductor becomes a maximum and will then begin to decrease due to the balance of voltage between PS and C. This decrease in current causes the magnetic field present in the core of L to collapse, thus pushing the stored energy towards the capacitor, resulting in the capacitor charging to a value of up to twice the power supply voltage, or 2V. The value of 2V arises because during charging V is developed across L, and then C is charged to V; once the magnetic field collapses the voltage across L gets pushed towards C, resulting in a total voltage of 2V. Without the presence of the diode, D, current would

then begin to flow in the opposite direction because there is a potential difference between the capacitor and the power supply. However, D prevents this reverse current flow and so allows C to retain its charge of 2V. The principles of charging just described offer some excellent advantages: the power supply only needs to be approximately half the desired charge value, the efficiency of charging is very high, and with the use of appropriate DeQing techniques, which will be discussed shortly, the voltage stored in C can be controlled.

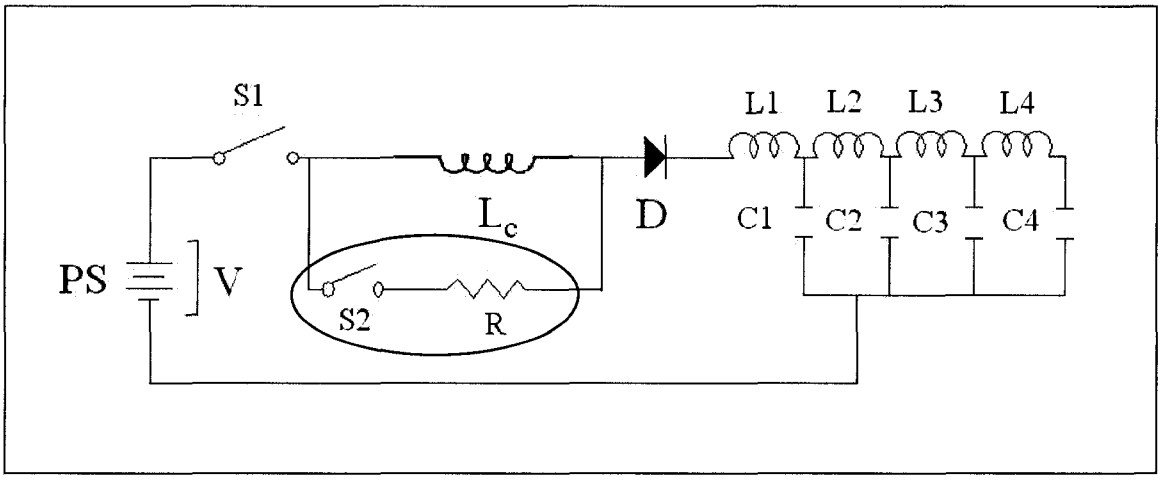

Figure 2-11 Simplified modulator circuitry highlighting the DeQing circuit (circled section)

Figure 2-11 shows a similar circuit to Figure 2-10, except now a DeQing circuit has been introduced, and the capacitor C has been replaced with an appropriate pulse forming network (PFN) representation. Again, if switch S1 is closed the power supply will begin to charge the PFN, which is the grouping of capacitors and inductors seen to the right of D in Figure 2-11, through the choke inductor L_c. The charge will be stored in the capacitors C1...C4. In theory, there will be a slight lag in charge times between successive capacitors due to the inductors between them (L1...L4); however, since the inductance of L_c is large compared to these PFN inductors (approximately 1 Henry for L_c

and micro Henrys for L1...L4) this time difference is negligible when compared to the total charging time. As mentioned before, if the process is unhindered the capacitors will charge to a value of approximately 2V. However, in practice the desired value of the voltage stored in these capacitors is between V and 2V. To achieve this desired value a "DeQing" circuit is required. This circuit, composed of switch S2 and resistor R in Figure 2-11, is placed in parallel with the choke inductor. Once the desired charge voltage is reached in the PFN, S2 will be closed and the remaining stored energy in L_c will be rerouted and dissipated as heat through R. The term DeQing arises from the fact that this parallel resistance is spoiling the quality factor, Q, of the inductor which is given by

$$Q = \frac{\omega L}{R_c} \tag{2-26}$$

Where Q is the quality factor, L is the inductance, R_c is the resistance of the circuit, and ω is the resonant frequency. So when S2 is open, the resistance will be very small and Q will thus be large. When S2 is closed, resistance, R, is deliberately introduced into the circuit causing R_c to become large and thus spoiling or 'DeQing' the inductor circuit.

Now that the PFN is charged, the discharging mechanism will be analyzed. For the following progression it will be assumed that the charge on each capacitor in the PFN is 2V. Figure 2-12 shows the addition of a discharge section to the modulator circuit. T is a thyratron type switch which is triggered once the PFN has reached the desired charge. The thyratron is a gaseous switch and once triggered will begin to conduct current from the PFN into the load (usually a step-up transformer and a magnetron or klystron). The load will be impedance matched to the PFN circuit so that maximum power transfer is achieved. When switch T is closed C1 will begin to discharge through L1. The current

will flow through L1 until the voltage across the load resistor reaches V, at which time C1 will cease its discharge, with a remaining charge of V, and C2 will begin discharging. Once again C2 will cease its discharge when it reaches a voltage of V. This continues until we get to the final capacitor, C4 in Figure 2-12; C4 will discharge all the way to zero, then C3 will discharge to zero, then C2 and finally C1. This continual sequence of discharge will supply a rectangular voltage pulse to the load. The length and magnitude of this pulse are determined by the characteristics of the PFN circuitry. This pulse is used to energize the cathode in the magnetron or klystron.

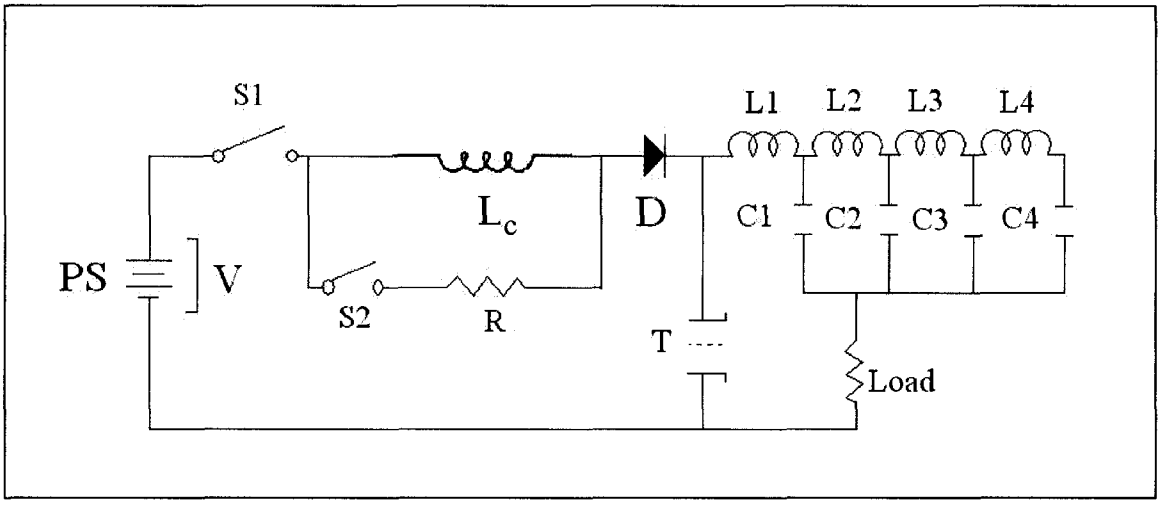

Figure 2-12 Modulator circuit with discharge section

The main functionality of the modulator has now been described and Figure 2-13 shows a few extra components to indicate where the test signals used in chapter 4 are measured. The high voltage power supply (HVPS) current is measured after the choke inductor and diode, the PFN voltage is measured using a voltage divider (VD) and the magnetron current is measured on the load side of the step-up transformer. The shaped voltage pulse

generated by the PFN is used to energize the cathode, in the magnetron or klystron to initiate the amplification of the RF signal; this will be described in chapter 3.

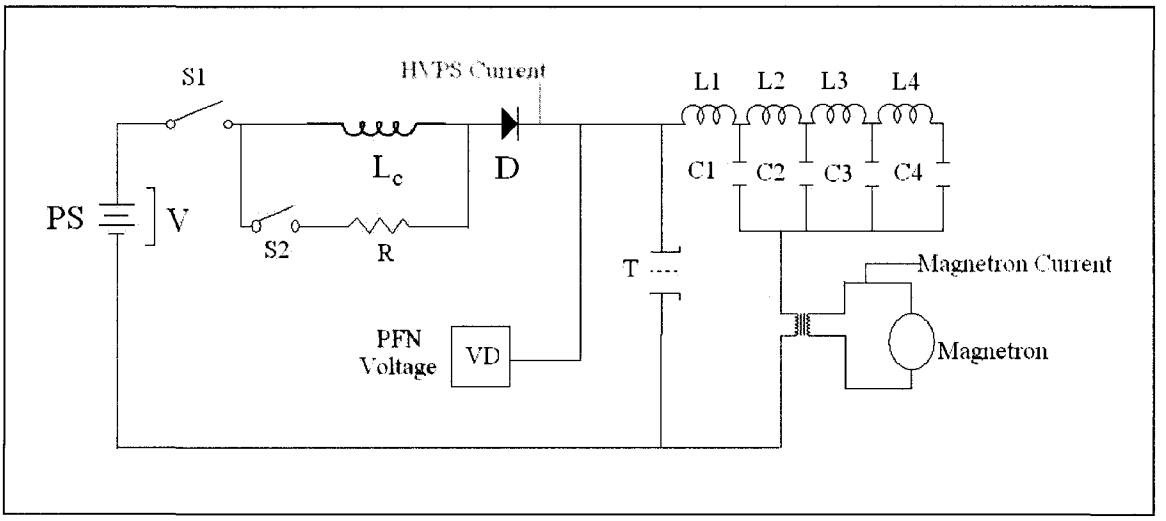

Figure 2-13 Test signal measurement locations in modulator

References:

1. Griffiths, D. J., *Introduction to Electrodynamics 3rd Edition*, Prentice Hall, New Jersey, 1999.
2. Jackson, J. D., *Classical Electrodynamics 3rd Edition*, Wiley & Sons, New York, 1999.
3. Balanis, C. A., *Antenna Theory: Analysis and Design 2nd Edition,* Wiley & Sons, New York, 1997.
4. Maclean, J., Sutton, R., Hoffman, R., "Interpreting Antenna Performance Parameters for EMC Applications Part 1: Radiation Efficiency and Input Impedance Match", *TDK RF Solutions.*
5. *IEEE Transactions on Antennas and Propagation*, Vols. AP-1, No. 3, May 1969; Vol. AP-22, No. 1, January 1974; and Vol. AP-31, No. 6, Part II, November 1983.
6. Maclean, J., Sutton, R., Hoffman, R., "Interpreting Antenna Performance Parameters for EMC Applications Part 2: Radiation Pattern, Gain, and Directivity", *TDK RF Solutions*
7. Stutzman, W.L., Thiele, G.A., *Antenna Theory and Design*, Wiley & Sons, New York, 1981.
8. Stewart, J., *Calculus 4th Edition*, Brookes/Cole Publishing Company, Pacific Grove, 1999.
9. Karzmark, C.J., Nunan, C.S., Tanabe, E., *Medical Electron Accelerators*, McGraw-Hill Inc., New York, 1993

10. Oncology 560 class notes. University of Alberta Medical Physics (2005).

3 Materials and Methods

3.1 Dipole antenna measurements

3.1.1 Introduction

Before RF measurements can be taken on a linear accelerator, a proper near-field measurement technique must first be verified. The frequencies of interest on a linear accelerator (1 ~ 100 MHz) have wavelengths ranging from 3 meters to 300 meters, which necessitates the use of near field techniques as the linac measurements will be made in close proximity to the source (modulator). Quantification of EM emissions in the near field of a radiation source requires the independent measurement of the electric (E) and magnetic (H) field strengths, as there is no longer a simple relationship between the E and H field magnitudes [1].

$$\frac{E}{H} \neq \eta;\ \eta = 377\Omega$$

To ensure correct measurement of these two quantities, the measurement technique will be validated using a known radiation source. An appropriately energized dipole antenna was chosen as the radiation source because its radiation pattern is well known in both the near and far field zones [1]. The following chapters will investigate the measurement of the radiation pattern of a dipole emitter, and the subsequent verification of a near-field measurement technique and its further application to linear accelerator EM emission measurements.

3.1.2 Equipment

The following is a description of the equipment used to perform the measurements which will follow:

Linear dipole antenna constructed in house (Figure 3-1). This dipole consists of a coaxial connector mounted on a sheet of epoxy plastic, which does not affect the radiation pattern. This was tested by placing a sheet of epoxy plastic between a transmit and a receive antenna and measuring the attenuation to the measured signal – no attenuation was observed. A wire is soldered to the center conductor pin of the coax connector and another wire is soldered to the outer shield, thus constructing the dipole. The total length of this dipole is 12cm, which corresponds to a half-wavelength frequency of approximately 1.25GHz and a quarter-wavelength resonant frequency approximately 625MHz. This length was initially chosen because 1.25GHz was a simple frequency to make preliminary measurements with because of its short wavelength, allowing for a compact antenna and compact measurement area.

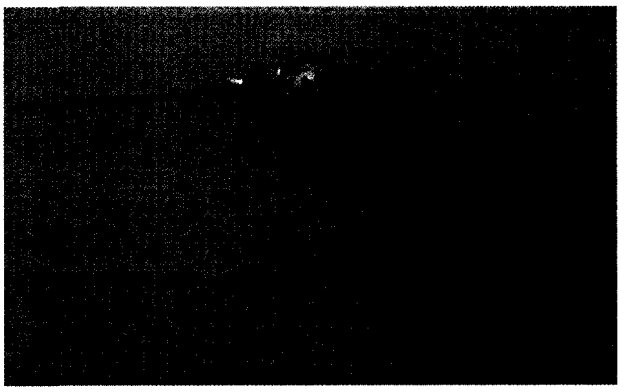

Figure 3-1 Dipole antenna 12cm in length constructed in-house with half-wavelength resonance frequency of 1.25GHz

HZ-11 Probe Set For E and H Near Field Emissions (Rohde and Schwarz, Munich, Germany). This probe set is designed to measure near field RF emissions; the small size and good sensitivity of these probes make them ideal for near field measurements. It is comprised of 5 field probes (2 electric and 3 magnetic), a 20 cm extension handle, and a preamplifier [2]. The selectivity of the probes makes them suitable for near field measurements where the electric and magnetic field components need to be measured separately. However, only the 6cm loop probe and the ball probe (Figure 3-2) were used in the experiments to follow. These two probes were chosen because they have the largest frequency responses (100 kHz to 500 MHz) of the probes in the set and therefore the most suitable for the measurements.

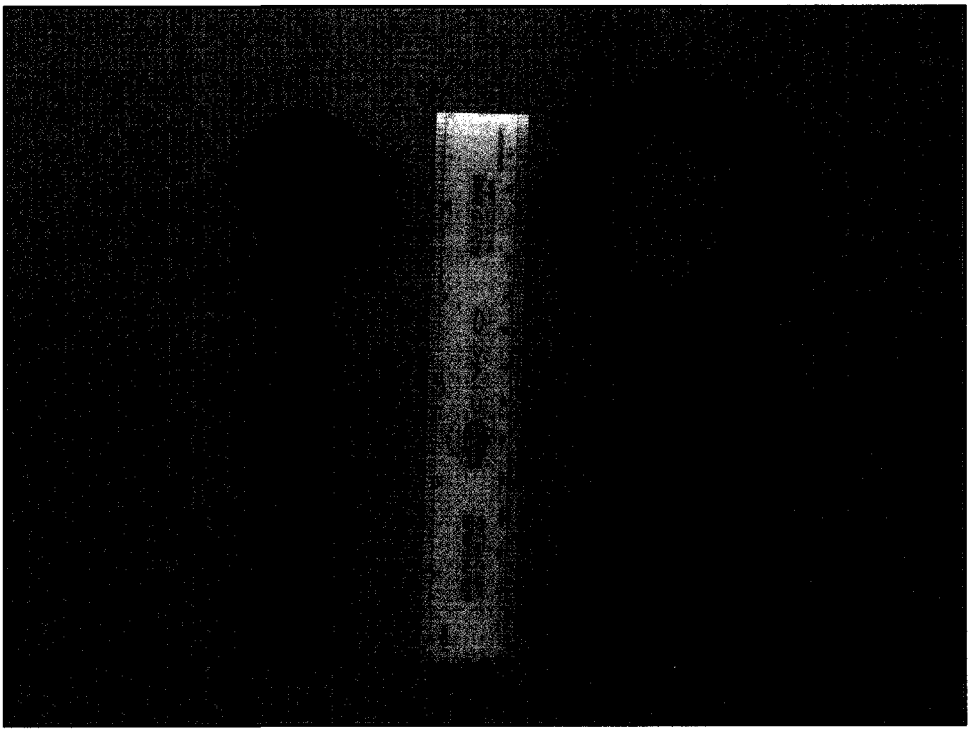

Figure 3-2 Rohde and Scwarz HZ-11 field probes: ball probe (left) and loop probe (right)

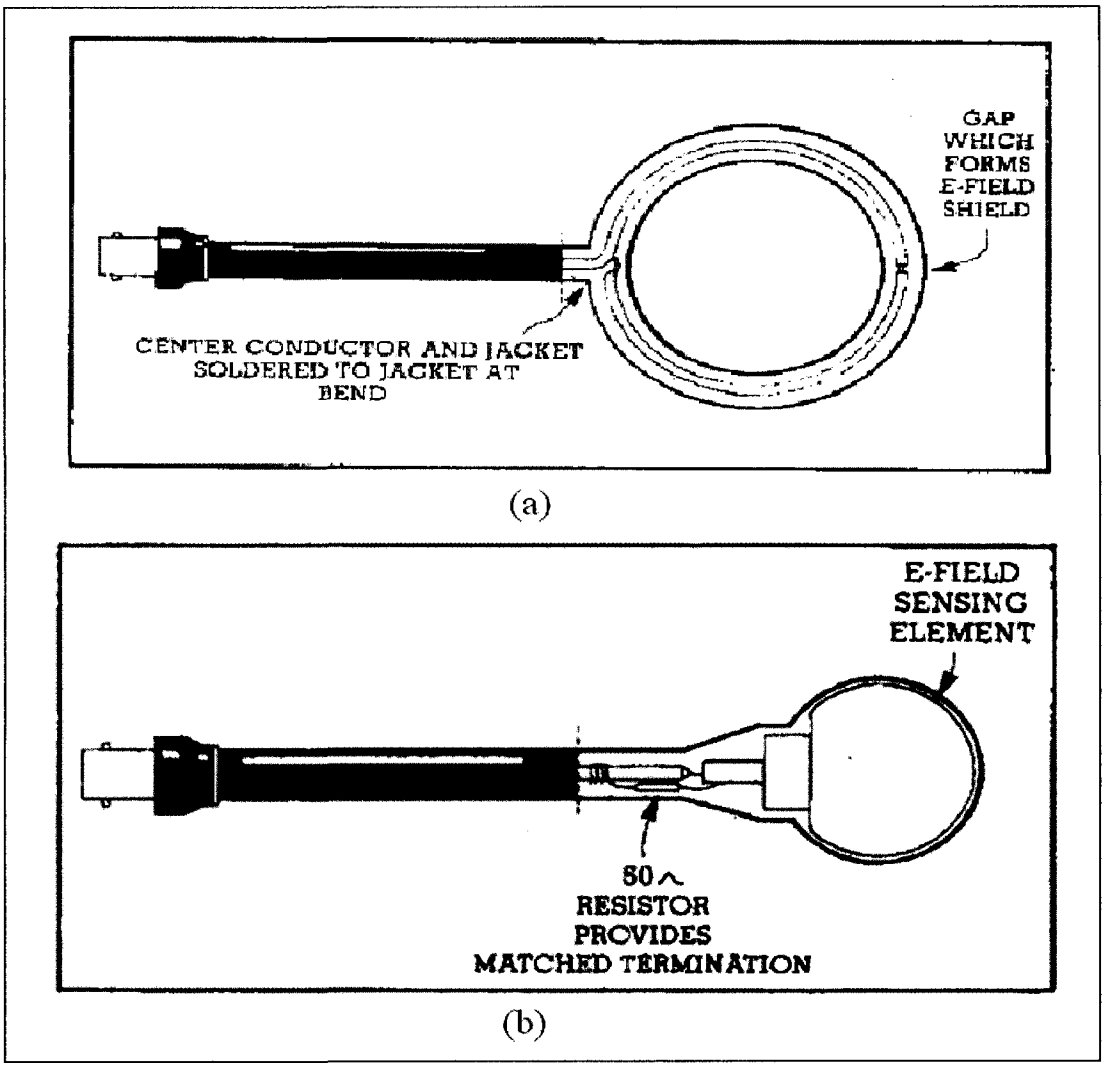

Figure 3-3 Loop (a) and Ball (b) probe [© Rohde and Schwarz, 2008 with permission]

The ball probe (model 904) is an E field probe and will reject the H field with up to 30dB of E/H rejection. Seen in Figure 3-3b, the ball probe consists of a coaxial cable with a 50 ohm termination, to provide a nominal match to the coaxial line. The E field sensing element is a hollow metallic ball connected through a 50 ohm resistor to the outer shield of the coaxial line. Inside this ball is an insulator into which the center conductor of the coax is extended. This essentially creates a capacitive relationship between the metallic

ball and the center conductor. The electric field seen by the metallic ball will induce a charge on the surface of the ball. The E field is then determined by measuring the potential difference between the center conductor and the metallic ball. The H field is preferentially rejected because there are no closed loops for the current to flow in, hence no magnetic induction can occur. An approximation of the representative circuit can be seen in figure 3-4.

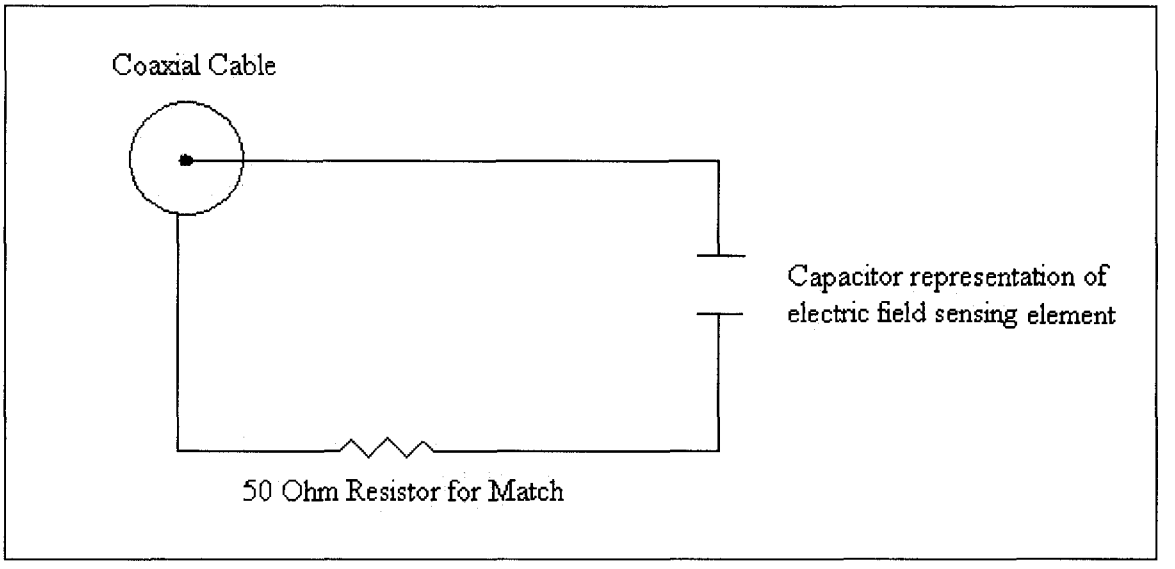

Figure 3-4 Circuit approximation of electric field probe

The loop probe (model 901) is an H field probe and will reject the E field with up to 41dB of H/E rejection. Seen in Figure 3-3a the loop probe consists solely of a 50 ohm coaxial line which is looped and 360 degree soldered to the outer shield of the coaxial cable. Without modification this would cause a short in the circuit; however, there is also a gap which is cut into the outer shield at the high point of the loop, this gap creates a balanced electric field inside of the loop and thus the loop will preferentially reject the

electric field. It also allows the center conductor to form a closed current loop through which the H field can be measured via Faraday's Law of induction [3]

$$\varepsilon = \oint \overline{E} \cdot \overline{dl} = -\frac{d\Phi}{dt} \tag{3-1}$$

where ε is the EMF, E is the electric field and Φ is the magnetic flux through the loop. Faraday's Law is one of Maxwell's equations and can be written more generally as follows [3 and Eq. 2-5]:

$$\overline{\nabla} \times \overline{E} = -\frac{\partial \overline{B}}{\partial t} \tag{3-2}$$

The field probes are geometrically calibrated. This means that one set of probes is built and properly calibrated in a TEM cell (an enclosed device which generates an electromagnetic field with known properties) [2], where they are exposed to a plane wave (377ohm) field and their frequency response is graphed. This response is represented by their performance factor (PF) in units of dB, which relates the voltage induced in the probe to the field strength that the probes are exposed to.

$$PF_{dB} = 20\log\left(\frac{E}{V}\right) \tag{3-3}$$

Where E is the field strength and V is the voltage induced. The rest of the probes distributed are constructed in an identical fashion but are not individually calibrated. This geometrical calibration introduces errors in the field values which would be larger than those seen on individually calibrated field probes. The performance factors of the ball probe and of the 6 cm loop probe can be seen in Figure 3-5 [2] and the thickness of the lines indicates the uncertainty in the values. This leads to a performance factor error of at

least ± 1dB. The loop probe performance factor is shown as the equivalent electric field response; this is done using the fact that the calibration field impedance was 377 ohms, and so to obtain the proper H field value 51.52 dB must be subtracted from the displayed performance factor. This value comes from the E/H ratio, $20 \cdot \log(377) = 51.52\ dB$. The units of the E and H fields calculated from the measured voltage and performance factor are Volts per meter and Amps per meter, respectively.

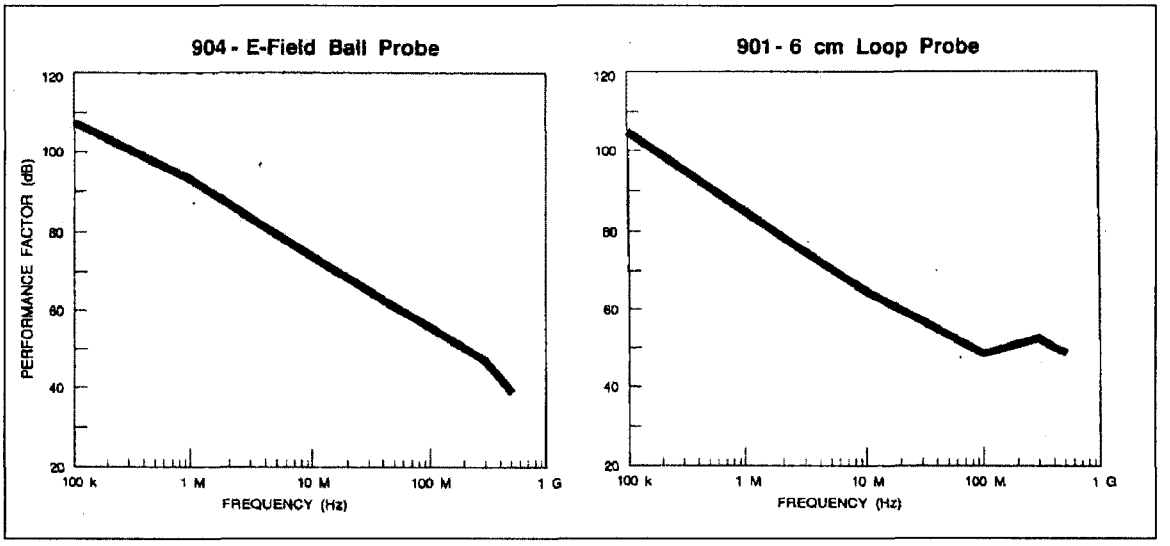

Figure 3-5 Performance factors for the ball probe (E) and 6 cm loop probe (H)

[© Rohde and Schwarz, 2008 with permission]

Network/Spectrum/Impedance Analyzer (Agilent 4396B 1.8 GHz, Agilent Technologies, Santa Clara, California, USA): This system was used in the spectrum analyzer setting. It has a frequency range of 100 kHz to 1.8 GHz. The 4396B can be used as a network analyzer for testing network equipment, as a spectrum analyzer for frequency analysis of input signals, and as an impedance analyzer. Combined with the transmission/reflection test set (Agilent model 87512A) the network analyzer can

measure the transmitted and reflected power characteristics of a device, including a transmit antenna, and can measure the signal loss along a coaxial line. When used in the spectrum analyzer mode, it can be used for robust, accurate frequency analysis with an accuracy level of ±0.12 dB in the frequency range of interest. The input ports for the analyzer are matched to 50 ohms through a simple matching circuit shown in figure 3-6, where R_S is the impedance of the source, in our case a 50 ohm coaxial cable, and R_L is the impedance of the load, represented as a 50 ohm resistor.

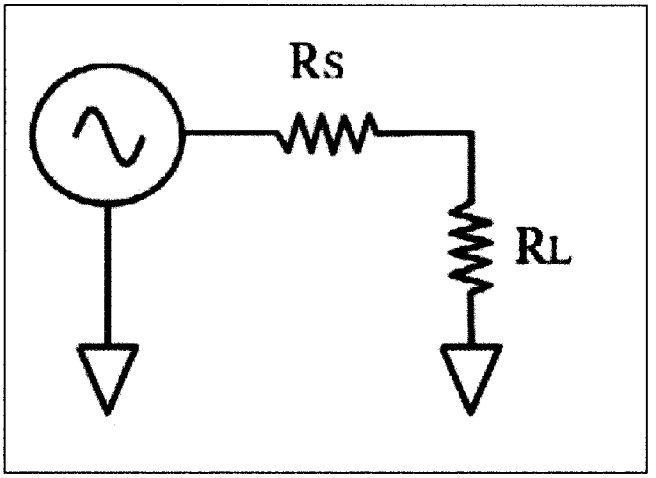

Figure 3-6 Impedance matching circuit for 4396B analyzer

An **Oscilloscope** (Agilent DSO6104A , Agilent Technologies, Santa Clara, California, USA) for measuring time-domain data. This scope has 4 analog input channels, a maximum bandwidth of 1 GHz, a maximum sample rate of 4 Giga-samples per second and an update rate of 100,000 waveforms per second. This scope allows for the rapid acquisition of several waveforms simultaneously and easy comparison of signals. The inputs have variable impedance values of either 50 Ω or 1 MΩ, depending on the type of input. Waveform averaging and instant mathematical operations (e.g. Fast Fourier

Transform) are also possible. The oscilloscope was ideal for making the time based measurements performed in later chapters.

A **Signal Generator** (Agilent E4400B ESG Series, Agilent Technologies, Santa Clara, California, USA) used as the frequency source for the transmit antenna. Provides a continuous sinusoidal output signal with selectable frequency (250kHz to 1Ghz) and power level (-136dBm to 13dBm). Provides a constant, steady signal that is ideal for use as a power source for the antenna transmitters used in this thesis. Output port is a simple coaxial port and is matched to 50Ω.

A **wooden antenna stand designed (Figure 3-7) and constructed in house**. This stand has three purposes: first, to support the transmit antenna (dipole, Figure 3-1) and the field probes (Figure 3-2); second, to provide a setup which would facilitate the measurement of the dipole's radiation pattern; and third, to assure measurement reproducibility and consistency. Prior to construction, possible materials were tested to assure sufficient RF transparency so that the stand itself would not alter measurements. Materials tested were wood and Delrin™.

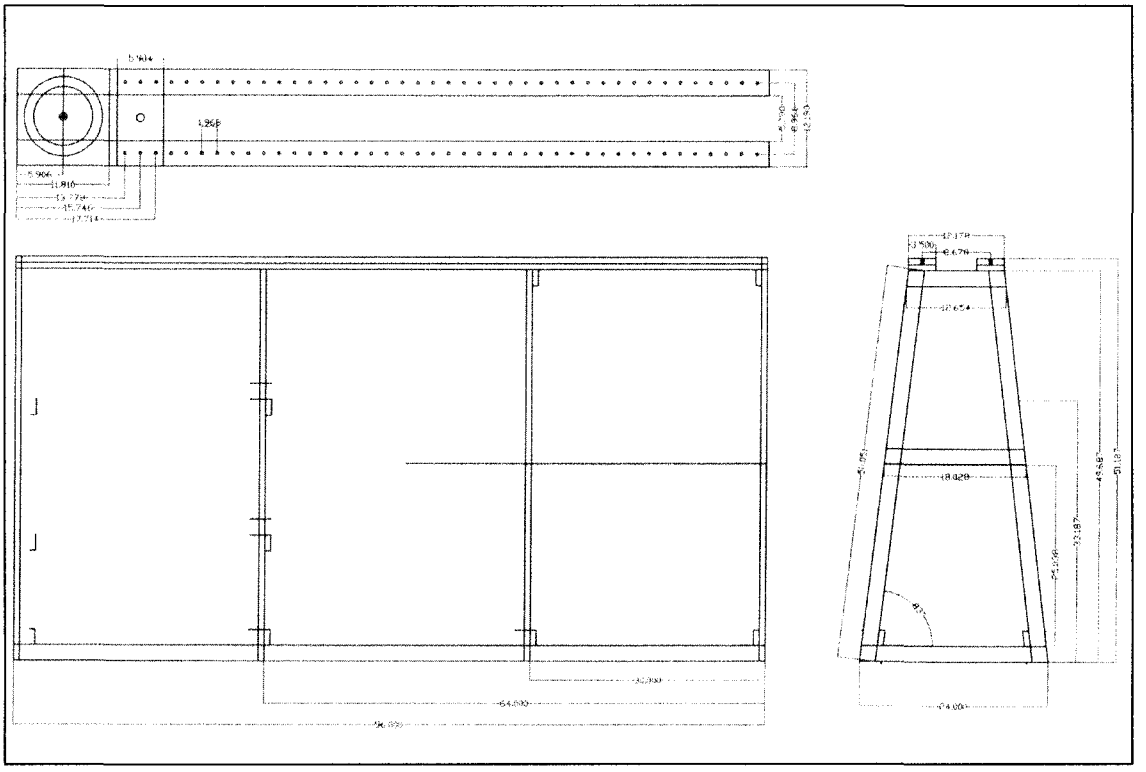

Figure 3-7 Autocad depiction of antenna stand

3.1.3 Materials testing for antenna stand

Appropriate stand materials must be sufficiently RF transparent, which means that they have high transmission so that they will not attenuate the signal, and low reflection so that their presence will minimally alter the measurements. To test the RF transparency of wood and Delrin an experiment was devised to measure the effect these materials would have on antenna measurements. Figure 3-8 shows the different setups used to accomplish this goal. A dipole was used as the transmitting source and a loop was used as the receiver, both of which were constructed in-house. The dipole antenna can be seen in Figure 3-1. The loop antenna was constructed using a single piece of wire and a coaxial connector attached to a piece of epoxy plastic (as with the dipole). One end of the wire

was soldered to the center conductor of the connector, and the other end was soldered to the outer shield (see Figure 3-9). The diameter of the loop is 10 cm and was chosen so that the loop would be compact. The setup included placing an obstruction (made of wood or Delrin) between the source and receiver in four different locations: close to the transmitter, halfway between the source and receiver, close to the receiver, and behind the receiver. These are numbered 1 through 4, respectively, in Figure 3-8. Measurements were then taken in an alternating fashion, first with obstruction and then without obstruction. This was repeated for each obstruction position, and for both wood and Delrin. The results are shown in Figures 3-10 and 3-11. The errors in these figures were calculated by calculating the standard deviation as follows, where x is the data point, $\bar{x}$ is the mean of the data, and n is the number of data points.

$$error = \sqrt{\frac{\sum (x - \bar{x})^2}{(n-1)}} \tag{3-4}$$

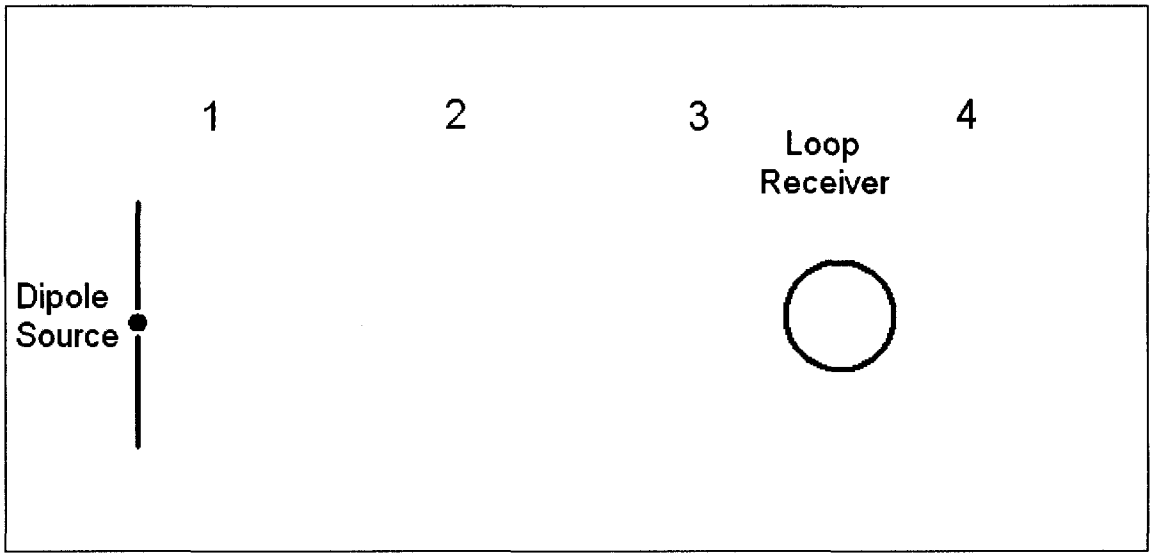

Figure 3-8 Obstruction measurement setup

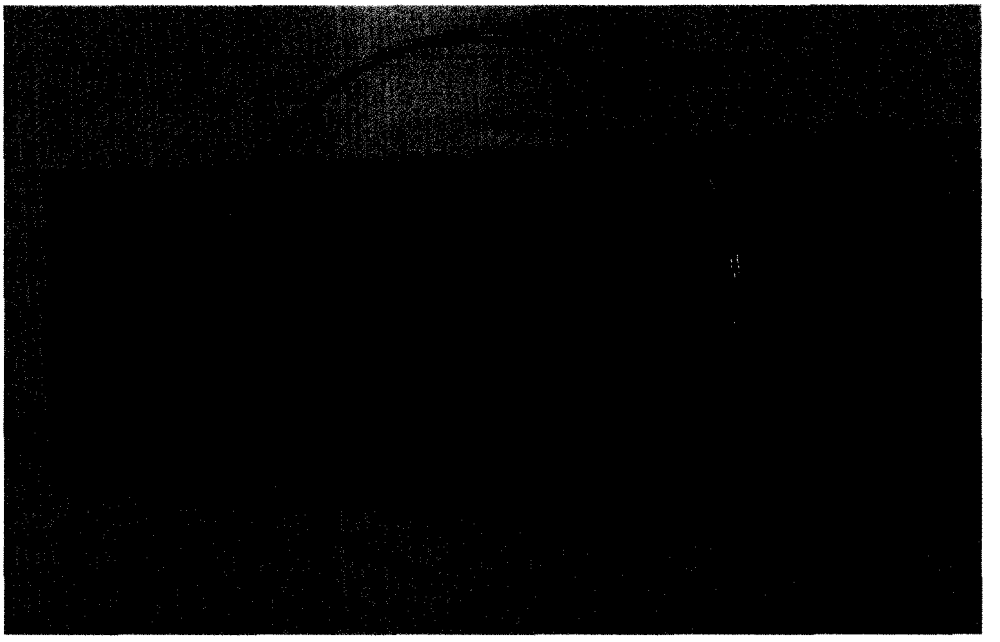

Figure 3-9 Loop antenna receiver

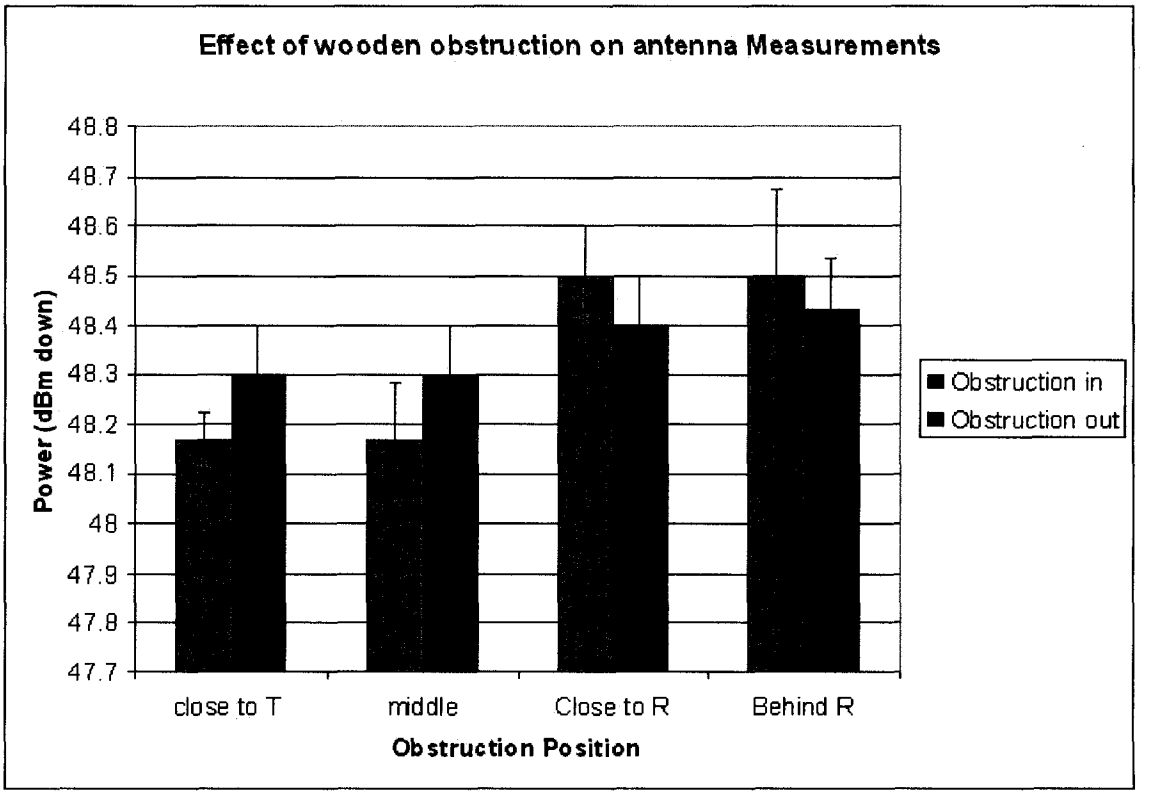

Figure 3-10 Obstruction measurements with wood

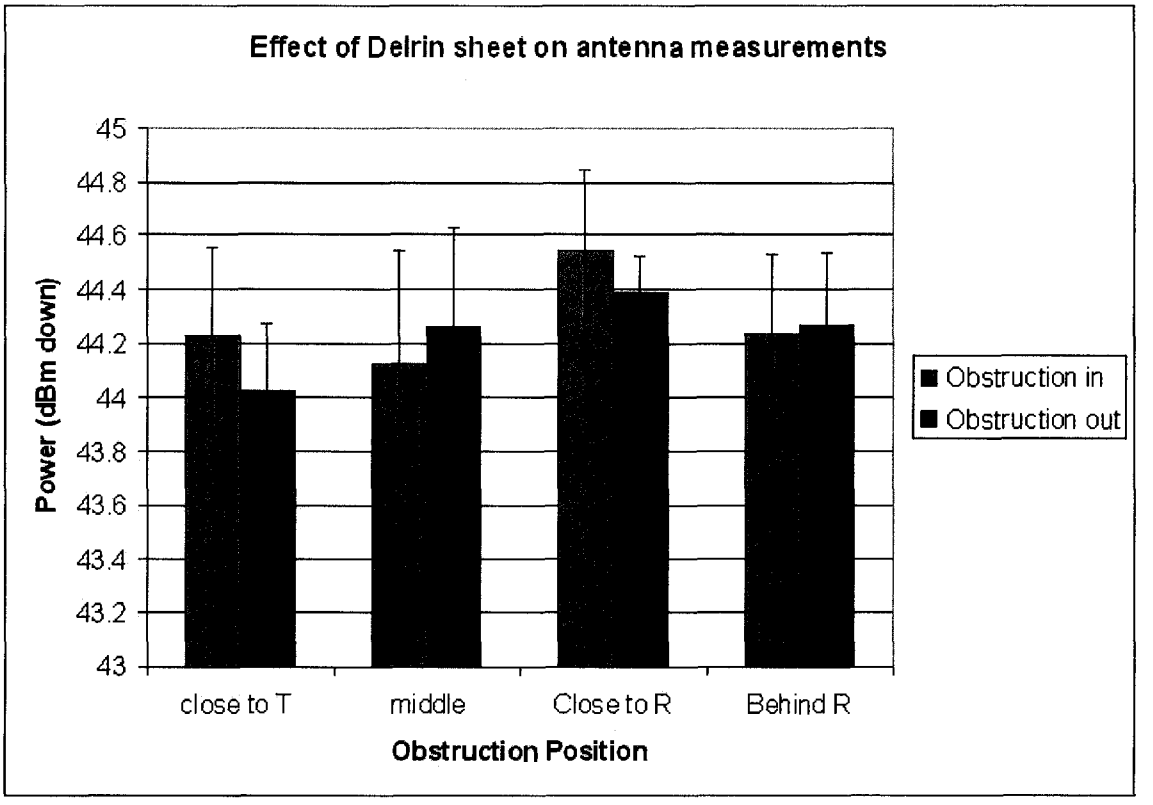

Figure 3-11 Obstruction measurements with Delrin

Figures 3-10 and 3-11 show that wood and Delrin have negligible effects on the antenna measurements. Both materials display values which are within error of the measurements taken with no obstruction present. Both of these materials would be appropriate for use as construction materials for the antenna stand. The antenna stand was constructed according to the schematic in Figure 3-7, using wood for the frame and Delrin for the antenna supports. The structure was glued together to avoid any deleterious effects that metal nails/screws could have. The finished structure is shown in figure 3-12. The transmit stand is capable of rotating to allow for precise, reproducible measurement of the angular radiation pattern of the source. There are angular gradations which allow for known rotation angles. Also, the receive stand has plugs which fit into the holes on top of

the stand (see Figure 3-7) allowing the precise, reproducible measurement of the radiation pattern dependence on radial distance. These two types of measurements will enable the comparison of the measured dipole radiation pattern to the theoretical dipole radiation pattern.

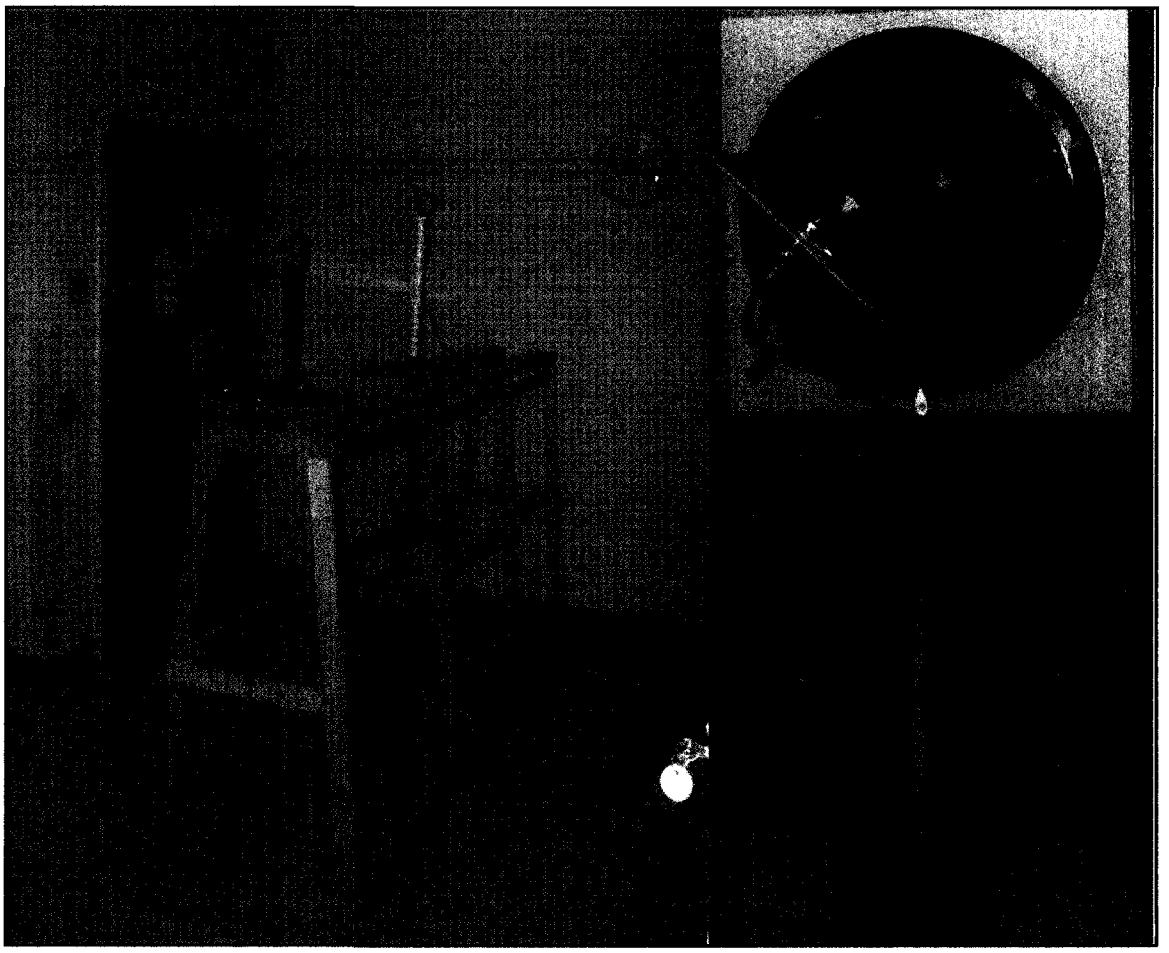

Figure 3-12 Constructed Antenna stand – showing entire stand (left)

Transmit stand (top right) and Receive stand (bottom right)

3.1.4 Note about transition to linear accelerators

Because of the poor time-response triggering of the spectrum analyzer, it was not used as a measurement tool for the linear accelerator measurements. As stated in [2], an oscilloscope may also be used in conjunction with the field probes. Some basic, controlled measurements were taken to assure that the same result would be obtained when moving to an oscilloscope.

The measurement setup involved using the frequency generator to output a signal at several different frequencies, at a power level of -2dBm. This signal was sent directly into either the oscilloscope or the spectrum analyzer and the results are shown in Figure 3-13. Errors were calculated from values found in [2] and [4].

Figure 3-13 shows that there is very little difference between the voltages measured by the two devices, provided the RMS value is used for the scope, with an average difference of 0.002V and a standard deviation of 0.004V. The voltage change measured with frequency, resulting in the slope of the plots seen in Figure 3-13, is due to the frequency response of the cable and not the devices themselves. With the total output power of the signal generator being -2dBm, corresponding to a voltage of 0.178V, it can be seen that the spectrum analyzer actually measures a voltage higher than this for low frequencies (.5, 1, 10MHz), while the scope never measures a voltage greater than 0.178V. This could be a small calibration error on the spectrum analyzer, though even the highest value is within error of 0.178V.

Figure 3-13 shows that both the oscilloscope and the spectrum analyzer provide results which are consistent and as such are both suitable for these types of measurements. Both systems offer different advantages: the spectrum analyzer provides better signal to noise for frequency measurements and is more effective than the oscilloscope at low power levels. For example, the results in section 4.1 could not have been obtained with the scope as the voltages induced in the field probes due to the dipole were below the threshold of the oscilloscope. However, the spectrum analyzer triggering is not sensitive enough for use with the short pulse lengths of the linear accelerators. In this case the better time response of the oscilloscope will be desired. Also, the linear accelerators will have power levels that are much higher, and so the higher sensitivity of the spectrum analyzer is not required as it was at lower power levels.

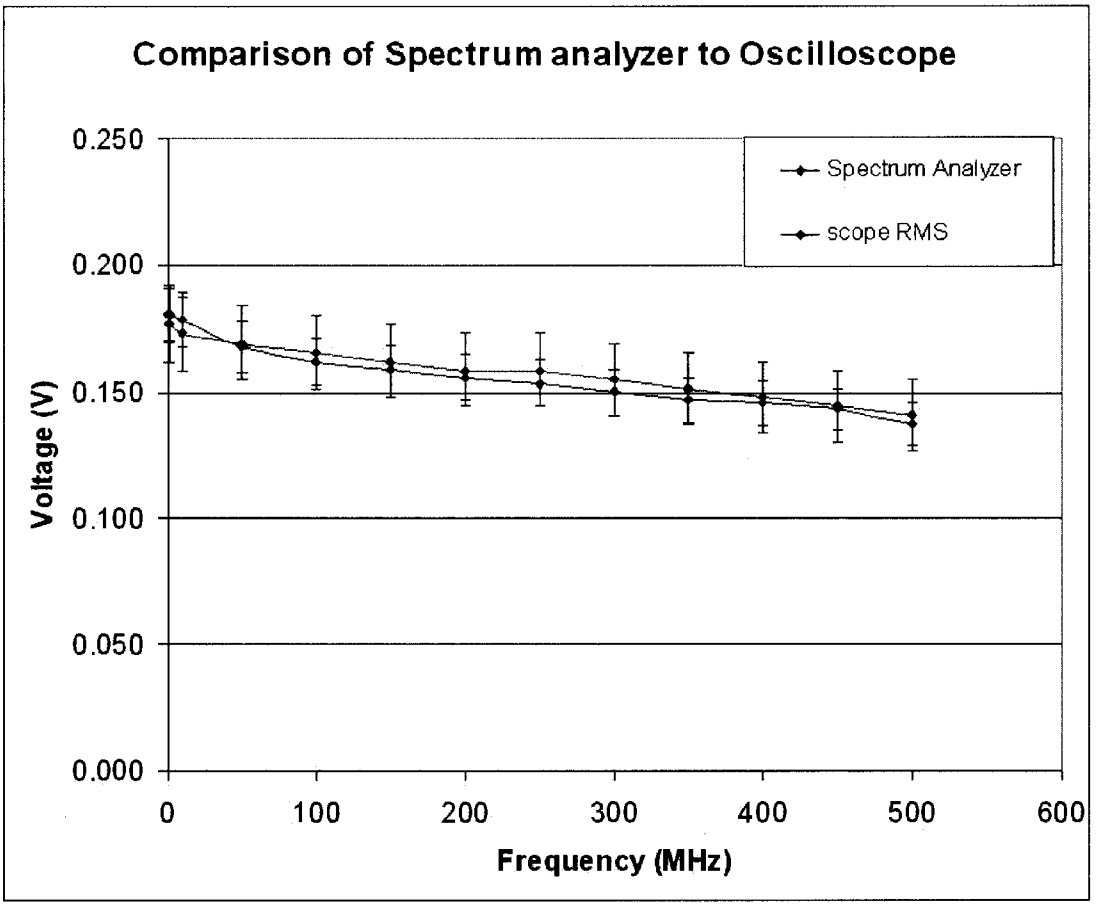

Figure 3-13 Comparison of voltages measured by the spectrum analyzer and the oscilloscope

3.2 Linear Accelerator Measurements

3.2.1 Introduction

In order to effectively make the linac and MRI systems functionally independent, the RF emissions of the linac must be shielded from the RF coils of the MRI. The major source of RF noise emanating from the linac is the pulse modulator, whose detailed function is described in section 2.3. During the pulse discharge, and subsequent charging cycle, there are several transient currents and voltages in the PPM which could lead to RF emissions. The hypothesis to be explored here is that these transient signals, which can be seen through monitoring various PPM test signals described in 2.3, are responsible for the RF emanating from the system. The objective of the experiments described in this chapter is to measure the electric and magnetic field components of these emissions. The two components must be measured separately because they will be measured in the near field region and as such will not have a simple relationship to each other (see section 2.1.4). These measurements will be used to quantify the magnitude and frequency spectrum of the electric and magnetic field signals. The magnitudes will not be quantified to a high degree of accuracy; the objective is to obtain information on the order of magnitude of emitted signals along with the frequencies of maximum emission. This information is crucial to determining the effect of this interference on the MRI system; whose RF coils receives signals on the order of microwatts from patients [7] during imaging.

3.2.2 Equipment

The majority of the equipment used for these experiments is described in section 3.1.2 and as such their descriptions will not be repeated here. As mentioned above the

measurements to follow were made on a medical linear accelerator, in this case a Varian 600C (Varian, Inc., Palo Alto, California, USA) powered by a magnetron microwave source (see section 2.2 for detailed functioning). Before discussing the experimental setup, it is important to note that two distinctly different types of measurements were taken: internal and external. The internal measurements refer to the various test signals obtained directly from the PPM, while the external measurements refer to the field probe measurements.

The internal measurements were taken by connecting one end of a coaxial cable to the test output connector on the linac control panel and the other end to the oscilloscope. The signals were then measured while the linac was pulsing to produce pulsed radiation. The traces were transferred from the oscilloscope to a PC with a Keithley KUSB 488 (Keithley Instruments Inc, Cleveland, Ohio, USA) GPIB interface. The data was acquired using a software program DADiSP (DSP Development Corporation, Newton, Massachusetts, USA). On the 600C unit there were three signals of interest: the pulse forming network (PFN) voltage, the high voltage power supply (HVPS) current (also called charging current), and the magnetron current (section 2.3). Samples of these signals can be seen in Figures 3-14 and 3-15. Figure 3-14 shows the signals on a millisecond timescale which represents a complete pulsing (discharge/charge) cycle of the linac. Figure 3-15 is shown on a microsecond timescale and only shows the discharge portion of the cycle, which occurs at approximately 0.55ms in Figure 3-14.

The external measurements were taken by connecting the field probes to the oscilloscope via coaxial cable. The traces were again transferred to a PC with the Keithley GPIB interface and DADiSP. Samples of these signals can be seen in figures 3-16 and 3-17. Figure 3-16 shows the signals on a millisecond timescale which represents a complete pulsing (discharge/charge) cycle of the linac. Figure 3-17 is shown on a microsecond timescale and only shows the discharge portion of the cycle, which occurs at approximately 0.55ms in Figure 3-16.

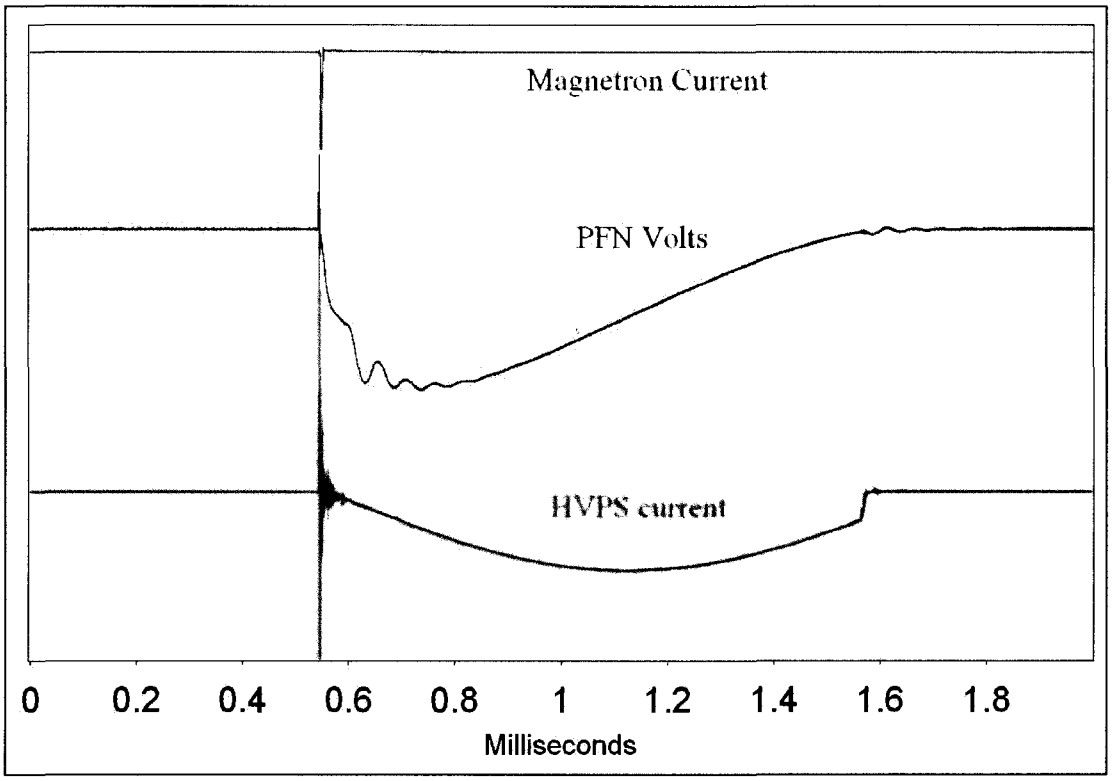

Figure 3-14 Magnetron Current (pink), PFN voltage (red) and HVPS current (cyan) on ms timescale

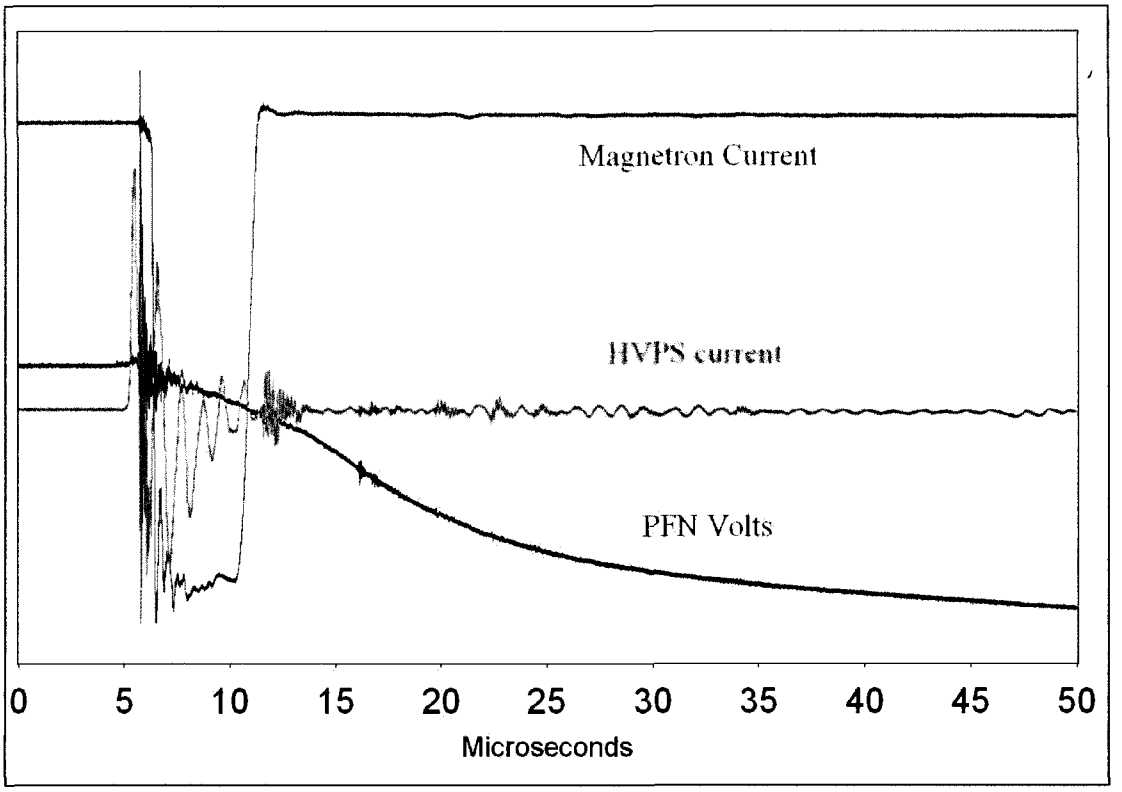

Figure 3-15 Magnetron current (pink), PFN voltage (Red) and HVPS current (cyan) on a μs timescale

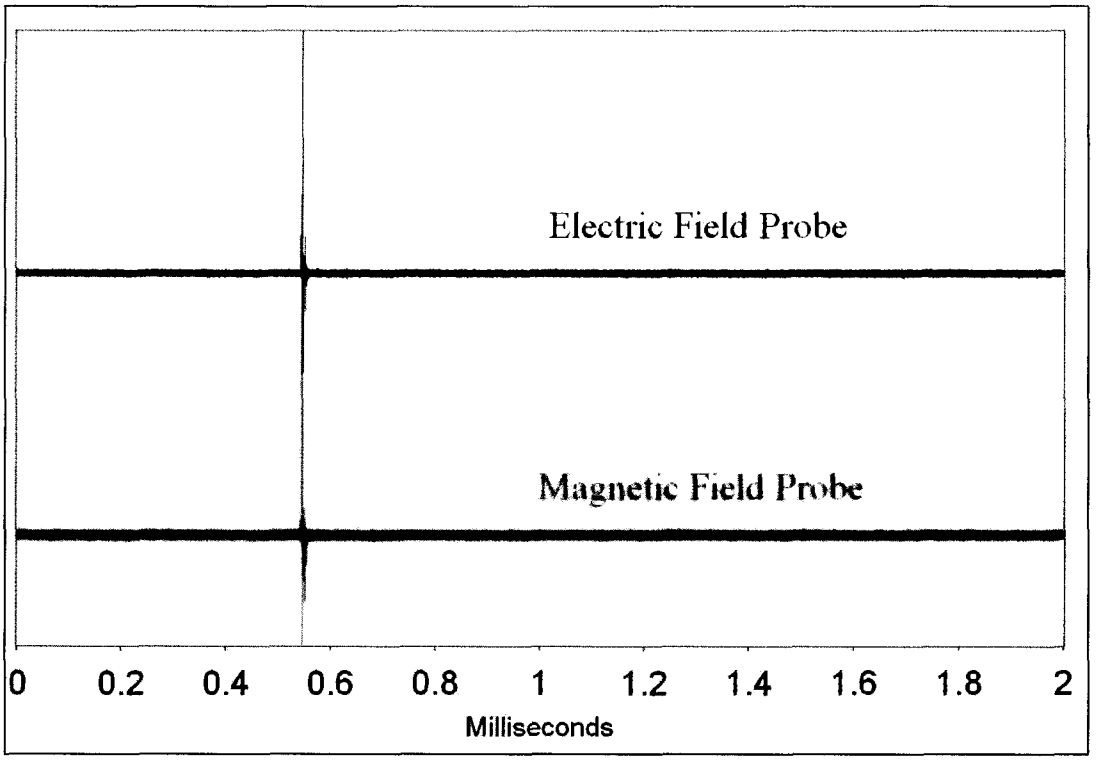

Figure 3-16 Electric field probe (blue) and magnetic field probe (green) signals on a ms timescale

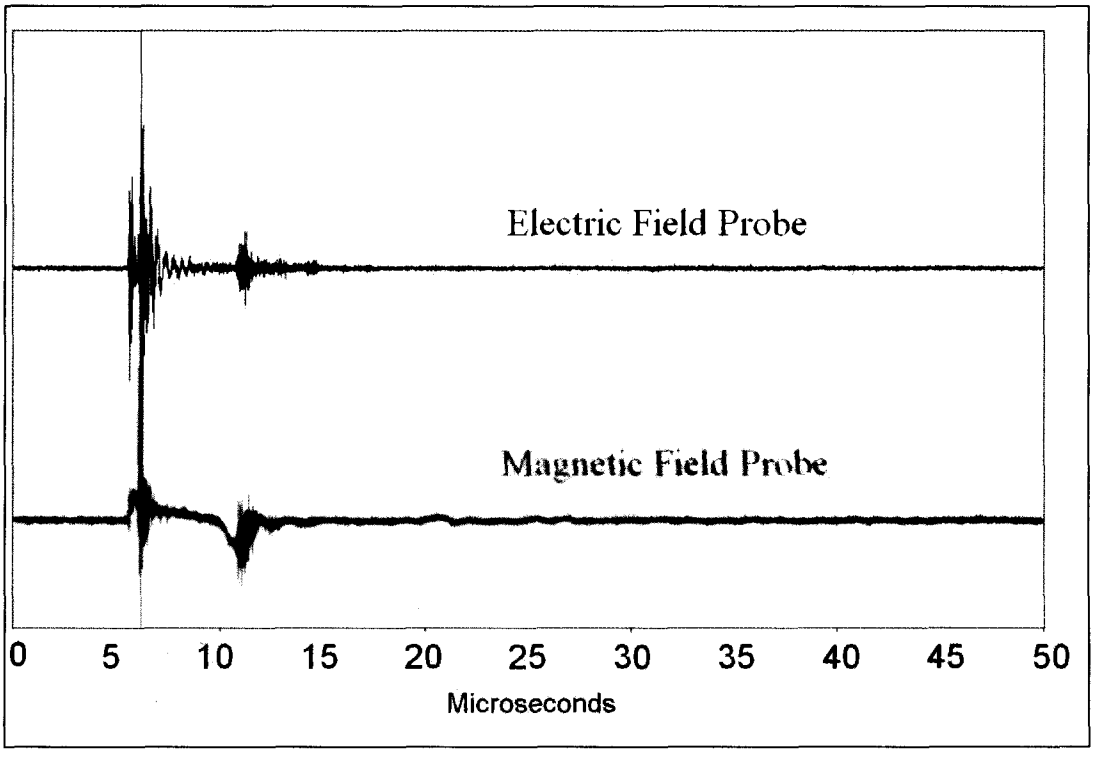

Figure 3-17 Electric field probe (blue) and magnetic field probe (green) signals on a μs timescale

3.2.3 Measurement setup

These measurements were taken in the newly renovated MR-linac vault that houses a refurbished 600C linac (Varian Medical Systems). The experimental setup for the measurement of electric and magnetic fields emitted by the PPM can be seen in Figure 3-18. The PC and the oscilloscope were both set up near the control panel so that the internal measurements could easily be taken. The control panel contains the computers and software required to control and operate the linac; it is located outside of the linac vault. The measurement probes were place beside the modulator cabinet, which was also outside of the linac vault. The measurement probes were connected via coaxial cable to the oscilloscope, which was triggered using the system SYNC pulse. This pulse is internally generated and pulses nominally at a rate of 180 Hz (~ every 5.6 ms), but the pulse output frequency varies depending on the dose rate. When the linac is functioning normally the dose servo will drop pulses to maintain the preset dose rate. This pulse dropping is not desirable for our measurements because if the pulse is dropped, no signal is seen on the oscilloscope. Therefore the dose servo control setting was turned off and the dose rate was set to the maximum at 250 monitor units per minute (MU/min) so that only minimal pulses would be dropped. With the servo turned off and the dose rate set to 250 MU/min the linac will only drop 1 out of 6 pulses regularly and so will generate a measurable oscilloscope signal the majority of the time. The linac was then turned on and the oscilloscope was manually stopped to acquire the data traces; these were then transferred to the PC. The oscilloscope was then returned to RUN mode and the process was repeated, acquiring 16 separate traces to allow DADiSP to average the signals, for each of the following five signals: electric field probe, magnetic field probe, HVPS

current, magnetron current, and PFN voltage. Sixteen signal averages were used because adequate noise reduction was achieved with this number.

It should be noted that the test points on a linac do not directly measure the large voltages and currents present inside the modulator. It is not generally possible to measure a large voltage using an oscilloscope directly. The test points all represent scaled currents and voltages which retain the shape of the original signals, which in the case of this thesis is the important information. Therefore, the PFN voltage test point is located at the output of a simple voltage divider realized solely of resistive components thus making the measurement directly proportional to the absolute PFN voltage without distorting its pulse shape. Similarly, the HVPS current is measured as the voltage across 1 ohm resistance through which a fraction of the HVPS current flows. Thus the measured voltage across the resistance is directly proportional to HVPS current. The high magnetron current is measured using a non-invasive inductive type of current probe already connected to this particular test point.

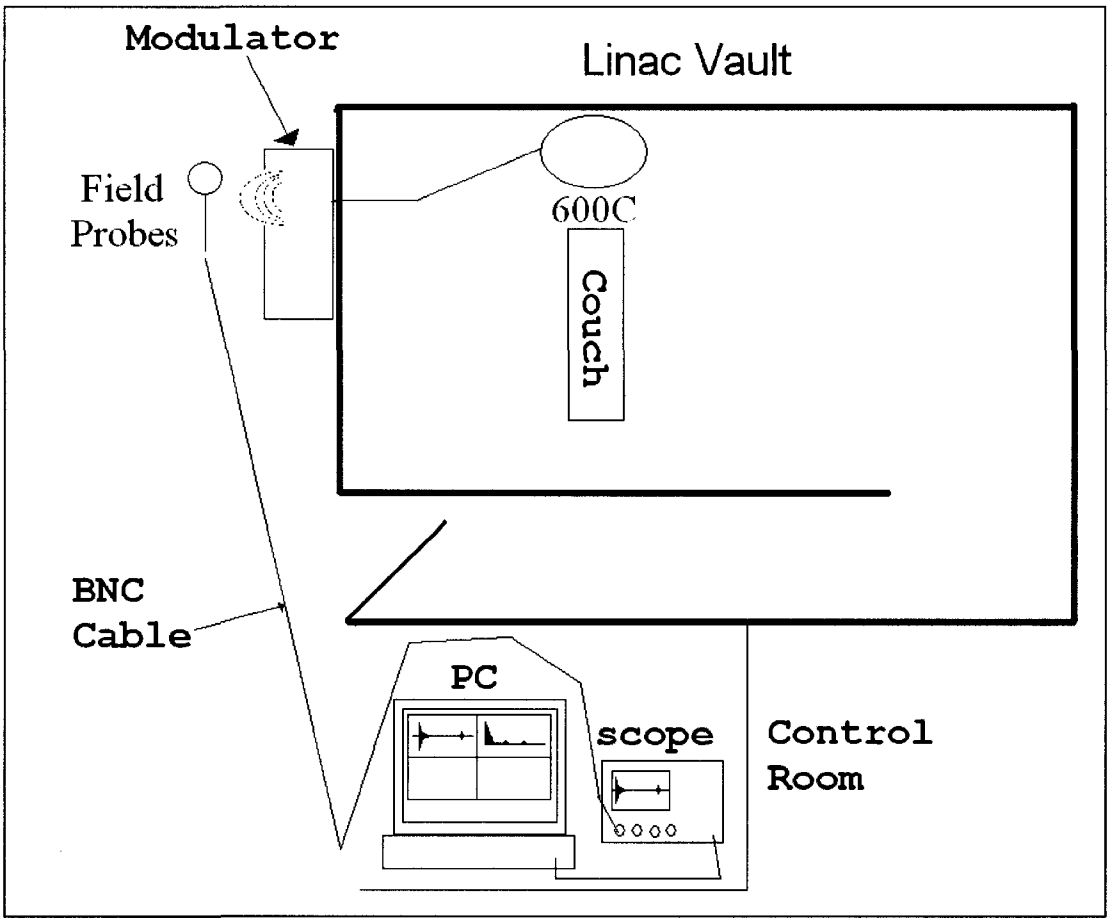

Figure 3-18 Measurement setup for MRIL field measurements

References:

1. Balanis, C. A., *Antenna Theory: Analysis and Design 2nd Edition,* Wiley & Sons, New York, 1997.
2. *Operating Manual for HZ-11Probe Set*, Rohde & Schwarz: Instrument Division. Munich, Germany.
3. Griffiths, D. J., *Introduction to Electrodynamics 3rd Edition,* Prentice Hall, New Jersey, 1999.
4. *Agilent 4396B Network/Spectrum/Impedance Analyzer Data Sheet.* Agilent Technologies, Santa Clara, California, 2003.
5. *Agilent Technologies InfiniiVision 6000 Series Oscilloscopes Data Sheet.* Agilent Technologies, Santa Clara, California, 2003.
6. *Agilent ESG-A and ESG-D RF Signal Generators Data Sheet.* Agilent, Santa Clara, California, 2003.
7. ECRI Institute, "*Scanning Systems, Magnetic Resonance Imaging*". URL: http://docs.ksu.edu.sa/PDF/Articles34/Article340196.pdf , May 2003.

4 Results

4.1 Dipole Antenna Radiation Pattern Measurements

With the constructed antenna stand two types of experiments were performed to measure the radiation pattern of a dipole transmit antenna. The first, called radial measurements in this text, examines the radiation pattern dependence on distance from the source. The second, called angular measurements in this text, examines the radiation pattern dependence on angle with respect to the source. These results were then compared to the theoretical pattern of a dipole antenna. It is important to note that the measurement environment was a confined space with several objects in close enough proximity to cause reflections which could adversely affect the measurements. For example there are several large metallic objects present in the room, such as a refurbished linac and a large metal cabinet.

4.1.1 Simplification of theory

4.1.1.1 Angular measurements

The constructed dipole (Figure 3-1) has a total length of 12cm, which corresponds to a half-wavelength resonant frequency of approximately 1.25GHz and a quarter-wavelength resonant frequency approximately 625MHz. Figure 4-1 shows the theoretical angular dependence of the radiation pattern (equation 2-11) for dipole length of half-wavelength, quarter-wavelength, and eighth-wavelength; these correspond to frequencies of 1.25GHz, 625MHz, and 312.5MHz, respectively. It can be seen in Figure 4-1 that the radiation pattern of a dipole does not change drastically for radiation frequency values below $\lambda/2$ [1]. Also, the radiation pattern remains the same even if a convenient fraction of a

wavelength, such as 1/2, 1/4, and 1/8, is not used. The similarity in angular patterns will allow for a simple comparison of measured values to theory by allowing the use of the $\lambda/2$ pattern, rather than calculating the angular pattern for each frequency.

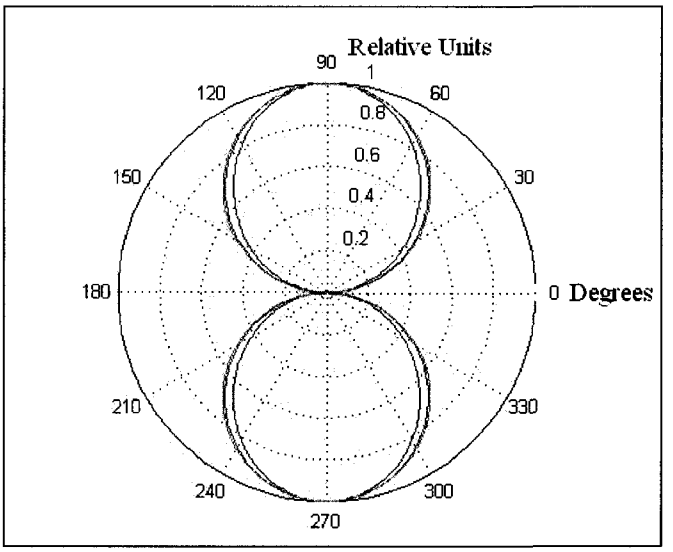

Figure 4-1 Theoretical angular dipole radiation pattern (Eq. 2-12) for dipole lengths of half-(blue), quarter-(red) and eighth-wavelength (green). The dipole is oriented along the horizontal (0-180 degree) axis and the circles represent the relative power scale normalized to unity at 90 degrees at a constant radial distance from the dipole center.

4.1.1.2 Radial Measurements

The field dependence on distance from the source can also be simplified for comparison to theory. Despite having two components and a complicated form, the electric field still bears a strong resemblance to an inverse radial distance (1/r) decay. This can be seen by plotting the total electric field, given by (taken from Eqs 2-14a and b):

$$E_{tot} = \sqrt{E_\rho^2 + E_z^2} \tag{4-1}$$

against the separation distance, r, and comparing it to an inverse decay.

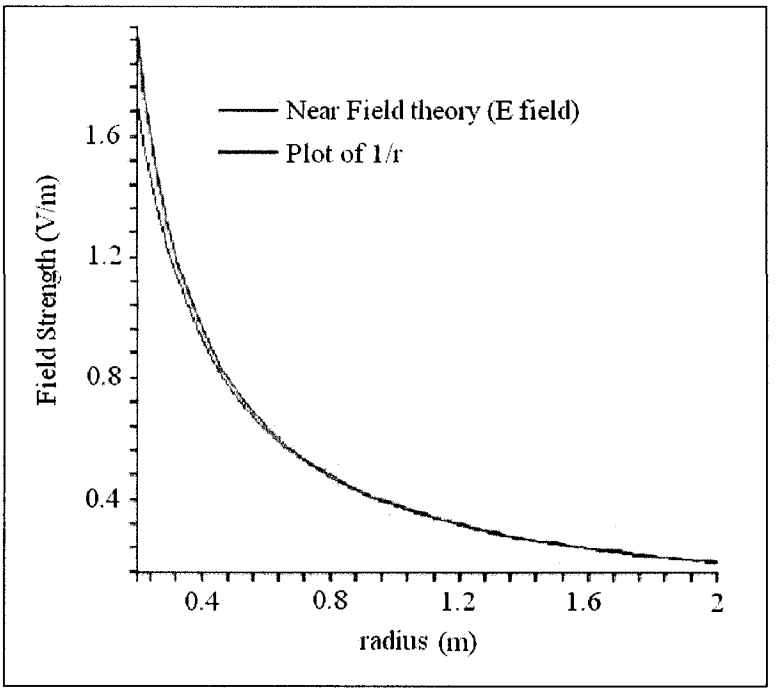

Figure 4-2 Comparison of near-field electric field to a 1/r type decay

Figure 4-2 shows almost no difference between the two graphs for most values of r and at small values of r exhibits a maximum difference of approximately 10%. As such it will be suitable for use as a comparison tool against the measured values. The current, I_0, (Eqs. 2-14a and b) was the only variable that was used for normalization and was set to a value which provided values comparable to the 1/r values.

4.1.2 Radial Measurements

Radial measurements were performed using a dipole antenna as the radiation source (Figure 3-1). This was placed in the Delrin transmit antenna stand (Figure 3-12) with the center of the dipole facing towards the receive antenna, along the length of the stand, corresponding to an angle, θ, of 90 degrees. The output signals sent to the dipole were

supplied by the signal generator at a single frequency and power level via 50Ω coaxial cable. The frequencies used were 400 and 500 MHz and the power supplied to the dipole was 1 mW (equivalently 0 dBm). Two different frequencies were used to examine the frequency dependence of these measurements. These frequencies were used because they were convenient values to use in conjunction with a colleague's simulations.

The field probes were used as the receive antennas and connected to the spectrum analyzer to measure the electric and magnetic field strengths of the dipole antenna at several separation distances. The separation distance was initially 20 cm and was incremented to a final distance of 190 cm. The increments were 5 cm until a distance of 100 cm was reached and then 10 cm increments were used. The values measured on the spectrum analyzer were in dBm (P_{dBm}) (dB is decibel and the m reflects the reference value is 1 milliWatt) and were then converted to field values via the performance factor using the following formula.

$$E = V \cdot PF \tag{4-2}$$

where E is the field value (in V/m or A/m) and V is the voltage measured by the spectrum analyzer calculated from P_{dBm} by:

$$V = \sqrt{P_W \bullet R} \tag{4-3}$$

$$P_W = \frac{10^{\left(\frac{P_{dBm}}{10}\right)}}{1000} \tag{4-4}$$

where P_W is the power in Watts, R is the resistance (50Ω) of the network analyzer input port and PF, in Eq. 4-2, is the appropriate performance factor in non-log form calculated from equation 3-3 by:

$$PF = 10^{\left(\frac{PF_{dB}}{20}\right)} \tag{4-5}$$

Once the performance factors were applied the data was plotted as field value versus separation distance. This was then compared to the 1/r relationship as per section 4.1.1.2. The results are shown for 400 MHz and 500 MHz in figures 4-3 (electric field) and 4-4 (magnetic field). It should be noted that for the electric field only one measurement orientation was required because of the isotropic nature of the ball probe. However, for the magnetic field three different orientations were used to acquire the 3 different (x, y, z) components of the field. The resulting measurements were added in quadrature to obtain the total magnetic field. The error associated with all measured values, E and H, are +/- 1.4%, which is derived from the error associated with the spectrum analyzer of .12 dBm.

In Figures 4-3 and 4-4 there is reasonable agreement between the theoretical radiation pattern and the measured one. Figure 4-3 shows that the electric field measurements appear to be much more susceptible to reflections due to the measurement environment. The maxima and minima seen in the measurement plots are likely due to areas of constructive and destructive interference, respectively. In Figure 4-4, it appears that reflections affect the magnetic field less than the electric field; there are fewer oscillations in the magnetic field measurements. In the 400 MHz magnetic field data (Figure 4-4) we can see that there is excellent agreement from 20 cm to 100 cm and then

some deviation between measurement and theory after that, while the 500 MHz magnetic field shows good agreement from 20 cm to 35 cm and again from 120 cm to 180 cm, but not as good between 35 and 120 cm. This shows that there appears to be some effects due to reflections still present in the magnetic field; they are just less prominent than for the electric field. The theoretical patterns represent what would occur in the absence of a physical room (i.e. in free space). Also, since it was not possible to determine the current, I_0 (equations 2-14a, b), the first value of the theoretical data was scaled to the first value of the measured data.

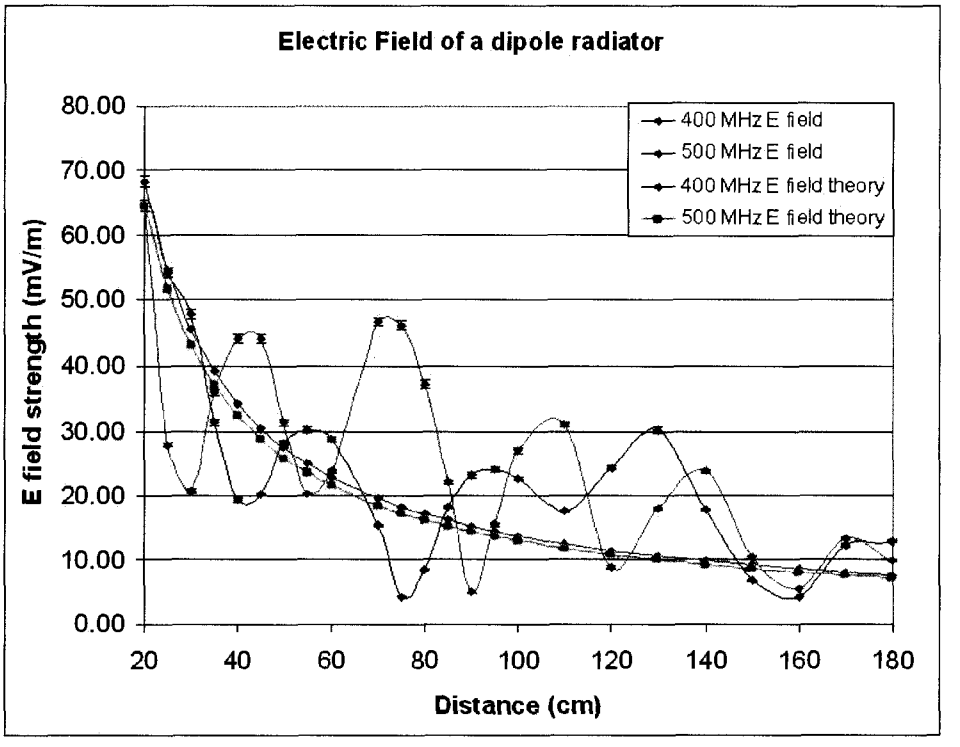

Figure 4-3 Electric field measurements and theory for a dipole radiating at 400MHz and 500MHz

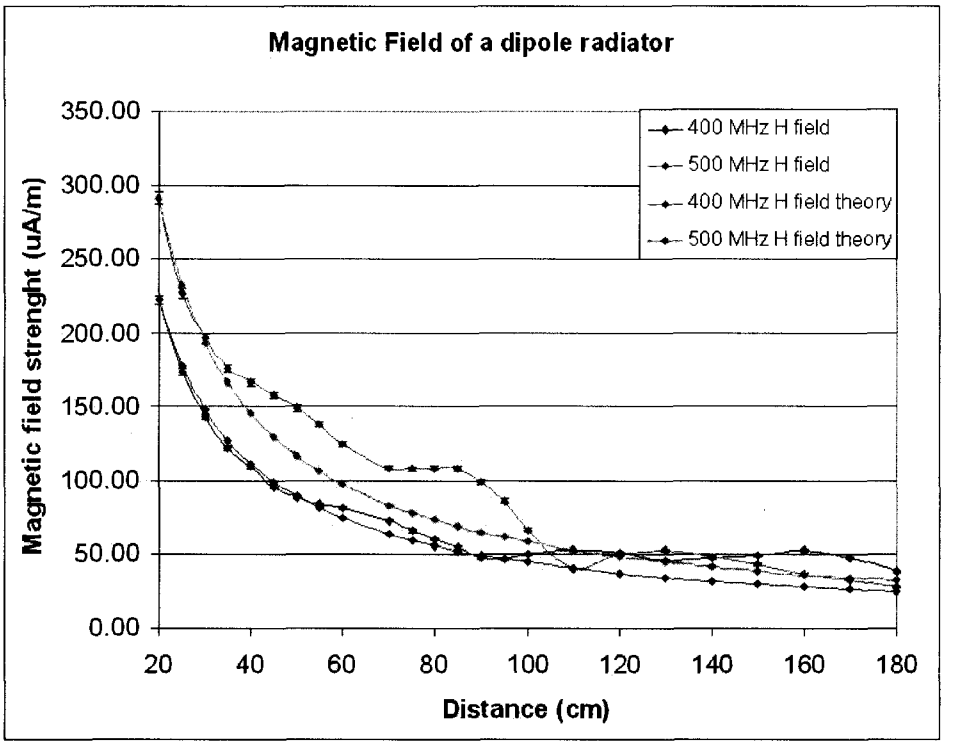

Figure 4-4 Magnetic field measurements and theory for a dipole radiating at 400MHz and 500MHz

It is postulated above that the wavelike nature of the radial electric field patterns seen in Figure 4-3 are due to reflections caused by the measurement laboratory. To investigate whether this was the case, the measurements were repeated in an open soccer field where the only deleterious effects anticipated would be ground reflections. The results are shown in Figures 4-5 and 4-6 compared to the in-room results from Figures 4-3 and 4-4. It is evident that there is a drastic difference between the in-room results and the measurements taken in the field. At 400 MHz there is a small oscillation around 75 cm, but much reduced from the in-room measurements. At 500 MHz there is a single oscillation that is more prevalent than at 400 MHz, but again the shape contains less oscillation than the in-room measurements. The slight oscillations seen in the

measurements taken in the field are likely due to reflections from steel and concrete which are located below the ground – the soccer field is located above a parking garage. The difference in response at the two different frequencies could be due to the composition or spacing of the steel/concrete supporting the reflection of one frequency more than the other; in this case the 500 MHz electric field seems to be more strongly reflected by the ground structure than the 400 MHz electric field.

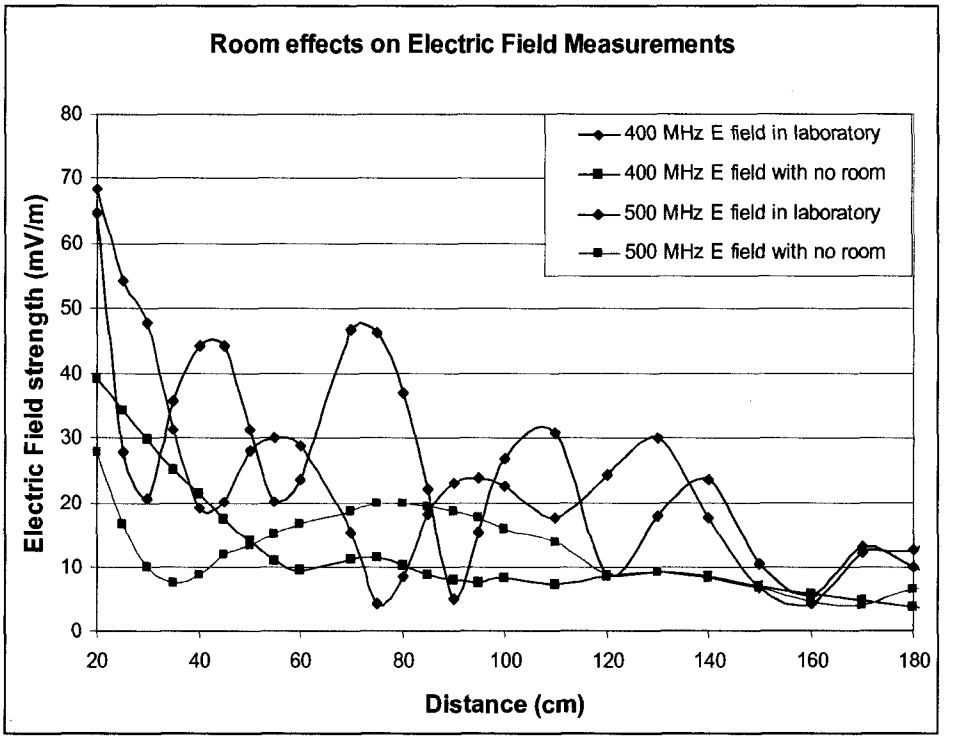

Figure 4-5 Comparison of radial electric field measurements made at 400 and 500 MHz; with (blue, red) and without (pink, cyan) room effects

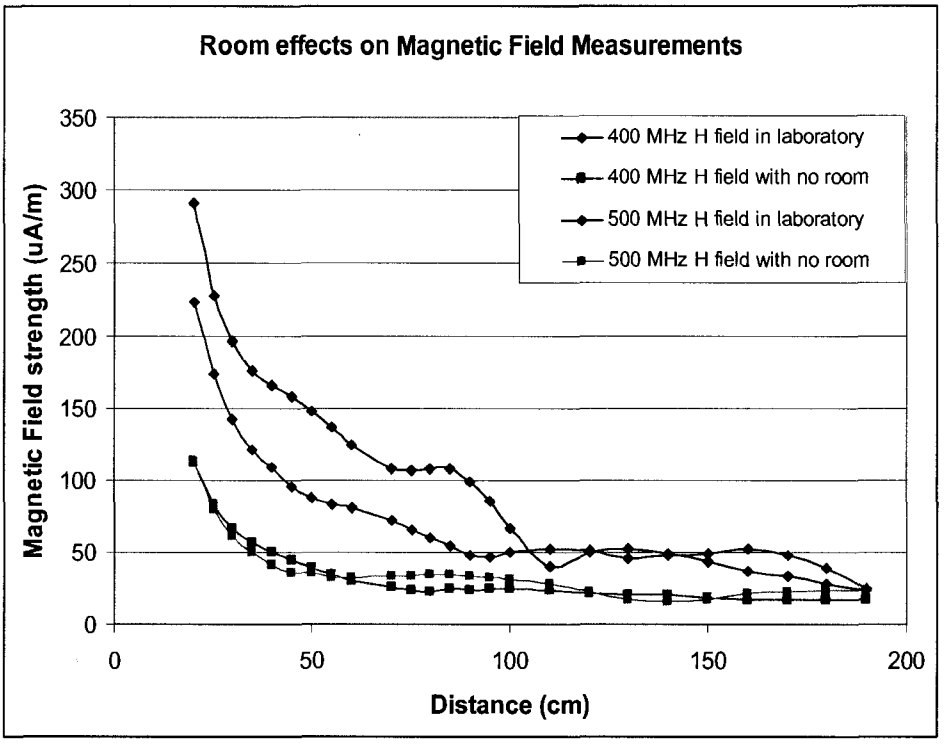

Figure 4-6 Comparison of radial magnetic field measurements made at 400 and 500 MHz; with (red, blue) and without (pink, cyan) room effects

4.1.3 Angular measurements

Angular measurements were performed using a dipole antenna as the radiation source (Figure 3-1). This was placed in the Delrin transmit antenna stand (Figure 3-12) The output signals sent to the dipole were supplied by the signal generator at a single frequency and power level via 50Ω coaxial cable. The frequencies used were 400 and 500 MHz to examine frequency dependence, and the power used was 1 mW (equivalently 0 dBm). The field probes were again connected to the spectrum analyzer and were placed on the receive stand. In these experiments the separation distance was kept constant at 50 cm and the transmit antenna was rotated through 180° (Figure 4-7), corresponding to start and finish angles of -90 and 90 degrees, respectively (i.e. the dipole center facing right to begin and left to finish).

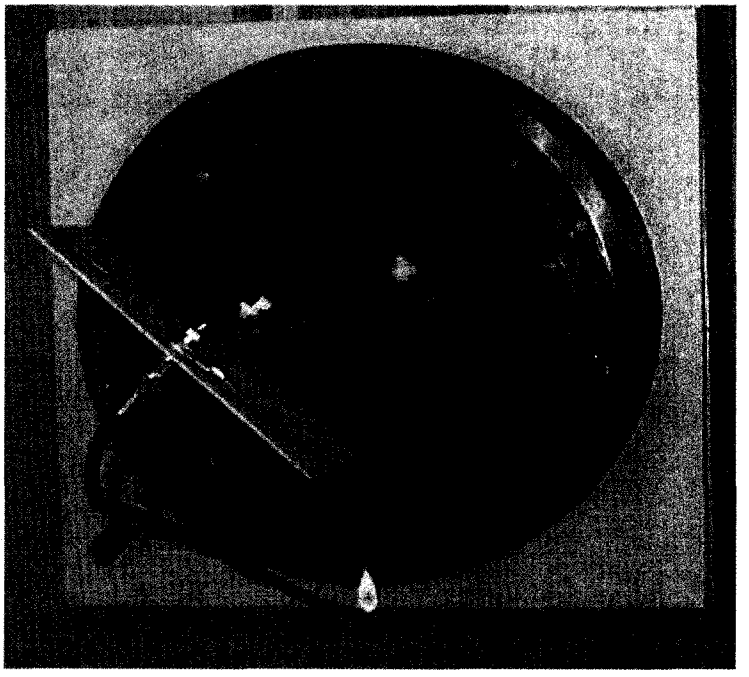

Figure 4-7 Rotation of dipole transmit antenna (shown at ~ 45°)

The results from these measurements can be seen in Figures 4-8 and 4-9. In these figures the radial spokes represent angles in degrees and the concentric circles represent a constant field strength value. There is not a good agreement between the angular measurements of the electric and magnetic field and the dipole theory. This difference could be due to the deleterious effects of the room upon the measurements; the measurement environment causes reflections which disrupt the measurement of the appropriate pattern. However, when measurements were repeated in the soccer field the pattern was similar to those seen in Figures 4-8 and 4-9; so the reflections due to the room are not definitively the cause of the discrepancy. Another possibility could be that the transmission lines attached to the field probes are acting as receiving antennas. This was tested by disconnecting the field probes and measuring the signal seen due to the

cable – no signal was seen. Another experiment was done putting a matched resistive load at the end of the transmission line instead of the field probes, but again no signal was measured so it was concluded that the transmission lines were properly shielded. It could be speculated that the transmission dipole is not producing the appropriate field; to test this hypothesis the frequency of emission was changed to 1 GHz, since this was closer to the half-wavelength frequency of the antenna. At this frequency the electric field was measured and the results are seen in Figure 4-10. Looking at this figure we see that the dipole does have the appropriate radiation pattern at this frequency, although it does not seem to produce the appropriate pattern at 400 and 500 MHz. Note that the plot displays a power measured in milliwatts; this is because the field probe does not have a listed performance factor at 1 GHz and so field values could not be calculated. As above, the current, I_0, could not be measured and the maximum theoretical values in Figures 4-8, 4-9 and 4-10 are scaled to the maximum values of the measured data.

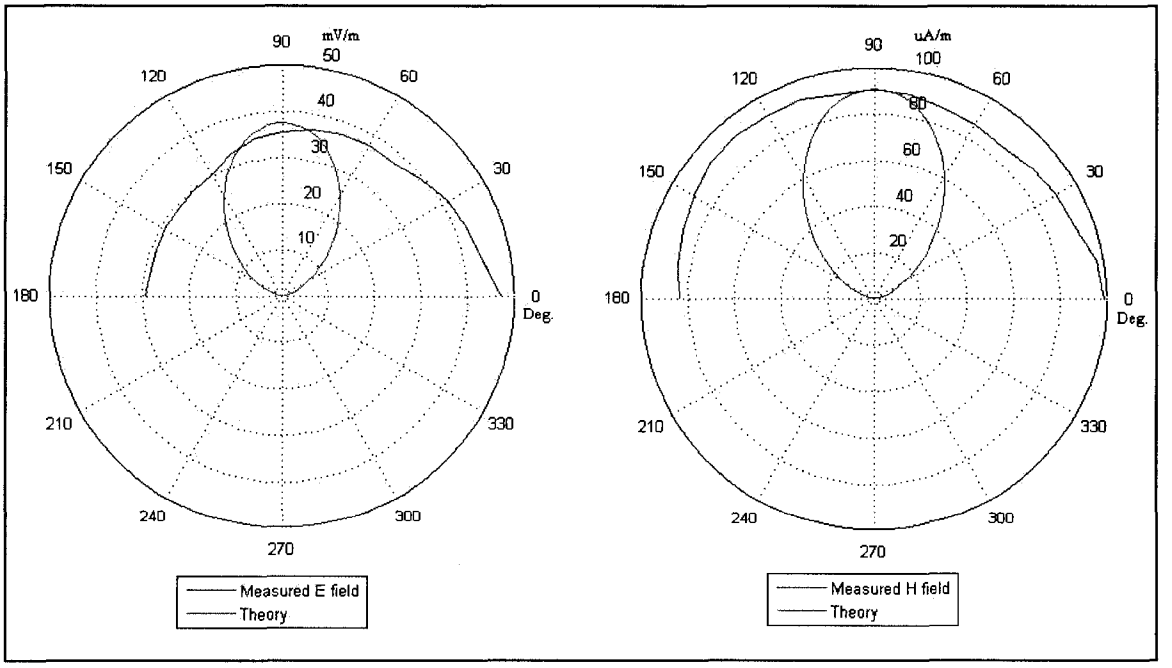

Figure 4-8 Angular field measurements for electric and magnetic fields at 400MHz

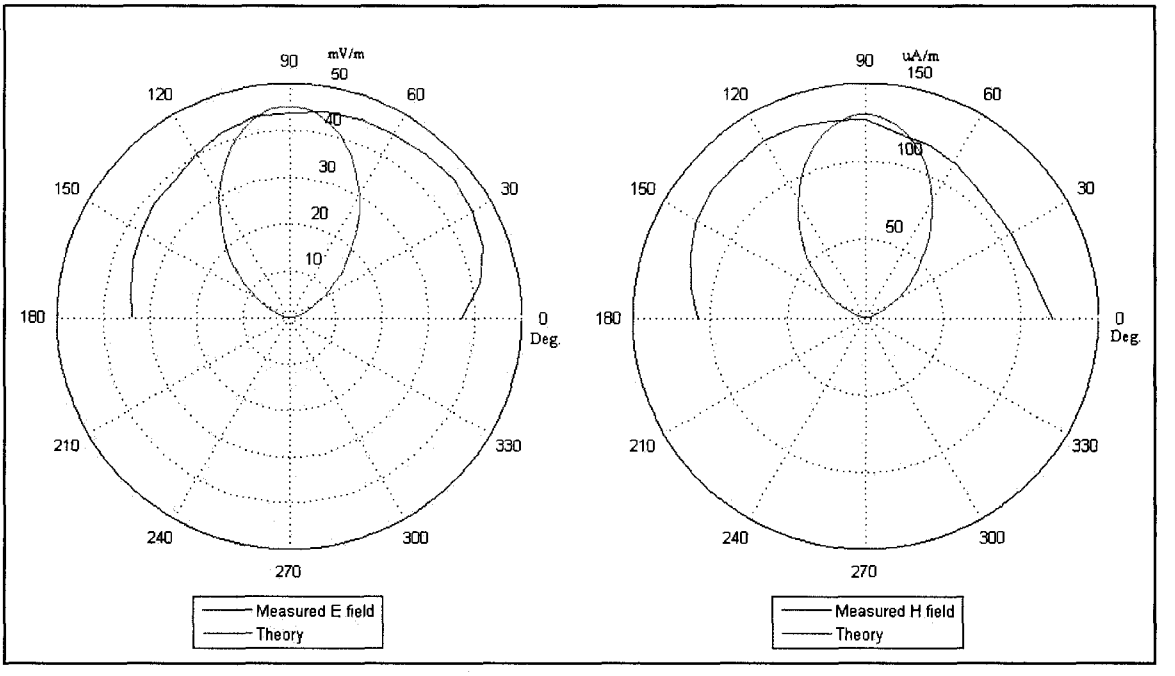

Figure 4-9 Angular field measurements for electric and magnetic fields at 500MHz

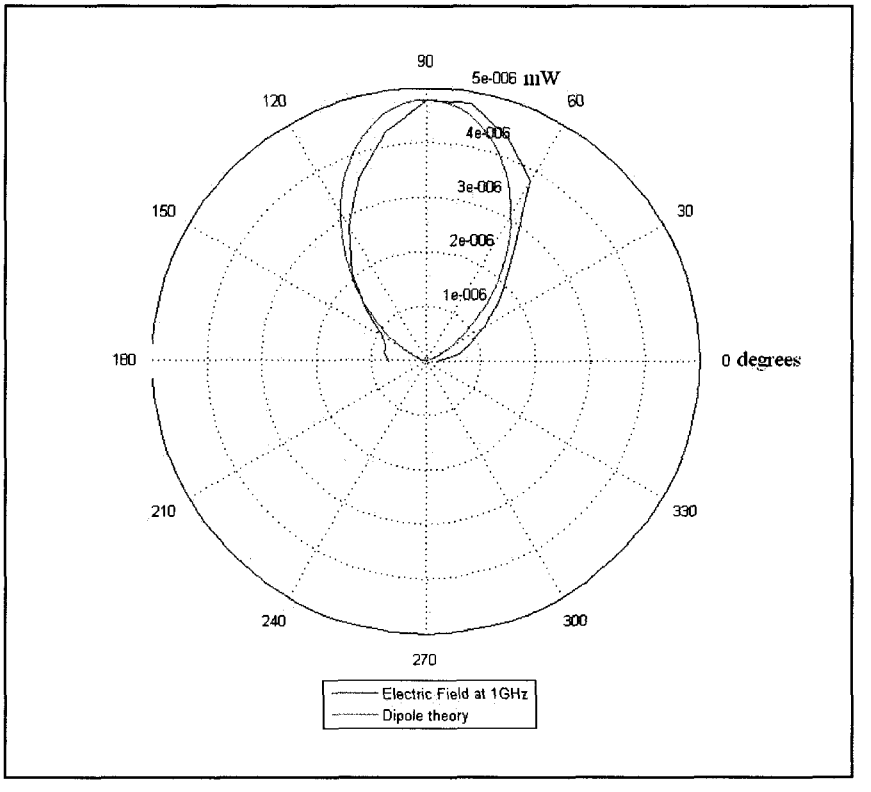

Figure 4-10 Angular electric field pattern of dipole antenna measured at 1GHz

4.2 Linear Accelerator Measurements (time domain)

The time-based oscilloscope measurements presented in section 3.2.2 were displayed graphically using DADiSP and the internal measurements were compared to the external measurements in order to discern possible correlation between the signals. If certain internal signals showed strong correlation with the emission signals (field measurements) then the source of emission could possibly be isolated and appropriately shielded to prevent interference between the linac and MRI system. The horizontal axis represents time in all the graphs. A vertical axis was not displayed because the voltages are not meaningful in this situation; only the time coincidence is important. Also, the voltages/currents of the test signals do not represent the true voltages/currents seen in the modulator and as such are not useful, as mentioned in chapter 3 they are scaled representations of the actual currents and voltages present in the modulator.

4.2.1 Electric field measurements

Figures 4-11 through 4-13 show the electric field probe signal compared to each of the internal signals that were measured. The timescales are all 25 microseconds and show the discharge portion of the cycle (as in Figures 3-15 and 3-17).

Figure 4-11 shows some correlation between the HVPS current switching on and the signal in the electric field probe, particularly in the regions of 5.5 to 6 microseconds and 7 to 8 microseconds. Therefore it is likely that the signal being measured by the electric field probe is in part caused by the HVPS current pulsing.

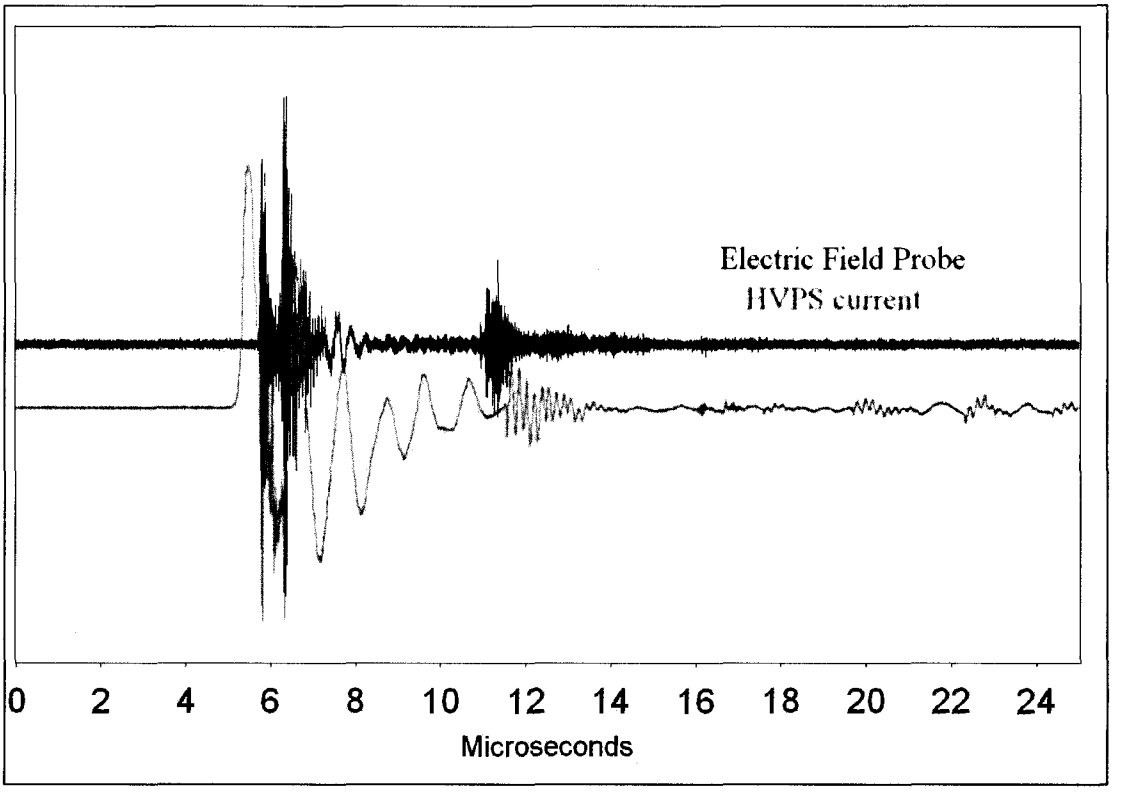

Figure 4-11 Time domain comparison of HVPS current and electric field probe signal

Figure 4-12 shows correlation between the magnetron current switching on/off and the second and third pulses of power seen in the electric field probe, occurring at approximately 6.5 and 11 microseconds, respectively. The relatively smooth shape of the magnetron current as it is switching on/off does not appear to present the same frequency components that are seen in the electric field probe, so in this case it is possible that the magnetron current is either indirectly causing these emissions, or that the electronics in the linac which transmit the signal to the system output do not adequately transmit the higher frequencies present in the signal. A third possibility is that the response of the E field probe, cable and oscilloscope is not ideal and the ringing occurs when the E field changes abruptly in time.

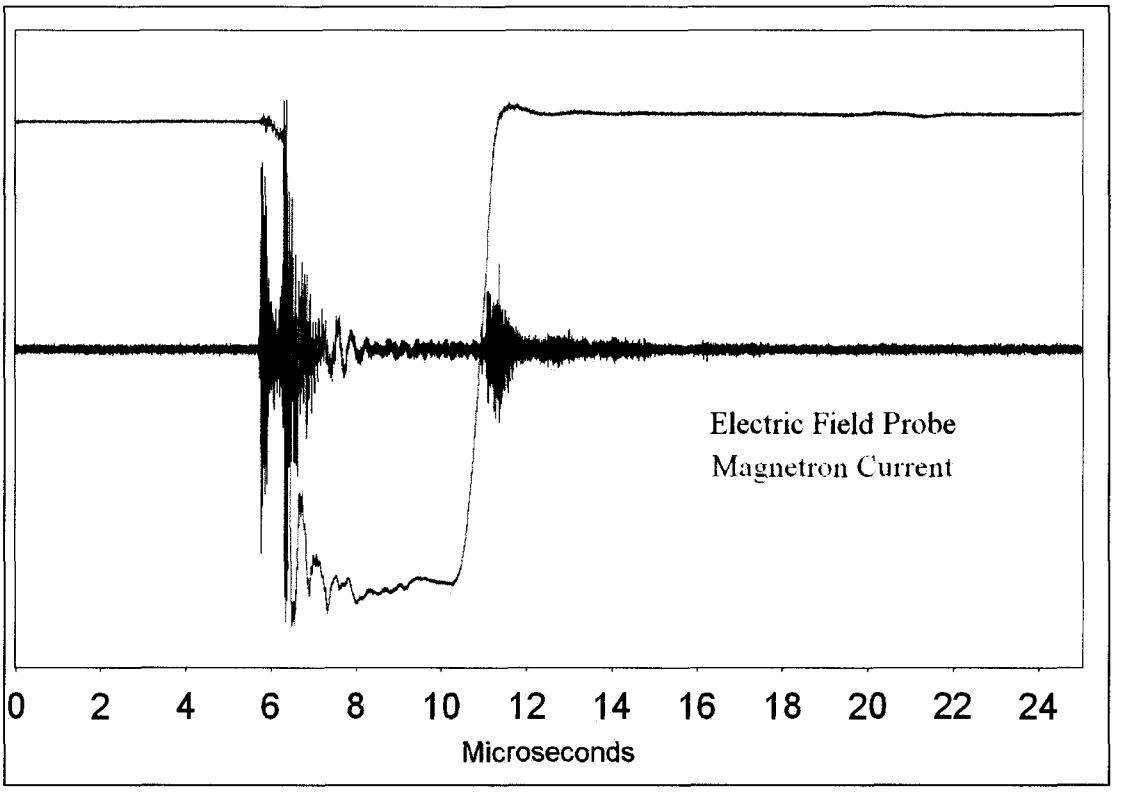

Figure 4-12 Time domain comparison of magnetron current and electric field probe signal

Figure 4-13 shows that the PFN voltage appears to have very good correlation with the first pulse of power seen on the electric field probe, at approximately 5.5 microseconds. The signals appear to begin simultaneously and also appear to have similar oscillation characteristics. There also appears to be some correlation between 7 and 8 microseconds; both signals have oscillation of similar shape present during this time period. Perhaps the PFN voltage is also a contributor to the electric field probe signal.

Figures 4-11 through 4-13 indicate that the EM signal emitted from a 600C linac and measured by the electric field probe is caused by several different sources, including the HVPS current, the magnetron current and the PFN voltage. Another possibility is that the test signals represent noise radiated from another location in the modulator and as such would not be the root cause of the signal.

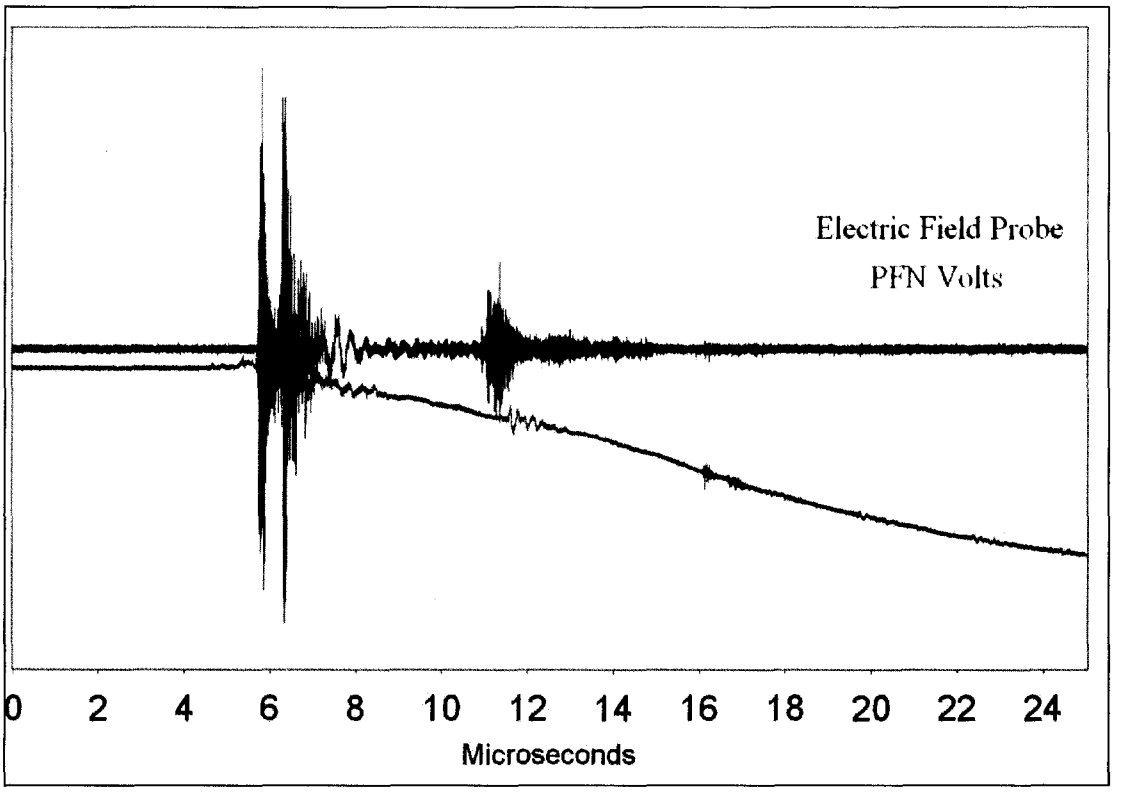

Figure 4-13 Time domain comparison of PFN voltage and electric field probe signal

4.2.2 Magnetic field measurements

Figures 4-14 through 4-16 show the magnetic field probe signal compared to each of the measured internal signals. Again here, the timescales are all 25 microseconds and show the discharge portion of the cycle.

Figure 4-14 shows the magnetic field probe signal and the HVPS current signal. There appears to be some correlation between the HVPS current pulsing on and the signal in the magnetic field probe. However, the initial pulse on the magnetic field probe ($\sim$ 6 μs) does not appear to correlate as closely with the HVPS current as the electric field probe does. There is also no visible correlation outside this one small area. The HVPS current also begins about 0.5 μs before any signal is seen in the field probe.

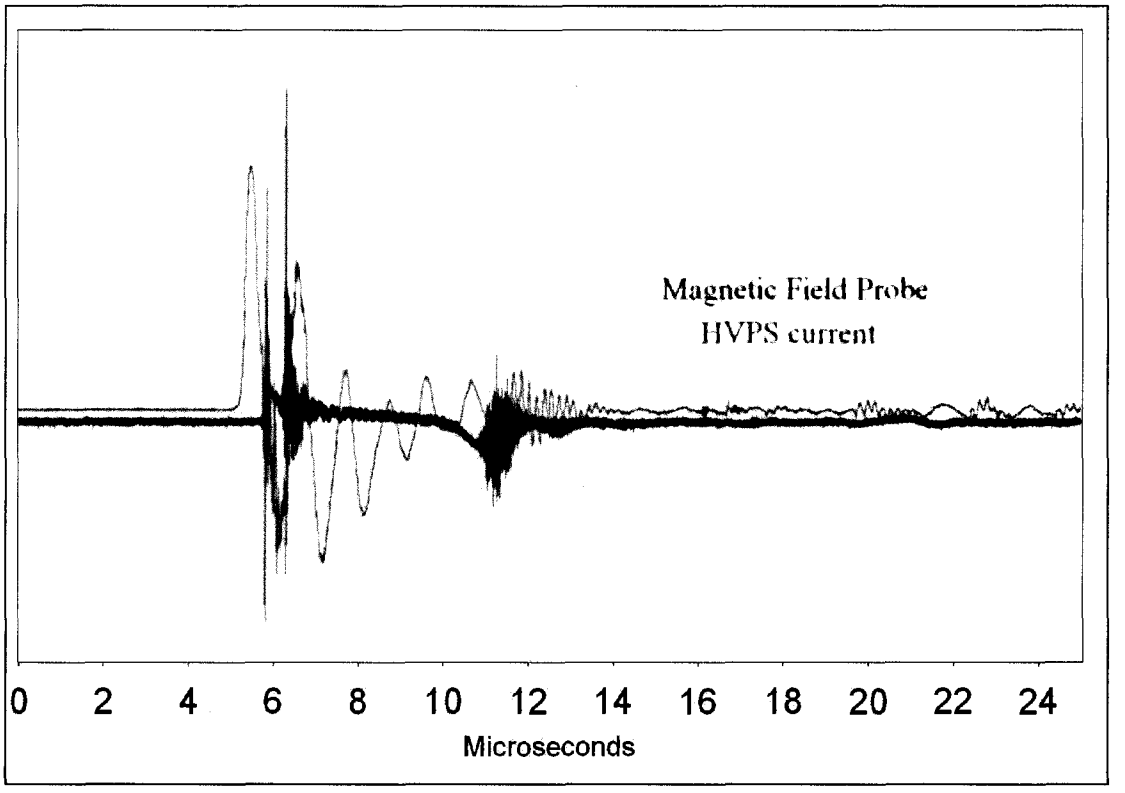

Figure 4-14 Time domain comparison of HVPS current and magnetic field probe signal

Figure 4-15 shows the magnetron current with the magnetic field probe signal. As seen with the electric field probe, there seems to be good correlation between the magnetron current switching on/off and the second and third pulses in the magnetic field probe signal. However, once again the smoothness of the magnetron current signal does not reflect the oscillation frequencies seen in the magnetic field probe signal. So, as before, the magnetron current signal may be inadequately represented due to problems with the electronics, or it may be indirectly causing the emissions being measured by the magnetic field probe. A third possibility is that the response of the E field probe, cable and oscilloscope is not ideal and the ringing occurs when the E field changes abruptly in time.

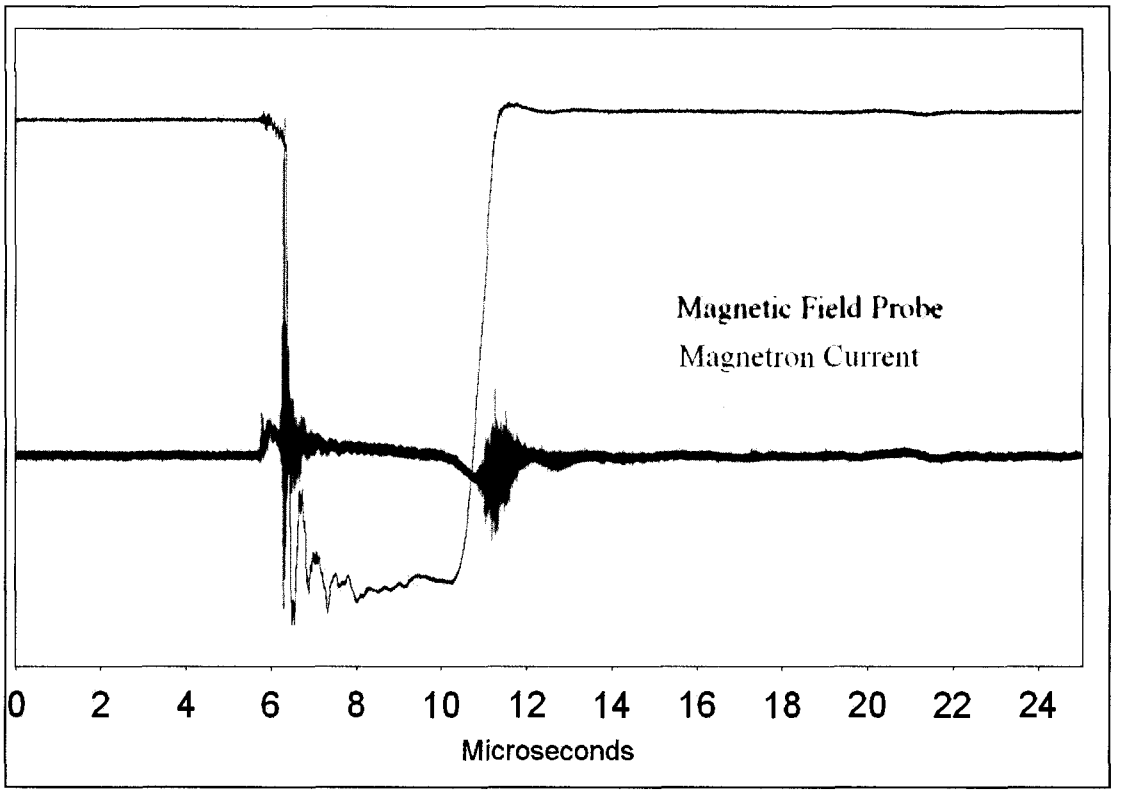

Figure 4-15 Time domain comparison of magnetron current and magnetic field probe signal

Figure 4-16 shows the PFN voltage along with the magnetic field probe signal. Here there appears to be some correlation between the PFN voltage and all three pulses present in the magnetic field probe signal, at ~ 6, 6.5, and 11 μs. There is particularly strong correlation between the PFN voltage beginning and the first pulse of signal in the magnetic field probe; the overlay makes it difficult to discern, but the two signals begin at the same instant. These two signals appear to be very closely related, indicating that the PFN voltage could be responsible for a large amount of the signal measured in the magnetic field probe.

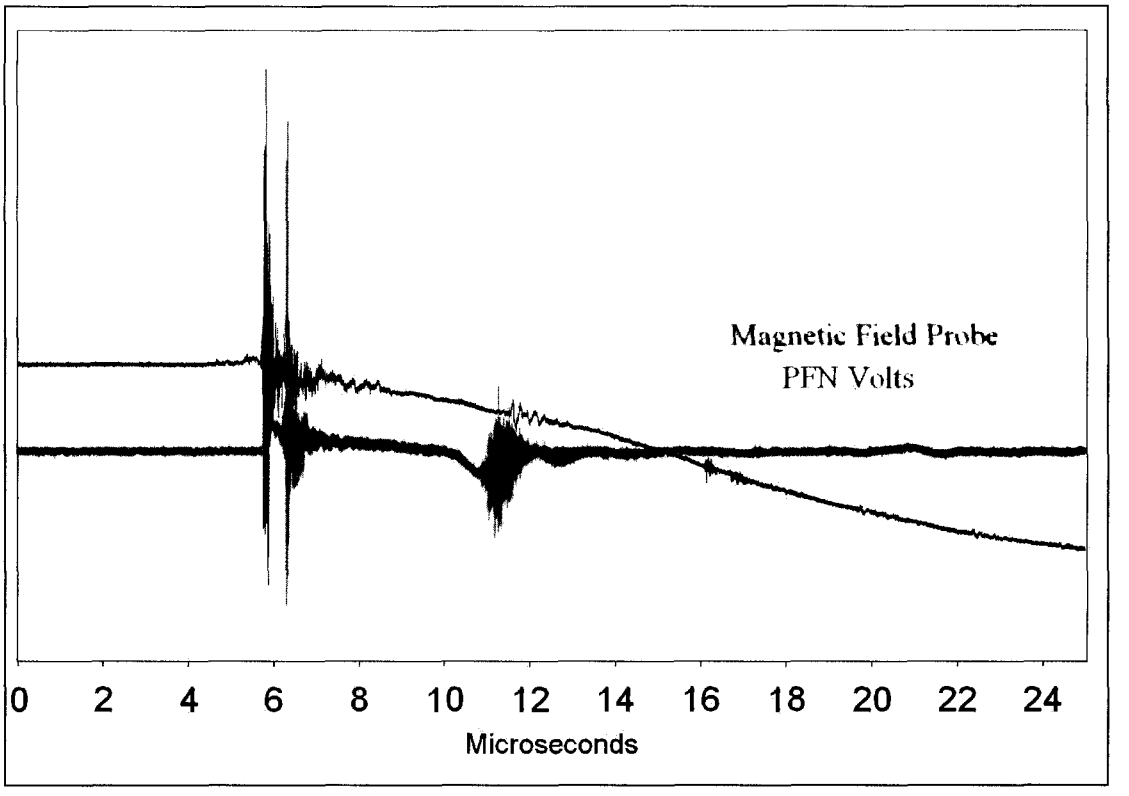

Figure 4-16 Time domain comparison of PFN voltage and magnetic field probe signal

4.3 Linear Accelerator Measurements (Frequency domain)

The figures in the previous section displayed some correlation between signals in time; to further examine the signal correlations the frequency spectra of these signals will now be examined. This was done by taking the normalized magnitude of the Fast Fourier transform of the signals using DADiSP ('SPECTRUM' command). This command is normalized so that, for example, a sine wave of amplitude A, and frequency F, will yield a SPECTRUM of amplitude A at frequency F. This command was used so that the values of the Fourier transform of the oscillographs would still represent real voltages, and thus the performance factor (see section 4.1.2) could be appropriately applied to yield electric and magnetic field strengths. The form of SPECTRUM is as follows:

$$spectrum(s) = \frac{2 \cdot mag(FFT(s))}{length(s)} \tag{4-6}$$

where FFT represents the fast Fourier transform.

Figures 4-11 through 4-16 will now be redisplayed as frequency spectra. All subsequent Fourier transforms are averaged over a time period of 50 microseconds. The horizontal axes will represent the frequency and applies to both displayed signals. The vertical axes will be field strength, and will thus apply only to the electric or magnetic field probe signals. The vertical axes for the test signals were not displayed because, as mentioned above, they do not represent the real voltages/currents seen in the modulator; only the frequency correlation is important for comparison. A cross-correlation method was used as a quantitative comparison tool, by extracting regions from both the test signals (HVPS, Magnetron current etc.) and the field probe signals. Regions were selected by finding peaks in the test signals and comparing these to the same frequency range in the field probe signals.

Cross-correlation is a method of comparing two signals. It is defined as follows [2]:

$$f(x) = g \star h = \int_{-\infty}^{\infty} g(u-x)h(u)du \tag{4-7}$$

Where g and h are two functions of u. The cross-correlation is similar in nature to a convolution, except that the function is not reversed, simply displaced before multiplication [2]. It is sometimes referred to as the 'sliding dot-product' because one function is 'slid' across the other producing a series of multiplication. Often the cross-correlation is expressed through the correlation coefficient, which is the normalized cross-correlation. It is normalized by the factor *f(0),* which yields correlation values between -1 and 1, with zero representing no correlation and 1 representing perfect

correlation. The correlation coefficient represents the similarity between the two signals. In the case of this thesis a high correlation coefficient represented a peak the same frequency being present in both the test signal and the measured electric/magnetic fields. Because of noise present in the signals and limited sampling rates, the threshold for correlation has been set very high (≥0.90). This threshold is somewhat arbitrary; it was chosen because regions with no correlation would not yield a value higher than 0.7, and so to assure no false positives the threshold was placed much higher than this value. It is possible that correlations exist in regions with a coefficient less than the threshold but they are not definitive using this method.

4.3.1 Electric field measurements

Figure 4-17 shows the frequency comparison of the electric field probe signal with the HVPS current. The values in table 4-1 represent the frequencies which displayed good correlation. The frequency range and number of points was chosen based on the width of the peak and the amount of noise surrounding it. Figure 4-17 shows that there is very good agreement at several frequencies (Table 4-1) between these two signals. This reinforces the correlation seen in Figure 4-9 and definitively shows that several of the frequencies seen in the electric field probe are contained in the HVPS current and could be the result of the HVPS current pulsing. It should be noted that there are several other peaks present in the electric field probe signal that do not appear to be present in the HVPS current. This implies that the HVPS current could be a major source of electric field noise, but is not the sole source.

Frequency (+/- 0.5MHz)	Correlation Coefficient (normalized to 1)	Frequency range/#points (MHz)
10 MHz	0.92	7.7-12.2/300
14.5 MHz	0.95	11.5-17.6/400
31.5 MHz	0.96	28.3-34.3/400
36.2 MHz	0.91	35.1-38.2/200
49.2 MHz	0.97	47.7-49.7/130

Table 4-1 Comparison of HVPS current frequencies to electric field probe frequencies

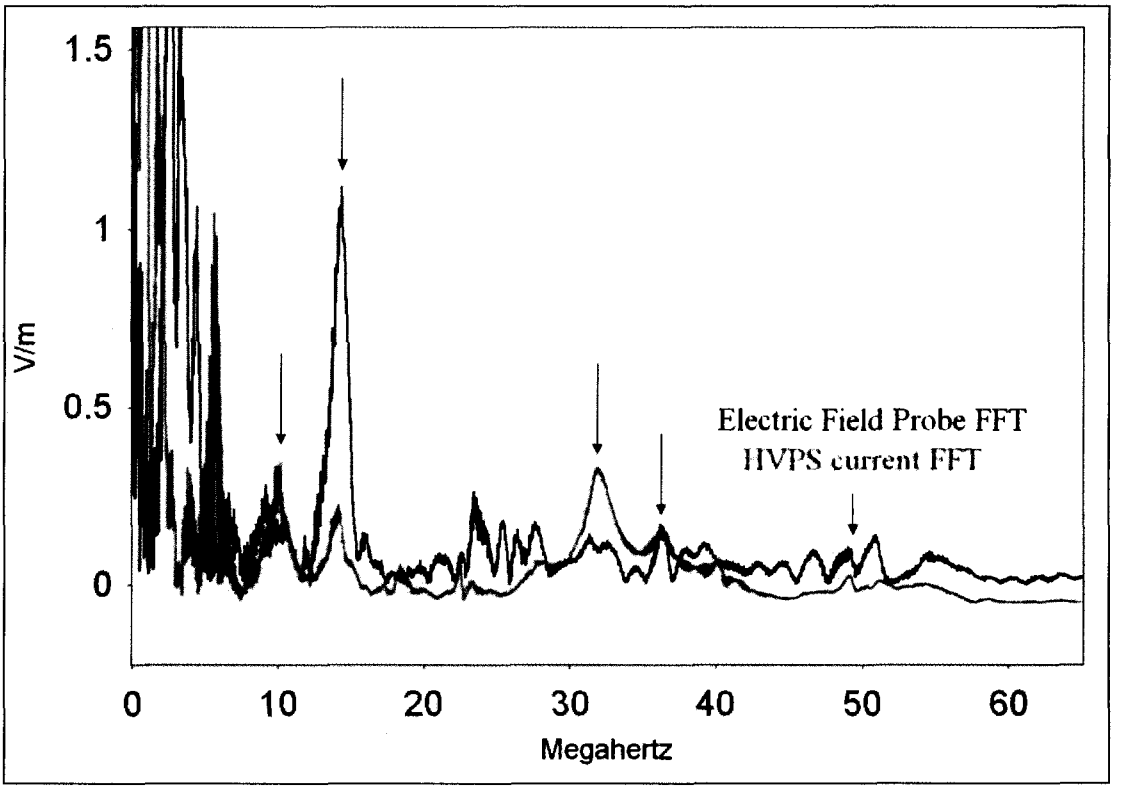

Figure 4-17 Frequency comparison of HVPS current and electric field probe signal

Figure 4-18 shows the frequency comparison of the electric field probe signal with the magnetron current and table 4-2 contains the frequencies of correlation. There is some

correlation between these two signals at lower frequencies, but they do not display as much correlation as was seen with the HVPS current. The field values at these frequencies are higher than those seen at the frequencies overlapping with HVPS current. This implies that although the magnetron current only displays modest correlation with the electric field probe, it is a source of noise that will need shielding consideration due to the strength of the electric field at these frequencies.

Frequency (+/- 0.5MHz)	Correlation Coefficient (normalized to 1)	Frequency range/#points (MHz)
2.41 MHz	0.90	1.5-4.6/200
2.59 MHz	0.90	1.5-4.6/200

Table 4-2 Comparison of magnetron current frequencies to electric field probe frequencies

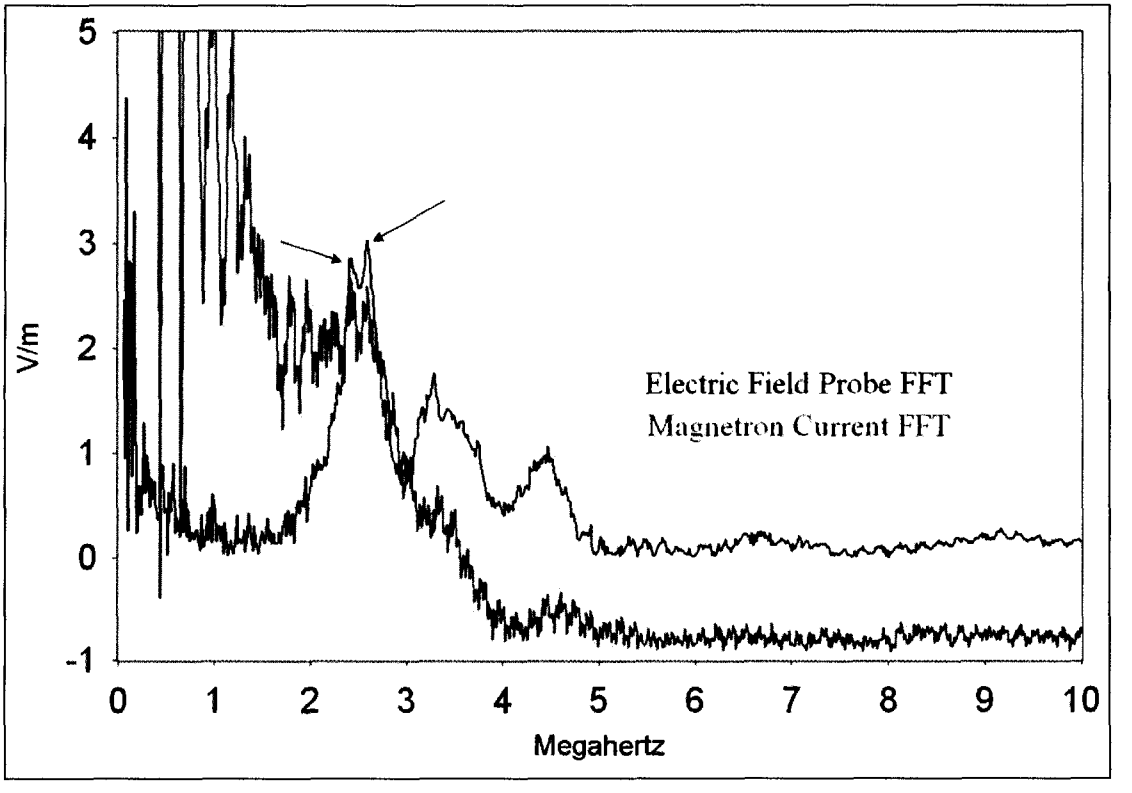

Figure 4-18 Frequency comparison of magnetron current and electric field probe signal

Figure 4-19 shows the frequency comparison of the electric field probe signal with the PFN voltage. There is no obvious correlation between these two signals and so, despite the correlation between these two signals seen in the time domain, the PFN voltage does not appear to contribute to the electric field emissions measured by the field probe.

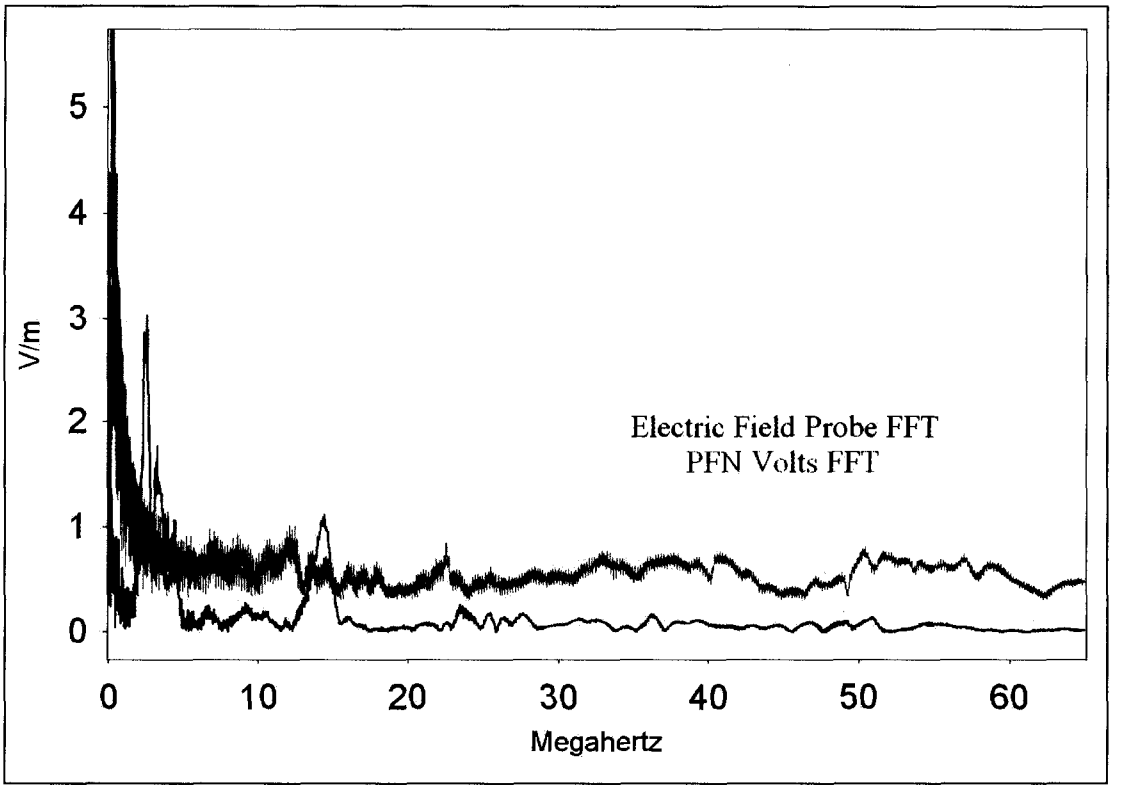

Figure 4-19 Frequency comparison of PFN voltage and electric field probe signal

4.3.2 Magnetic field measurements

Figure 4-20 shows the frequency comparison of the magnetic field probe signal with the HVPS current. Table 4-3 shows the frequencies which displayed good correlation. There

was only one frequency peak that displayed good correlation; however, there are other peaks which appear to be related (i.e. ~9.5 to 10 MHz) but were not at the exact same frequency so did not provide a good correlation coefficient.

Frequency (+/- 0.5MHz)	Correlation Coefficient (normalized to 1)	Frequency range/#points (MHz)
14.5 MHz	0.94	11.5-16.0/300

Table 4-3 Comparison of HVPS current frequencies to magnetic field probe frequencies

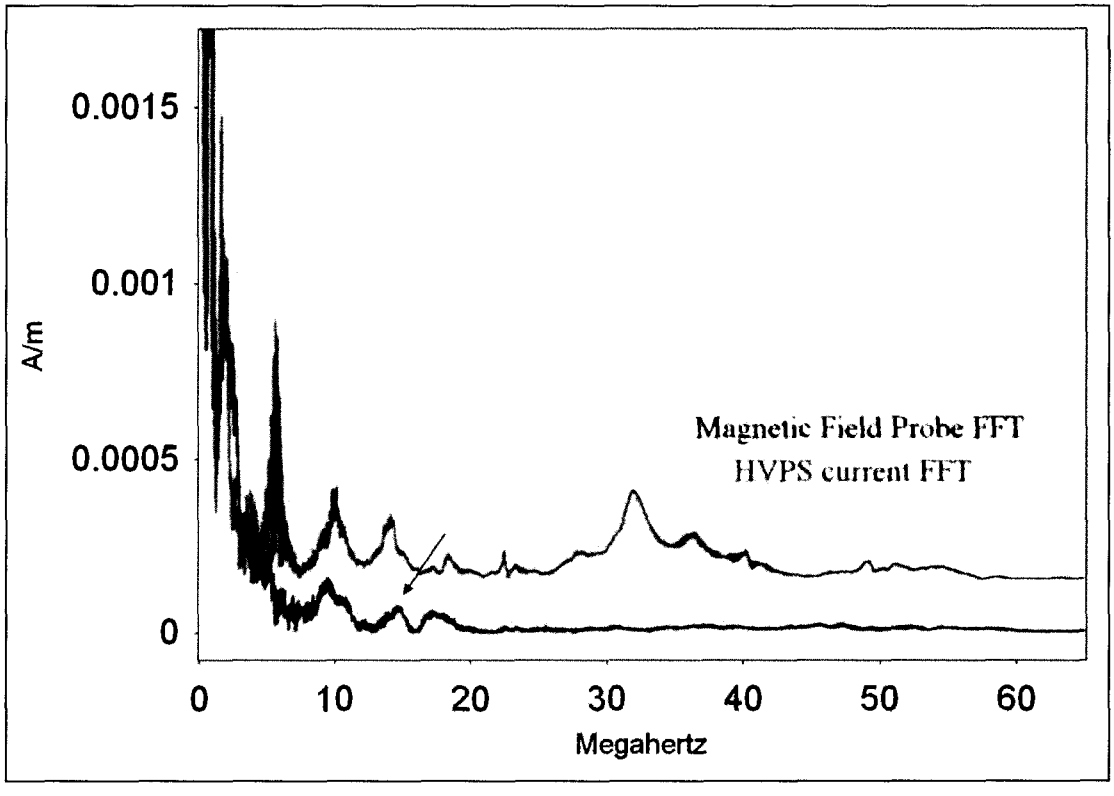

Figure 4-20 Frequency comparison of HVPS current and magnetic field probe signal

Figure 4-21 shows the frequency comparison of the magnetic field probe signal with the magnetron current and table 4-4 contains the frequencies of overlap. The frequencies of

overlap in this case are very low (on the order of kilohertz) and contribute only a small portion of the full frequency band seen in the magnetic field probe signal. Note that the x axis is a much smaller span than in Figure 4-20 and this causes the plot to appear less noisy.

Frequency (+/- 0.5MHz)	Correlation Coefficient (normalized to 1)	Frequency range/#points (MHz)
0.3	0.99	0.23-0.40/12
0.55	0.97	0.44-0.64/14

Table 4-4 Comparison of magnetron current frequencies to magnetic field probe frequencies

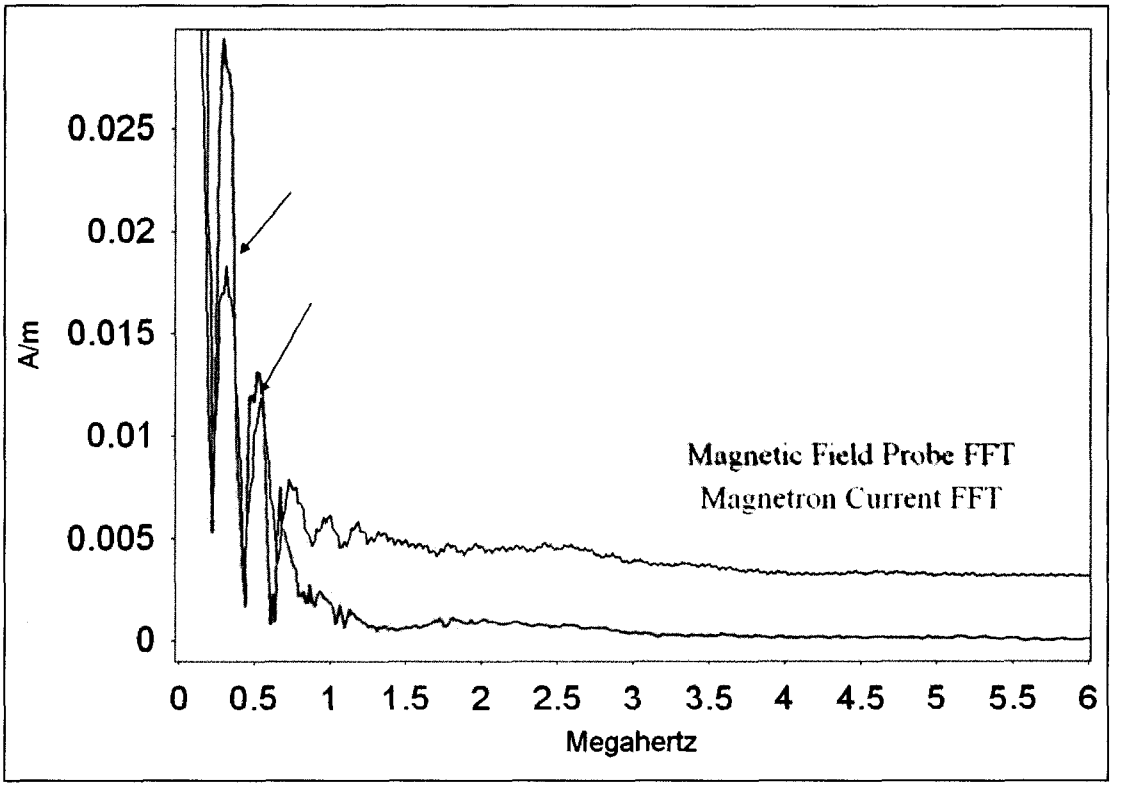

Figure 4-21 Frequency comparison of magnetron current and magnetic field probe signal

Figure 4-22 shows the frequency comparison of the magnetic field probe signal with the PFN voltage. Table 4-5 contains the frequencies of correlation between the two signals. There are several frequencies which displayed correlation, and although the coefficient was only 0.87 at 22.5 MHz, it was included because the shapes very closely resemble each other and are almost certainly correlated. The PFN voltage appears to contribute the most frequency components to our magnetic field signal. This is intuitive as the PFN discharges through a large inductor; this inductor is similar in shape to a solenoid and as such should create magnetic fields around it, analogous to that created by current flowing through a solenoid.

Frequency (+/- 0.5MHz)	Correlation Coefficient (normalized to 1)	Frequency range/#points (MHz)
22.5 MHz	0.87	20.6-24.3/250
37.5 MHz	.98	35.1-38.9/250
81.3 MHz	0.97	76.3-84/500

Table 4-5 Comparison of PFN voltage frequencies to magnetic field probe frequencies

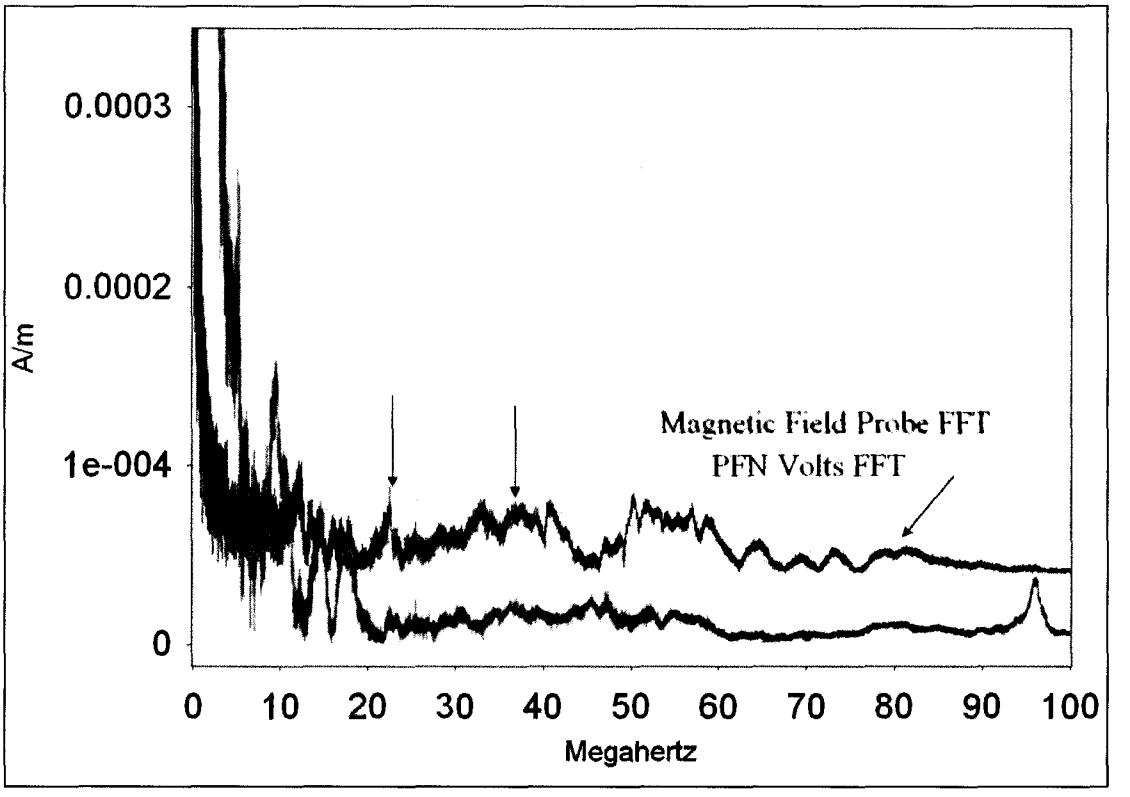

Figure 4-22 Frequency comparison of PFN voltage and magnetic field probe signal

4.4 Electric and Magnetic field values

The previous sections have discussed the time and frequency correlation between measured signals. It is also important to examine the field strengths being measured by the electric and magnetic field probes. Figures 4-23 and 4-24 display the electric and magnetic field values versus frequency where the vertical axis is chosen to display the maximum field value, which occurs near the DC component. The field values were calculated as per section 4.1.2 using the appropriate frequency dependent performance factors. The magnetic field plot (Figure 4-24) is shifted horizontally in order to properly

display this maximum component which is seen in the low frequency region of the plot (see *x* axis).

The electric field signal (Figure 4-23) shows values of over 1V/m for certain frequencies, up to approximately 15 MHz; these are fairly large field values and cannot be ignored. On the other hand, it can be seen that there is very little magnetic field strength beyond 1 MHz, relative to the initial value of approximately 0.24 A/m. Figure 4-25 shows a scaled version of Figure 4-24; the y axis is scaled to display the signal topography present at the higher frequencies. Here we can see that there are field values that are above background contained in the magnetic field signal, but that their values are quite small.

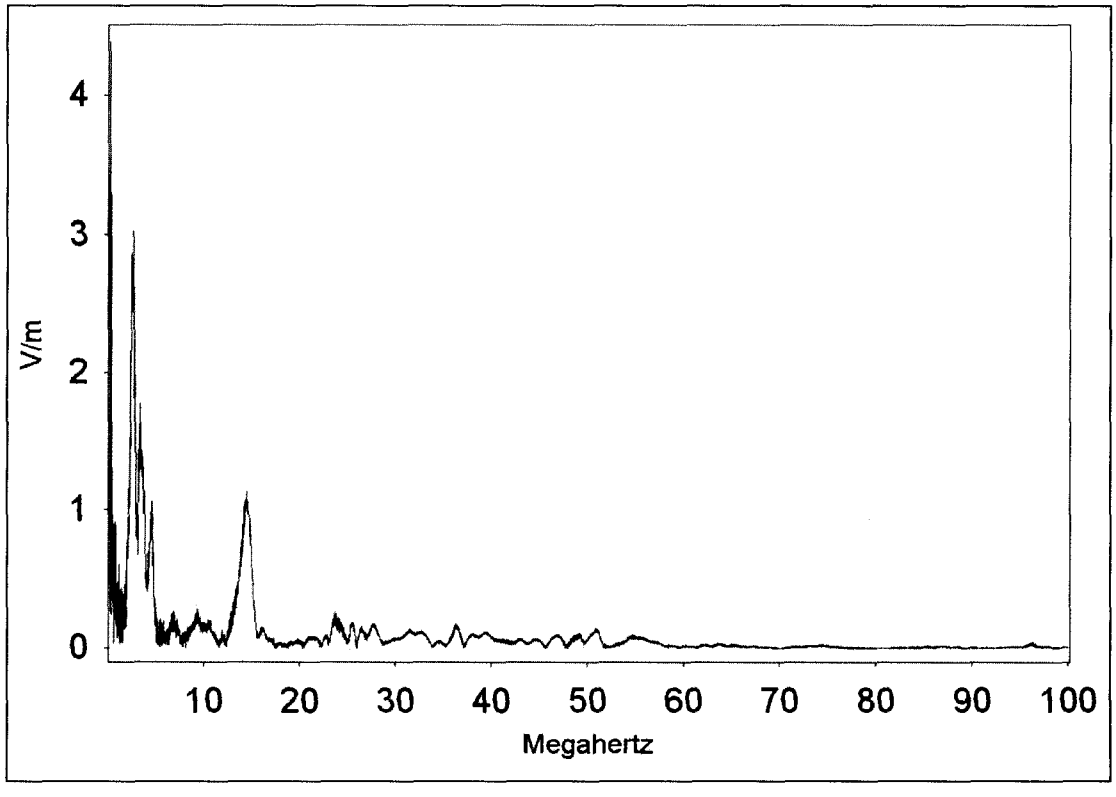

Figure 4-23 Electric field values as a function of frequency

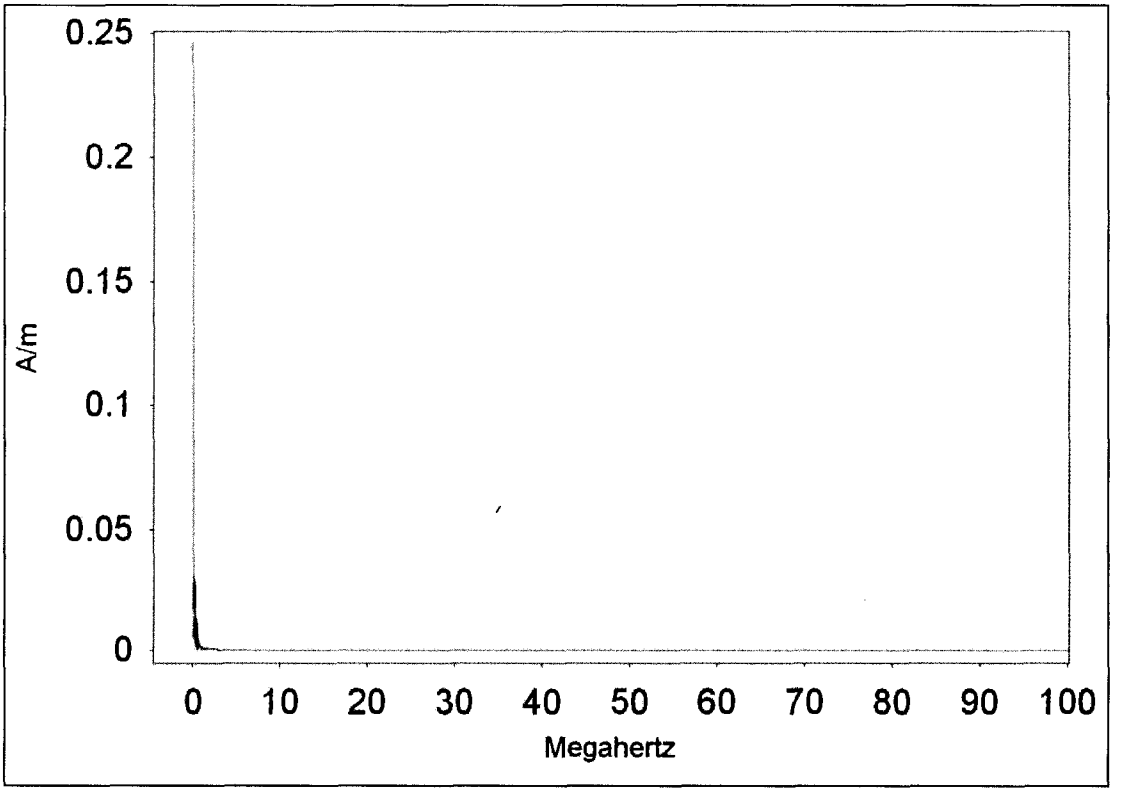

Figure 4-24 Magnetic field values as a function of frequency

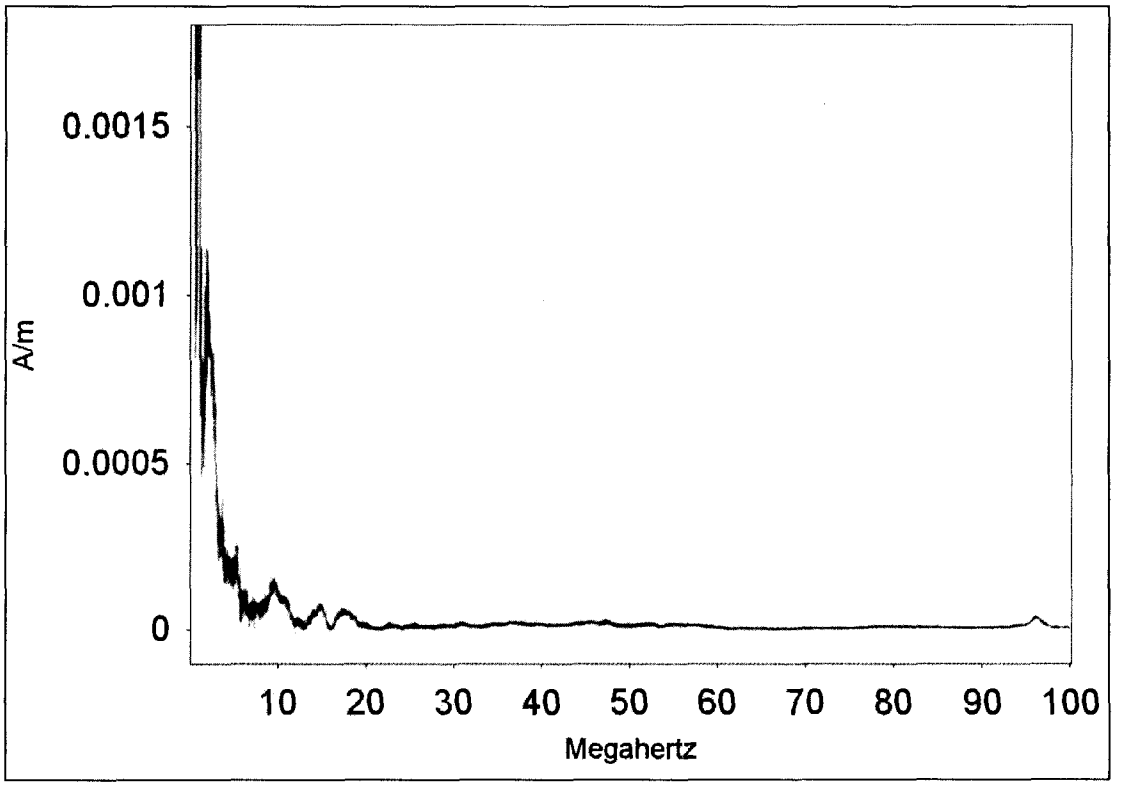

Figure 4-25 Magnetic field values as a function of frequency (scaled y -axis)

References:

1. Balanis, C. A., *Antenna Theory: Analysis and Design 2nd Edition,* Wiley & Sons, New York, 1997.
2. Bracewell, R.N., *The Fourier Transform and its Applications*, 3rd Edition, McGraw-Hill, New York, 1965.

5 Discussion

5.1 Antenna pattern measurements

Based on the results in chapter 4, and taking into account the rudimentary design of our dipole transmitter, the measurement technique was able to partially reproduce the radiation pattern of the dipole at 400 and 500 MHz. The results showed obvious perturbations due to the measurement environment; however, moving the antenna outside into the field showed reduced effects due to reflections and the radial measurements matched fairly closely to a theoretical curve. The corresponding angular measurements did not match the theory, but the close match at 1 GHz showed that the probes are measuring the correct field strengths. It appears that the constructed dipole does not radiate the proper angular field pattern at 400 and 500 MHz. These results, taken together, demonstrate that this measurement technique can be applied, with caution, to other RF sources. This technique was next applied to measuring the RF noise associated with medical linear accelerators

5.2 Linear Accelerator Measurements

The measurements in sections 4.2 and 4.3 appear to confirm that the electromagnetic noise being emitted by the modulator portion of a linac is emanating from multiple sources. There was correlation seen between internal system signals (HVPS current, magnetron current and PFN voltage) and the electric and magnetic field components. Strong correlation was seen between the HVPS current and the electric field probe; strong correlation was also seen between the magnetic field probe and the PFN voltage.

Further investigation must be done to more definitively isolate the emission sources. It is also possible that the noise being measured is simply being carried by the test signals but actually originates from another section in the modulator. Further investigation of this is currently being pursued by a colleague.

Section 4.4 showed that there are field values that can be large at certain frequencies and thus will be important when assessing shielding requirements. The magnetic field values are only large at very low frequencies, while the electric field values can be substantial up to approximately 50 MHz (Figure 4-21). Figure 5-1 shows a crude power density approximation, it is found by approximating equation 2-2 as follows:

$$W = \frac{|E| \cdot |H|}{2} \tag{4-2}$$

The figure shows that at low frequencies there can be power densities on the order of hundreds of milliwatts per square meter but that for most frequencies the power level is small. However, according to ref [1], pp.4-5, the power received from the patient during the MR imaging process is on the order of microwatts. At the Larmor frequency of the 0.2 Tesla magnet, 8.5 MHz, intended for use in the MRI-Linac the power level is approximately 5 $\mu W/m^2$, which is sufficient to affect the imaging process. Therefore appropriate shielding measures will have to be taken, but those are beyond the scope of this thesis.

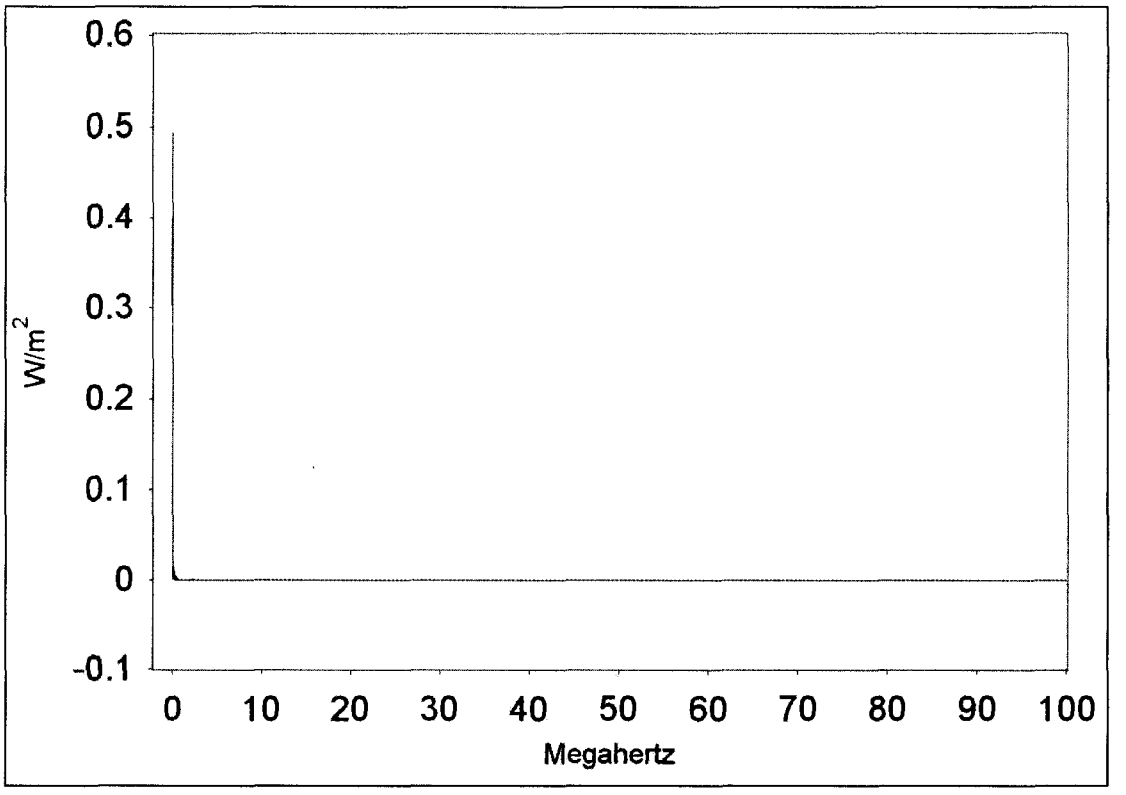

Figure 5-1 Approximation of power as a function of frequency

References:

1. ECRI Institute, "*Scanning Systems, Magnetic Resonance Imaging*". URL: http://docs.ksu.edu.sa/PDF/Articles34/Article340196.pdf , May 2003.

6 Conclusions and Future Work

6.1 Conclusions

The advent of IGRT has changed the way radiotherapy is applied, and the next logical step in the evolution of IGRT is the implementation of a real-time imaging and treatment system. The integration of an MRI scanner with a linac would provide a major step towards achieving this real-time system. The proposal at the Cross Cancer Institute to integrate a medical linac with a 0.2 Tesla, open bore magnet provides a simple, effective design to accomplish the intended goal.

The technological and mechanical obstacles which would inhibit this integration must be overcome and one of these obstacles is the RF interference between the MRI and the linac due to RF emanating from the linac. This extraneous RF could have deleterious effects on the image quality produced by the MR scanner. Hence, a technique to measure this RF must be tested. In section 4.1 a technique was tested for making quantitative near field RF measurements using a known radiation source and the electric and magnetic field probes. The results of these measurements showed that the technique can be applied with caution to other systems. This measurement technique was then taken and applied to measuring RF emanating from a medical linac (Section 4.2).

The electric and magnetic field measurements showed interesting results. First, it appears that there is correlation between the measured fields and the linac test signals. In particular there appeared to be significant correlation between the electric field

measurements and the high voltage power supply current, and between the magnetic field measurements and the PFN voltage. These correlations were seen in both the time and frequency domains. Second, the field values seen in section 4.4 suggest that shielding will be necessary for frequencies below 15 MHz; specifically, there are electric field values that are on the order of 1 V/m in this frequency range, corresponding to power levels ranging from microwatts to milliwatts. These power levels could affect the proper functioning of the MRI imager and should be appropriately shielded.

6.2 Future Work

This thesis has demonstrated a measurement technique, and has applied it to a medical linac; from this a few conclusions about the RF emissions of the linac were made. However, these are preliminary measurements and more detailed measurements should be made. Some of the future work that may be necessary is as follows:

1. To further isolate the actual sources of RF noise in the linac. Comparisons were made to system test signals in Chapter 4, but it is possible that there is some contamination between these signals; noise could be transferred between signals and may actually be arise from another source or sources. So the test signals need to be isolated from each other to discern the actual sources of RF emissions – though this may not be physically possible
2. The shielding of individual sections of the linac modulator. Once the RF noise sources have been isolated, the individual sections of the modulator, that are sources of noise, could be shielded to see the effect on overall RF emission. It may be possible to limit shielding to a few key components of the modulator,

rather than shielding the entire linac. This would allow for a less bulky prototype design, so the shielding would not hinder machine movement or the addition of new sections to the design.

3. The modification of the electronic setup of the modulator to control the RF emissions. It may be possible through manipulation of cable lengths etc. to control the frequencies of RF emission, or perhaps even to minimize or eliminate the RF noise. These changes could be guided by simulations of the modulator circuitry done by a colleague, M. Lamey.

In conclusion, the appropriate measurement of the RF emissions of a medical linac will be necessary for the design of appropriate RF shielding for the MR-Linac unit. This shielding will help to ensure the seamless integration of a linac with a MR imager.

7 Bibliography

1. Bernier, J., Hall, E.J., Giaccia, A. Radiation oncology: a century of achievements. *Nature Reviews Cancer* **4**, 737-747 (2004).
2. Verellen, D., De Ridder, M., Linthout, N., et al. Innovations in image-guided radiotherapy. *Nature Reviews Cancer* **7**, 949-960 (2007).
3. Dawson, L.A., Jaffray, D.A. Advances in Image-Guided Radiation Therapy. *Journal of Clinical Oncology* **25(8)** 938-946 (2007)
4. Marcel van Herk. Errors and Margins in Radiotherapy. *Seminars in Radiation Oncology* **14(1)** 52-54 (2004)
5. Rietzel, E., Rosenthal, S.J., Gierga, D.P., et al. Moving targets: detection and tracking of internal organ motion for treatment planning and patient set-up. *Radiother. Oncol.* **73** S68-S72 (2004)
6. Langen, K.M., Jones, T.L. Organ motion and its management *Int. J. Radiation Oncology Biol. Phys.* **50(1)** 265-278 (2001)
7. S Webb. Motion effects in (intensity modulate) radiation therapy: a review. *Physics in Medicine and Biology* **51** R403-R42 (2006).
8. Jake Van Dyke. *The Modern Technology of Radiation Oncology: A Compendium for Medical Physicists and Radiation Oncologists*. Medical Physics Publishing, Madison, Wisconsin, 1999.
9. Stützel, J., Oelfke, O., Nill, S. A quantitative image quality comparison of four different image guided radiotherapy devices. *Radiotherapy and Oncology* **86** 20-24 (2008)

10. Lagendijk, J.J.W., Raaymakers, B.W., Raaijmakers, A.J.E., et al. MRI/linac integration. *Radiotherapy and Oncology* **86** 25-29 (2008)

11. J.F. Dempsey. An Image-Guided Device Providing 4D CINE MRI Simultaneous to Radiotherapy Delivery. *Journal of Radiotherapy in Practice* **5** 179 (2006)

12. www.viewray.com

13. Carwardine, J.A., Wang, J. Analysis of the Electrical Noise from the APS Kicker Magnet Power Supplies. Proceedings of the 1995 IEEE *Particle Accelerator Conference.* **2** 1242-1244 1995

14. Karzmark, C.J., Nunan, C.S., Tanabe, E., *Medical Electron Accelerators*, McGraw-Hill Inc., New York, 1993

15. Kirkby, C., Stanescu, T., et al. Patient dosimetry for hybrid MRI-radiotherapy systems. *Medical Physics* **35** 1019 (2008)

16. Stanescu, T., Kirkby, C., et al. Sci-Fri PM: Planning-02: MRI-based radiation treatment planning for an MRI-linac system. *Medical Physics* **35** 3412 (2008)

17. Griffiths, D. J., *Introduction to Electrodynamics 3rd Edition*, Prentice Hall, New Jersey, 1999.

18. Jackson, J. D., *Classical Electrodynamics 3rd Edition*, Wiley & Sons, New York, 1999.

19. Balanis, C. A., *Antenna Theory: Analysis and Design 2nd Edition,* Wiley & Sons, New York, 1997.

20. Maclean, J., Sutton, R., Hoffman, R., "Interpreting Antenna Performance Parameters for EMC Applications Part 1: Radiation Efficiency and Input Impedance Match", *TDK RF Solutions.*

21. *IEEE Transactions on Antennas and Propagation*, Vols. AP-1, No. 3, May 1969; Vol. AP-22, No. 1, January 1974; and Vol. AP-31, No. 6, Part II, November 1983.

22. Maclean, J., Sutton, R., Hoffman, R., "Interpreting Antenna Performance Parameters for EMC Applications Part 2: Radiation Pattern, Gain, and Directivity", *TDK RF Solutions*

23. Stutzman, W.L., Thiele, G.A., *Antenna Theory and Design*, Wiley & Sons, New York, 1981.

24. Stewart, J., *Calculus 4th Edition*, Brookes/Cole Publishing Company, Pacific Grove, 1999.

25. Oncology 560 class notes. University of Alberta Medical Physics (2005).

26. *Operating Manual for HZ-11Probe Set*, Rohde & Schwarz: Instrument Division. Munich, Germany.

27. *Agilent 4396B Network/Spectrum/Impedance Analyzer Data Sheet.* Agilent Technologies, Santa Clara, California, 2003.

28. *Agilent Technologies InfiniiVision 6000 Series Oscilloscopes Data Sheet.* Agilent Technologies, Santa Clara, California, 2003.

29. *Agilent ESG-A and ESG-D RF Signal Generators Data Sheet.* Agilent, Santa Clara, California, 2003.

30. ECRI Institute, "*Scanning Systems, Magnetic Resonance Imaging*". URL: http://docs.ksu.edu.sa/PDF/Articles34/Article340196.pdf , May 2003.

31. Bracewell, R.N., *The Fourier Transform and its Applications*, 3rd Edition, McGraw-Hill, New York, 1965.